



LJMU Research Online

Topping, MW, Stark, DP, Senchyna, P, Chen, Z, Zitrin, A, Endsley, R, Charlot, S, Furtak, LJ, Maseda, MV, Plat, A, Smit, R, Mainali, R, Chevallard, J, Molyneux, S and Rigby, JR

Deep Rest-UV JWST/NIRSpec Spectroscopy of Early Galaxies: The Demographics of C iv and N-emitters in the Reionization Era

<http://researchonline.ljmu.ac.uk/id/eprint/26147/>

Article

Citation (please note it is advisable to refer to the publisher's version if you intend to cite from this work)

Topping, MW, Stark, DP, Senchyna, P, Chen, Z, Zitrin, A, Endsley, R, Charlot, S, Furtak, LJ, Maseda, MV, Plat, A, Smit, R, Mainali, R, Chevallard, J, Molyneux, S and Rigby, JR (2025) Deep Rest-UV JWST/NIRSpec Spectroscopy of Early Galaxies: The Demographics of C iv and N-emitters

LJMU has developed **LJMU Research Online** for users to access the research output of the University more effectively. Copyright © and Moral Rights for the papers on this site are retained by the individual authors and/or other copyright owners. Users may download and/or print one copy of any article(s) in LJMU Research Online to facilitate their private study or for non-commercial research. You may not engage in further distribution of the material or use it for any profit-making activities or any commercial gain.

The version presented here may differ from the published version or from the version of the record. Please see the repository URL above for details on accessing the published version and note that access may require a subscription.

For more information please contact researchonline@ljmu.ac.uk

<http://researchonline.ljmu.ac.uk/>



Deep Rest-UV JWST/NIRSpec Spectroscopy of Early Galaxies: The Demographics of CIV and N-emitters in the Reionization Era

Michael W. Topping¹, Daniel P. Stark², Peter Senchyna³ , Zuyi Chen¹ , Adi Zitrin⁴ , Ryan Endsley⁵ , Stéphane Charlot⁶ ,
Lukas J. Furtak⁴ , Michael V. Maseda⁷ , Adele Plat¹, Renske Smit⁸ , Ramesh Mainali⁹ , Jacopo Chevallard¹⁰ ,
Stephen Molyneux^{8,11}, and Jane R. Rigby¹² 

¹ Department of Astronomy / Steward Observatory, University of Arizona, 933 N Cherry Avenue, Tucson, AZ 85721, USA; michaeltopping@arizona.edu

² Department of Astronomy, University of California, Berkeley, CA 94720, USA

³ The Observatories of the Carnegie Institution for Science, 813 Santa Barbara Street, Pasadena, CA 91101, USA

⁴ Physics Department, Ben-Gurion University of the Negev, P.O. Box 653, Be'er-Sheva 84105, Israel

⁵ Department of Astronomy, University of Texas, Austin, TX 78712, USA

⁶ Sorbonne Université, CNRS, UMR 7095, Institut d'Astrophysique de Paris, 98 bis bd Arago, 75014 Paris, France

⁷ Department of Astronomy, University of Wisconsin-Madison, 475 N. Charter Street., Madison, WI 53706, USA

⁸ Astrophysics Research Institute, Liverpool John Moores University, 146 Brownlow Hill, Liverpool L3 5RF, UK

⁹ Observational Cosmology Lab, Code 665, NASA Goddard Space Flight Center, 8800 Greenbelt Road, Greenbelt, MD 20771, USA

¹⁰ Department of Physics, University of Oxford, Denys Wilkinson Building, Keble Road, Oxford OX1 3RH, UK

¹¹ European Southern Observatory, Karl-Schwarzschild-str. 2, 85748 Garching, Germany

¹² Astrophysics Science Division, Code 660, NASA Goddard Space Flight Center, 8800 Greenbelt Road, Greenbelt, MD 20771, USA

Received 2024 July 30; revised 2024 December 16; accepted 2025 January 6; published 2025 February 18

Abstract

JWST has recently discovered a subset of reionization era galaxies with ionized gas that is metal-poor in oxygen and carbon but heavily enriched in nitrogen. This abundance pattern is almost never seen in lower-redshift galaxies but is commonly observed in globular cluster stars. We have recently demonstrated that this peculiar abundance pattern appears in a compact (≈ 20 pc) metal-poor galaxy undergoing a strong burst of star formation. This galaxy was originally selected based on strong CIV emission, indicating a hard radiation field rarely seen locally. In this paper, we present JWST/NIRSpec observations of another reionization-era galaxy known to power strong CIV emission, the $z = 7.04$ gravitationally lensed galaxy A1703-zd6. The emission-line spectrum reveals this is a metal-poor galaxy ($12 + \log(\text{O}/\text{H}) = 7.47 \pm 0.19$) dominated by a young stellar population ($1.6_{-0.4}^{+0.5}$ Myr) that powers a very hard ionizing spectrum (CIV equivalent width, $\text{EW} = 19.4 \text{ \AA}$, He II $\text{EW} = 2.2 \text{ \AA}$). The interstellar medium is highly enriched in nitrogen ($\log(\text{N}/\text{O}) = -0.6$) with very high electron densities ($8\text{--}19 \times 10^4 \text{ cm}^{-3}$) and extreme ionization conditions rarely seen at lower redshift. We also find intense CIV emission ($\text{EW} \gtrsim 20 \text{ \AA}$) in two new $z \gtrsim 6$ metal-poor galaxies. To put these results in context, we search for UV line emission in a sample of 737 $z \gtrsim 4$ galaxies with NIRSpec spectra, establishing that 40%(30%) of systems with $[\text{O III}] + \text{H}\beta \text{EW} > 2000 \text{ \AA}$ have NIV] (CIV) detections with $\text{EW} > 5 \text{ \AA}$ ($> 10 \text{ \AA}$). These results suggest high N/O ratios, and hard ionizing sources appear in a brief phase following a burst of star formation in compact high-density stellar complexes.

Unified Astronomy Thesaurus concepts: Galaxy abundances (574); Galaxy chemical evolution (580); High-redshift galaxies (734); Galactic and extragalactic astronomy (563); Starburst galaxies (1570)

1. Introduction

Roughly a decade ago, deep near-infrared spectroscopy began to provide our first window on the rest-frame ultraviolet (UV) spectra of $z \gtrsim 6$ galaxies. This early glimpse revealed strong line emission from highly ionized species of carbon and oxygen, with intensities significantly in excess of those at lower redshifts (D. P. Stark et al. 2015a, 2015b, 2017; N. Laporte et al. 2017; R. Mainali et al. 2017; T. A. Hutchison et al. 2019; M. W. Topping et al. 2021). This was most clearly seen in two gravitationally lensed galaxies showing strong nebular CIV $\lambda\lambda$ 1548, 1550 emission, RXCJ2248-ID at $z = 6.11$ (R. Mainali et al. 2017; K. B. Schmidt et al. 2017), and A1703-zd6 at $z = 7.045$ (D. P. Stark et al. 2015a). The presence of triply ionized carbon requires a supply of 48 eV photons rarely seen in star-forming galaxies at lower redshifts. Some argued this may be indicative of a population of very-

low-metallicity stars (D. P. Stark et al. 2015a; R. Mainali et al. 2017), whereas others suggested the detections may point to the presence of narrow-line active galactic nuclei (AGNs) in relatively faint reionization era galaxies (K. Nakajima et al. 2018). With ground-based instrumentation, our ability to delineate the nature of the ionizing sources in these systems was long stunted by limited wavelength coverage ($\lambda_{\text{rest}} \lesssim 2000 \text{ \AA}$) imposed by our atmosphere.

The launch of JWST has fundamentally altered our ability to characterize the spectra of reionization era galaxies (e.g., D. Schaerer et al. 2022b; K. Z. Arellano-Córdova et al. 2022; H. Katz et al. 2023; J. R. Trump et al. 2023; E. Curtis-Lake et al. 2023; S. Fujimoto et al. 2023). Early observations have confirmed that hard radiation fields are present in a number of early galaxy spectra (e.g., A. J. Bunker et al. 2023; M. Tang et al. 2023; S. Tacchella et al. 2023; M. Castellano et al. 2024). Perhaps most striking has been the $z = 10.60$ galaxy GNz11 reported in A. J. Bunker et al. (2023). In addition to strong high ionization emission lines, the rest-UV spectrum reveals strong NIV] $\lambda\lambda$ 1483, 1486 and NIII] λ 1750 emission, indicating gas that is heavily enriched in nitrogen relative to

oxygen ($\log(\text{N}/\text{O}) = -0.38$) and carbon ($\log(\text{N}/\text{C}) \sim -0.5$) in spite of being very metal-poor ($12 + \log(\text{O}/\text{H}) = 7.82$; A. J. Cameron et al. 2023b). This abundance pattern is extremely rare in lower-redshift galaxies, suggesting a chemical evolution pathway that is perhaps unique to the reionization era, conceivably requiring a population of very (or super-) massive stars ($\gtrsim 10^{2-3} M_{\odot}$; J. S. Vink 2023; C. Charbonnel et al. 2023; R. Marques-Chaves et al. 2024; D. Nandal et al. 2024a) or punctuated star formation histories (SFHs; C. Kobayashi & A. Ferrara 2024). Similar abundance ratios are seen in many globular cluster stars (e.g., R. Gratton et al. 2004; P. Senchyna et al. 2024; E. Carretta et al. 2005), potentially indicating a connection between the stars being formed in GNz11 and those formed in the second-generation stellar populations of globular clusters (e.g., N. Bastian & C. Lardo 2018). The GNz11 spectrum also shows evidence for very high electron densities ($\gtrsim 10^5 \text{ cm}^{-3}$), 2 orders of magnitude above those seen in star-forming galaxies at lower redshift (e.g., R. L. Sanders et al. 2016), potentially reflecting conditions associated with a dense broad-line region or nuclear star cluster surrounding an AGN (P. Senchyna et al. 2024; R. Maiolino et al. 2024a).

Whether the peculiar abundance pattern of GNz11 is common in the reionization era is not known. It is also not clear whether the nitrogen-enhancement is somehow linked to the presence of the hard ionizing sources and high electron densities that are also seen in GNz11. But without a larger sample of such galaxies, it is impossible to adequately understand the physical mechanisms driving the origin of the abundance pattern. A natural place to begin investigation of these questions is the two $z \gtrsim 6$ galaxies with CIV detections from ground-based telescopes, both of which are extremely bright in the continuum ($J = 24.8\text{--}25.9$) allowing high signal-to-noise ratio (S/N) views of the ionizing sources and gas abundance pattern. While it was clear prior to JWST that both systems had a population of hard ionizing sources, it was not known whether they also had ionized gas that was nitrogen enhanced or elevated in density similar to GNz11. In JWST Cycle 1, we obtained NIRSpect R=1000 spectroscopy targeting both the $z = 6.11$ (R. Mainali et al. 2017; K. B. Schmidt et al. 2017) and the $z = 7.05$ (D. P. Stark et al. 2015b) CIV emitters (program ID: 2478). The observations were designed to extend the spectroscopic coverage of these sources into the rest-optical for the first time, providing insight into the metal content of early galaxies with hard radiation fields. We also obtained very deep rest-UV NIRSpect observations, providing complete coverage of the emission lines (and continuum) at $\simeq 1200\text{--}2000 \text{ \AA}$. This far-UV (FUV) spectral window contains a suite of features sensitive to the origin of the radiation field, the electron density, and the level of nitrogen enhancement.

In the first paper from this program, M. W. Topping et al. (2024a) presented a detailed investigation of the NIRSpect observations of RXCJ2248-ID, the $z = 6.11$ CIV emitter. The spectrum confirmed the presence of a hard radiation field with strong emission from numerous highly ionized species (i.e., CIV $\lambda\lambda 1548, 1550$, He II $\lambda 1640$). The rest-optical spectrum was found to be similarly extreme, with very large [OIII]+H β equivalent width (EW; 3100 \AA) only seen in the upper 2% of $z \simeq 6 - 9$ galaxies (e.g., J. Matthee et al. 2023; R. Endsley et al. 2024). In spite of the strength of [OIII] and the hydrogen recombination lines, the [OII] doublet is found to be very weak, suggesting an [OIII]/[OII] flux ratio (hereafter O32) of 184,

well in excess of nearly any star-forming galaxy previously studied at lower redshifts. M. W. Topping et al. (2024a) reported that the various spectral features are consistent with being powered by a young (1.8 Myr) stellar population in a $\lesssim 20 \text{ pc}$ region with ionized gas that is metal-poor ($12 + \log(\text{O}/\text{H}) = 7.43$) and extremely dense ($6\text{--}31 \times 10^4 \text{ cm}^{-3}$). The RXCJ2248-ID spectrum shows emission from [NIII] and [NIV], revealing a nitrogen-enhanced abundance pattern ($\log(\text{N}/\text{O}) = -0.39$) that is similar to that found in GNz11. However, in RXCJ2248-ID no spectral signatures were found that demand the presence of an AGN, suggesting that the high-ionization lines may likely originate from a low-metallicity population of massive stars.

Based on these results, M. W. Topping et al. (2024a) suggested that the nitrogen enhancement seen at $z \gtrsim 6$ may be produced in the dense clusters that form during a strong burst of star formation, a phase that many reionization era galaxies go through (S. R. Furlanetto & J. Mirocha 2022; J. Mirocha & S. R. Furlanetto 2023; V. Strait et al. 2023; T. Dome et al. 2024; R. Endsley et al. 2024). In this framework, the hard ionizing agents would be produced during the burst, and the high electron densities would reflect the extreme dense gas conditions associated with the burst. If this picture applies universally, we should also see nitrogen enhancements and high electron densities in the $z = 7.05$ galaxy Abell 1703-zd6 (hereafter A1703-zd6), the other CIV emitting primary target in our Cycle 1 program. In this paper, we present the deep NIRSpect observations of A1703-zd6. Our MSA design includes many additional bright lensed $z \gtrsim 6$ galaxies, which we also describe in this paper. Our primary goals are twofold. First we seek to understand more about what drives hard radiation fields in a subset of early galaxies. Second, we seek to understand if the hard radiation fields are linked in some way to spectra like GNz11, with nitrogen enhancements and high electron density. To put these results in context, we will additionally present constraints on the fraction of early galaxies with CIV and [NIV] lines in a large database of publicly available NIRSpect spectra.

The structure of this paper is as follows. Section 2 provides an outline of the observations and data analysis, and discusses our measurement methods. In Section 3 we describe the spectra of each object in our sample, and we discuss the derived properties of the sample in Section 4. Section 5 discusses the properties of these sources in the context of the reionization-era galaxy population. Finally, we provide a discussion in Section 6, followed by a summary and brief conclusions in Section 7. Throughout this paper, we assume a cosmology with $\Omega_m = 0.3$, $\Omega_{\Lambda} = 0.7$, and $H_0 = 70 \text{ km s}^{-1} \text{ Mpc}^{-1}$, and adopt solar abundances from M. Asplund et al. (2009; i.e., $Z_{\odot} = 0.014$, $12 + \log(\text{O}/\text{H})_{\odot} = 8.69$). All magnitudes are provided using the AB system (J. B. Oke & J. E. Gunn 1983).

2. Data and Measurements

In this section we provide an overview of the program from which our data are derived (Section 2.1), along with the methods used to measure emission and absorption lines from the spectra. In Section 2.2 we detail the methods used to infer properties of the stellar populations within each galaxy.

2.1. Observations and Reduction

Spectroscopic data were obtained using JWST/NIRSpect in Multi-Object Spectroscopy (MOS) mode targeting two lensing

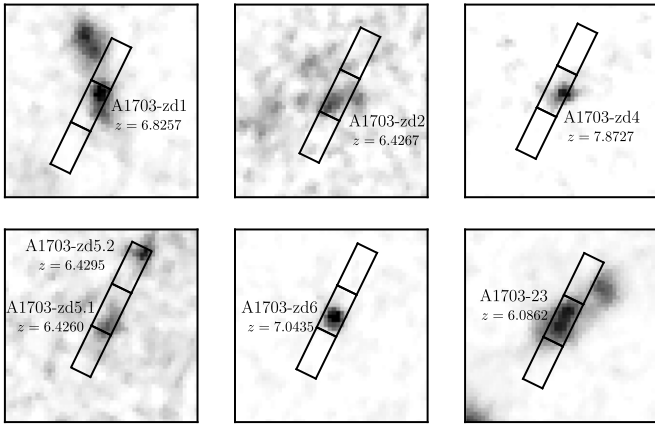


Figure 1. J_{125} -band images for each of the objects in our spectroscopic sample. Each postage stamp is $2''$ on a side and displayed in an orientation such that north is up and east is to the left. We overlay the position of the NIRSpect shutter in the postage stamp of each object. The listed redshifts were measured from the NIRSpect spectrum.

fields, Abell 1703 (RA: 198.7636, Dec: +51.821, S. W. Allen et al. 1992) and RXCJ2248-4431 (RA: 342.17972, Dec: -44.5330; L. Guzzo et al. 2009), as part of Cycle 1 program ID 2478 (PI: Stark). In the Abell 1703 field, we obtained data using the G140M/F100LP and G395M/F290LP dispersing modes with total exposure times of 6653 s and 1576 s, respectively, using the NRSIRS2RAPID readout mode. Following the position angle (PA) assignment of the observations, the MSA pointing centers were defined based on the locations of our highest-priority targets. For the observations in the Abell 1703 field presented in this analysis, we required that a microshutter slit be placed on A1703-zd6, which was previously spectroscopically confirmed to lie at $z = 7.045$ based on $\text{Ly}\alpha$ (M. A. Schenker et al. 2012), CIV, and OIII] (D. P. Stark et al. 2015a). We additionally required that the location of A1703-zd6 on the MSA would enable continuous wavelength coverage from $\text{Ly}\alpha$ to CIII] $\lambda\lambda 1907, 1909$ (9730Å–15530Å in the observed frame) in G140M, and [OII] $\lambda\lambda 3727, 3729$ to [OIII] $\lambda 5007$ (29980Å–40280Å in the observed frame) in G395M. The final MSA design was configured to fit these constraints and maximize the number of additional high-priority targets, which comprise a sample of z and i -drop galaxies selected to lie at $z \simeq 6$ (J. Richard et al. 2009; L. D. Bradley et al. 2012; R. Smit et al. 2014). Throughout this paper, we refer to the additional high-priority targets as A1703-zd2, A1703-zd5.1, A1703-zd5.2, A1703-zd4, and A1703-23 (see Table 1). Each slit placed upon the targets was composed of three microshutter slitlets, and we obtained data using the standard three-nod pattern, with one exposure for each nod position (Figure 1).

We reduced the spectroscopic data set using a pipeline composed of standard STScI tools (H. Bushouse et al. 2024)¹³ in addition to custom-made routines. The initial processing of the raw uncalibrated (*_uncal.fits) frames included a bias and dark current correction, as well as ramp fitting to the groups yielding the mean count rate in each pixel. During this stage, jumps in consecutive groups resulting from cosmic rays are identified and masked, including significant events such as “snowballs” and “showers.” The resulting full-frame 2D images were corrected for $1/f$ noise using the NSCLEAN

Table 1
Sample of Galaxies Observed with NIRSpect in Abell 1703

ID	R.A.	Decl.	H ₁₆₀	μ	z_{spec}
A1703-zd1	198.747582	+51.833604	24.0	$3.1^{+0.3}_{-0.3}$	6.8257
A1703-zd2	198.777070	+51.821802	24.9	$19.9^{+7.1}_{-7.0}$	6.4267
A1703-zd5.1	198.782392	+51.819382	25.7	$33.6^{+14.0}_{-13.7}$	6.4260
A1703-zd5.2	198.782206	+51.819568	25.3	$33.5^{+17.8}_{-16.9}$	6.4295
A1703-23	198.755951	+51.807251	23.8	$3.0^{+0.2}_{-0.2}$	6.0862
A1703-zd4	198.780017	+51.839995	25.4	$2.0^{+0.1}_{-0.1}$	7.8727
A1703-zd6	198.754233	+51.834663	25.9	$3.9^{+0.1}_{-0.2}$	7.0435

Note. H-band magnitudes are from L. D. Bradley et al. (2012), except for A1703-23, for which we use values from J. Richard et al. (2009).

(B. J. Rauscher 2024) package, and the 2D spectrum traced out by each object was cut out from all of the full-frame exposures. We applied a flat-field correction, a wavelength solution, and an absolute photometric calibration using the updated Calibration Reference Data System context to the cutout spectra for each exposure of every object. We subtracted the background from each exposure following the nodding pattern described above. The background-subtracted exposures were then interpolated onto a common wavelength grid. Each nodded exposure of the targets was then background subtracted and combined including the rejection of pixels that have been flagged in previous reduction stages. These 2D exposures for each object were then interpolated onto a common wavelength grid and combined to produce the final spectrum. We fit the spatial profile of each 2D spectrum, and used the fitting information to perform an optimal extraction (K. Horne 1986), yielding the final 1D spectra.

We corrected the emission from each lensed image for the effects of magnification. Our lens model builds on the model published by A. Zitrin et al. (2010), which used the Light-Traces-Mass approach and included a set of 16 multiply imaged systems to constrain the model, most of which had spectroscopic redshifts and were previously known (see J. Richard et al. 2009; M. Limousin et al. 2008). Here we rerun the model using a parametric lens modeling code, namely a revision of the A. Zitrin et al. (2015) parametric pipeline, which has been extensively used in recent JWST results (e.g., M. Pascale et al. 2022, 2025; L. J. Furtak et al. 2023; A. K. Meena et al. 2023). The model consists of two principal components: cluster galaxies and larger-scale dark matter halos. Cluster galaxies are modeled as double pseudo isothermal ellipsoids (Á. Elíasdóttir et al. 2007), scaled by their luminosity following common scaling relations (e.g., E. Jullo et al. 2007). Two dark matter haloes are incorporated, each modeled as a pseudo isothermal elliptical mass distribution (e.g., C. R. Keeton 2001). One halo is initially centered on the brightest cluster galaxy (BCG) but is allowed to roam around the BCG center, with the exact position optimized in the minimization procedure. A second halo is set on a second bright cluster galaxy north–northwest of the BCG, at [13:15:03.1829, +51:49:56.629]. The mass of the BCG and this second bright galaxy, as well as a third, central galaxy at [13:15:07.8290, +51:48:57.955], are modeled independently of the scaling relation, allowing for some more freedom. In the minimization, the redshifts of the photometric-redshift systems, i.e., those lacking a spectroscopic redshift, are left free to be optimized as well. The minimization is performed in the source

¹³ <https://github.com/spacetelescope/jwst>

Table 2
Derived and Measured Quantities for Galaxies Observed with NIRSpec in Abell 1703

ID	z_{spec}	$\log(M/M_{\odot})$	$\log(\text{SFR}/M_{\odot}\text{yr}^{-1})$	Age (Myr)	τ_{ν}	[OIII] + H β EW (\AA)	CIV EW (\AA)
A1703-zd1	6.8257	9.05 \pm 0.22	1.48 $^{+0.36}_{-0.32}$	37 $^{+27}_{-16}$	0.08 $^{+0.01}_{-0.03}$	1290 \pm 90	... ^a
A1703-zd2	6.4267	7.52 \pm 0.47	0.25 $^{+0.59}_{-0.53}$	17 $^{+18}_{-7}$	0.04 $^{+0.06}_{-0.03}$	1579 \pm 450	31.6 \pm 7.0
A1703-zd5.1	6.4260	7.74 \pm 0.77	-0.34 $^{+1.06}_{-1.37}$	70 $^{+117}_{-55}$	0.16 $^{+0.12}_{-0.13}$	443 \pm 162	< 4.3
A1703-zd5.2	6.4295	8.17 \pm 0.71	0.67 $^{+0.95}_{-1.06}$	23 $^{+45}_{-17}$	0.02 $^{+0.08}_{-0.01}$	1137 \pm 210	10.5 \pm 1.0
A1703-23	6.0862	9.54 \pm 0.16	1.40 $^{+0.29}_{-0.21}$	150 $^{+33}_{-61}$	0.17 $^{+0.04}_{-0.04}$	584 \pm 34	< 1.9
A1703-zd4	7.8727	8.50 \pm 0.27	1.06 $^{+0.52}_{-0.45}$	23 $^{+27}_{-13}$	0.07 $^{+0.04}_{-0.04}$	1895 \pm 520	< 4.9
A1703-zd6	7.0435	7.70 \pm 0.24	1.49 $^{+0.29}_{-0.26}$	1.6 $^{+0.5}_{-0.4}$	0.01 $^{+0.01}_{-0.01}$	4116 \pm 690	19.4 \pm 1.4

Notes. Reported stellar population properties are derived from BEAGLE SED fitting, and have been corrected for the effects of gravitational lensing (see Section 2).

^a CIV feature displays significant P-Cygni profile (see Section 3.2).

plane via a long Markov Chain Monte Carlo, and the final model has a (lens-plane) image reproduction rms of 0%–8.

Emission line fluxes, centroids, and widths were measured by fitting Gaussian profiles to the observed features. For emission lines that are isolated, we fit a model of a single feature, while emission lines in close proximity in wavelength were fit simultaneously. All of the emission-line fitting was provided an initial estimate of the redshift, and its centroid was allowed to vary within one resolution element for emission lines that trace the systemic redshift, and within 500 km s⁻¹ for resonance and absorption lines. In the case of multiple simultaneous line fits, the best-fit redshift was allowed to vary; however, the spacing between the lines was fixed. In some cases, such as for [OIII] $\lambda\lambda$ 3727, 3729 and NIII] λ 1750, the lines are significantly blended, and line fluxes were measured by integrating over the combined profiles. The continuum level for each line was measured by fitting a linear component to spectral windows on either side of the line. We obtained uncertainties on each property (flux, centroid, FWHM, and EW) by first creating 5000 mock spectra that were derived by perturbing the observed spectrum by its corresponding error spectrum. We repeated the above fitting procedure on each of the mock spectra, and assigned uncertainties based on the inner 68th percentile of the recovered distributions of each property.

2.2. Stellar Populations from SED Fitting

Before analyzing the emission line properties, we investigate the basic physical properties of our sample using synthesized broadband photometry from the spectra, following a similar approach to that presented in M. W. Topping et al. (2024a). For consistency with previous works, we derive photometry based on the JWST/NIRCam filter throughputs and fit the resulting broadband fluxes using spectral energy distribution (SED) models. The A1703 sample was observed using the G140M and G395M gratings, which completely encompass the JWST/NIRCam F115W, F150W, F335M, F356W, F410M, and F444W filters. As such, we utilized synthesized photometry in only these filters for the SED fitting, with the redshift of each object fixed to its spectroscopic value. Briefly, we fit the resulting photometry of both objects using BayEsiAn Analysis of GaLaxy sEds (BEAGLE; J. Chevallard & S. Charlot 2016). These models implement updated models of G. Bruzual & S. Charlot (2003), which include nebular emission using the prescription detailed in J. Gutkin et al. (2016). We assume a constant star formation history (CSFH) with a minimum age of 1 Myr, and adopt a uniform prior on metallicity (ionization

parameter) within the range $\log(Z/Z_{\odot}) \in [-2.24, 0.3]$ ($\log(U) \in [-4, -1]$). Finally, we assume an attenuation law following that of the SMC (Y. C. Pei 1992), and a fixed dust-to-metal ratio of $\xi_d = 0.3$. Throughout this analysis, we adopt galaxy properties (e.g., stellar mass, star formation rate, SFR) that have been corrected for gravitational lensing using the magnification factors provided in Table 2. By assuming a CSFH, the inferred stellar population parameters are representative of the most recent episode of star formation, which will dominate the emission in the rest-frame UV and optical. This modeling does not account for the possibility that each galaxy hosts a significant older stellar population, which could lead to a significant underestimate of properties such as the stellar mass and SFR (e.g., L. Whittler et al. 2023). However, this possibility will not significantly impact any of our conclusions.

We present the model properties that reproduce the SEDs in Table 2 and display the best-fit SEDs in Appendix B. The A1703 $z > 6$ sample spans a factor of ~ 170 stellar mass and ~ 70 in SFR, ranging from $\log(M/M_{\odot}) = 7.70 - 9.54$ and $\log(\text{SFR}/M_{\odot}\text{yr}^{-1}) = -0.34 - 1.49$, respectively. In Figure 2 we show the SFRs of our sample as a function of their stellar mass along with the larger sample of $z \simeq 6-9$ LBGs from R. Endsley et al. (2024). Our sample roughly extends over the full range of SFRs spanned by the broader $z \gtrsim 6$ population at $\log(M/M_{\odot}) \gtrsim 8$. When assuming a CSFH, we find the youngest galaxy has a CSFH age of just 1.6 Myr, while the oldest system has an age of 150 Myr. This suggests that our spectra are sampling galaxies dominated by a very young stellar population in addition to those that may have a significant contribution from more evolved stars. Additionally, the best-fit SEDs imply that our sample has a low average dust content, which is consistent with the typically blue UV slopes observed for galaxies during this epoch (e.g., M. W. Topping et al. 2024b; F. Cullen et al. 2023). However, the emission of some objects in our sample (e.g., A1703-zd4, A1703-23) is best modeled by SEDs that include a nonzero amount of attenuation. In the following Section, we describe the spectrum of each galaxy in our sample.

3. Spectroscopic Properties

In this Section we describe the spectroscopic properties of each object in our sample. Our focus will be on emission and absorption line measurements (i.e., EWs, line ratios), building an empirical physical picture for each individual galaxy. We will then build on and synthesize these results in Section 4, calculating gas-phase properties (i.e., electron densities,

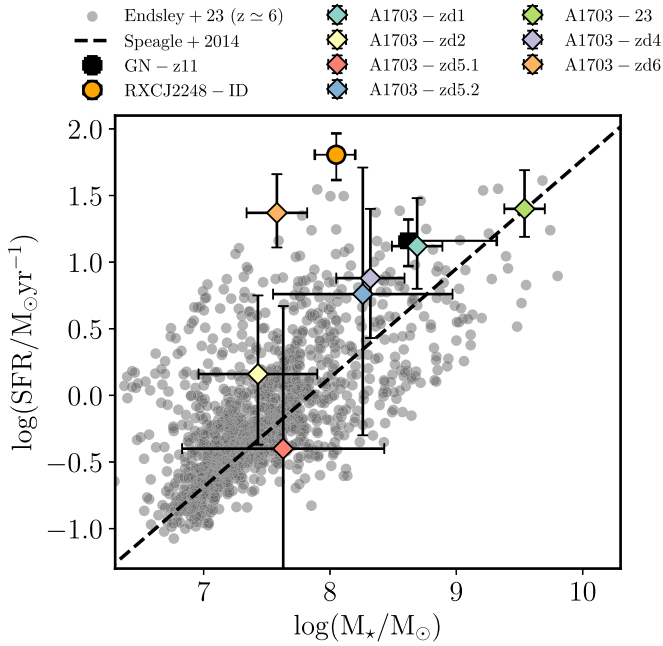


Figure 2. Star formation rate (SFR) versus stellar mass for the two primary targets discussed in this work (violet and orange points) inferred from the BEAGLE SED fitting. We compare to the values inferred for GN-z11 (black square; A. J. Bunker et al. 2023) and RXCJ2248-ID (orange circle; M. W. Topping et al. 2024a), in addition to a population of star-forming galaxies at $z \sim 6-9$ identified by R. Endlesley et al. (2024; gray circles). For reference, we display the “main sequence” derived by J. S. Speagle et al. (2014) calculated at $z = 6$. Our primary targets lie at significantly elevated SFR relative to the main sequence and the population of early star-forming galaxies at fixed stellar mass.

abundance patterns) using the empirical measurements reported in this Section.

Figure 3 presents spectra of the A1703 galaxies in the rest-UV and rest-optical, at wavelengths where lines are commonly detected. Line fluxes and EWs measured following the methods outlined in Section 2.1 are provided in Table 6 for the G140M spectra, and Table 7 for the G395M spectra. Multiple emission lines are detected in each galaxy. We also detect absorption lines in the two brightest continuum sources (A1703-zd1 and A1703-z3).

3.1. A1703-zd6

A1703-zd6 was identified as a bright ($H = 25.9$) z -band dropout, moderately lensed ($\mu = 3.9^{+0.1}_{-0.2}$) by the foreground Abell 1703 cluster (L. D. Bradley et al. 2012). M. A. Schenker et al. (2012) confirmed the redshift ($z = 7.045$) via detection of strong Ly α emission ($EW = 65 \pm 12 \text{ \AA}$) with Keck/NIRSpec. Motivated by the discovery of high-ionization UV lines in metal-poor $z \simeq 2-3$ galaxies (e.g., D. K. Erb et al. 2010; L. Christensen et al. 2012; D. P. Stark et al. 2014), a Keck/MOSFIRE J-band spectrum was subsequently obtained covering rest-frame 1433-1680 \AA . The observations revealed very strong nebular CIV emission at 1.2458 μm ($\lambda 1548$) and 1.2474 μm ($\lambda 1550$), indicating the presence of a hard ionizing spectrum rarely seen in lower-redshift star-forming galaxies (D. P. Stark et al. 2015a). The R=1000 NIRSpec spectrum presented in this paper covers the rest-UV (9700-18900 \AA) and rest-optical (28700-52700 \AA), providing a new window on the ionizing agents and ionized gas in A1703-zd6. Below we will discuss the lines measured in the spectrum and compare to

NIRSpec observations of RXCJ2248-ID (M. W. Topping et al. 2024a), the other $z \gtrsim 6$ CIV emitting galaxy known prior to JWST.

The rest-optical spectrum (Figure 3) shows very prominent Balmer lines ($H\beta$, $H\gamma$, $H\delta$, $H\epsilon$) and strong [OIII] nebular ($\lambda\lambda 4959, 5007$) and auroral ($\lambda 4363$) emission, yielding a systemic redshift of $z = 7.0435$. The $H\beta$ EW (423.8 \AA) is not only at the high end of values seen at $z \gtrsim 6$ (e.g., G. Roberts-Borsani et al. 2024) but is also larger than that found in the vast majority of extreme emission-line galaxies found at lower redshifts (e.g., M. V. Maseda et al. 2018; M. Tang et al. 2019). The [OIII] $\lambda\lambda 4959, 5007$ EW is similarly elevated (3692 \AA), matched by a small number of known $z \gtrsim 6$ galaxies in existing JWST surveys (M. Tang et al. 2023; M. Llerena et al. 2023; K. Boyett et al. 2024). Indeed, the [OIII]+ $H\beta$ EW (4116 \AA) is in the upper 0.5% of values seen in the reionization-era population (J. Matthee et al. 2023; R. Endlesley et al. 2024). The stellar population synthesis models described in Section 2.2 reproduce the strong optical lines with an [OIII] + $H\beta$ EW of $3930 \pm 370 \text{ \AA}$, provided the age of the stellar population dominating the light is very young (1.6 Myr) and the ionization parameter is very large ($\log(U) = -1.7 \pm 0.3$). In this picture, the strong CIV emission is powered by a hard radiation field associated with an extremely young stellar population formed in a recent burst of star formation (Figure 2).

In contrast to the strong nebular emission described above, the A1703-zd6 spectrum does not reveal detection of the [OII] doublet. The lower-ionization state gas (if present) appears to not be intense in its emission. The ratio of [OIII] and [OII] fluxes in A1703-zd6 is found to be > 36 (3σ), well above the typical values at $z \gtrsim 6$ (median O32 $\simeq 10$ in existing spectroscopic samples; M. Tang et al. 2023; A. J. Cameron et al. 2023b; R. L. Sanders et al. 2023). Such a large O32 value is qualitatively consistent with the well-known relationship between [OIII] EW and O32 (M. Tang et al. 2019; R. L. Sanders et al. 2020), whereby extreme ionization conditions (large O32) tend to be found in galaxies with very large [OIII] EW. The large flux ratio of [Ne III] and [OII] (> 3.8 ; hereafter Ne3O2) presents more evidence for extreme ionization conditions. The lower limits on the O32 and Ne3O2 ratios in A1703-zd6 are consistent with those measured in RXCJ2248-ID (M. W. Topping et al. 2024a). In RXCJ2248-ID, it was shown that the extremely large O32 value (184) was partially driven by elevated electron densities ($\sim 10^5 \text{ cm}^{-3}$), which result in collisional de-excitation of [OII]. At these high densities, we also expect anomalously strong He I $\lambda 5876$ emission, owing to elevated collisional excitation. A1703-zd6 presents a strong He I $\lambda 5876$ line, with a flux 26% that of $H\beta$. We will demonstrate that the densities of A1703-zd6 are indeed very large in Section 4.1.

The UV continuum slope of the synthesized SED of A1703-zd6 is very blue ($\beta = -2.6$), comparable to galaxies with similar luminosities at $z \gtrsim 6$ (M. W. Topping et al. 2024b; F. Cullen et al. 2023; A. M. Morales et al. 2024). Such blue colors suggest very little reddening from dust, as evidenced by the low optical depth implied by the BEAGLE population synthesis models fits ($\tau_V = 0.01 \pm 0.01$) described in Section 2.2 (see Table 2). The Balmer line flux ratios present a similar picture, with values ($H\gamma/H\beta = 0.57 \pm 0.17$) consistent with those expected from case B recombination (once the appropriate electron temperature and densities are adopted;

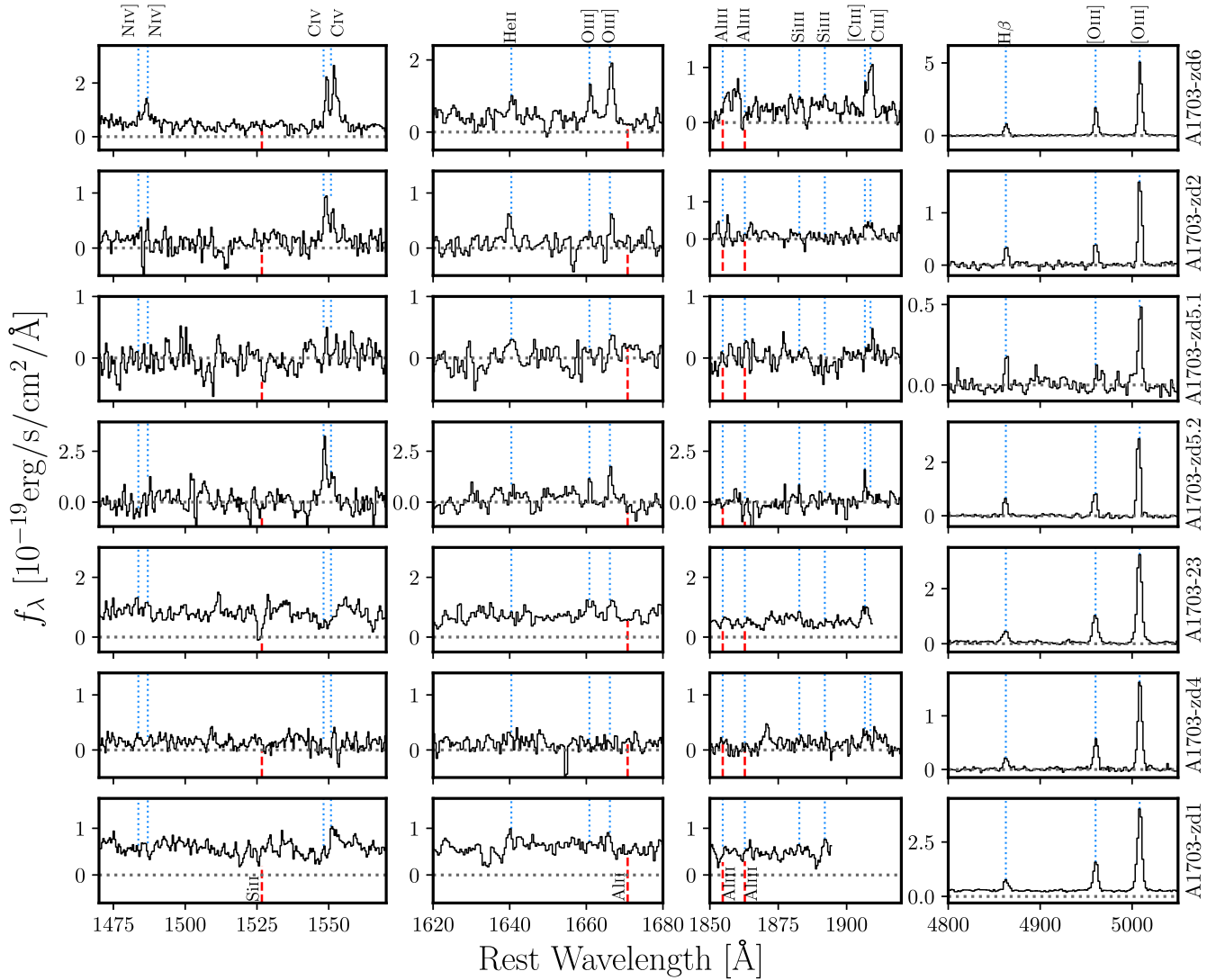


Figure 3. Presentation of the rest-frame UV and optical spectra for the sample of $z > 6$ galaxies in Abell 1703. Each row corresponds to one object, which is labeled on the side of the rightmost panel. Each column is a cutout of the rest-UV spectrum around the wavelengths where prominent features are detected. Vacuum wavelengths are indicated by vertical blue dotted lines rising above each spectrum, which are also labeled along the top row of panels. Transitions typically seen in absorption are indicated by vertical red dashed lines below each spectrum. These absorption lines are labeled along the bottom row of panels.

see Section 4.2). The optical line ratios also indicate the ionized gas is metal poor. We will show in Section 4.2 that detection of auroral lines suggest a gas-phase metallicity of $12 + \log(\text{O}/\text{H}) = 7.47$, corresponding to $6\% Z_{\odot}$.

The NIRSpect UV spectrum of A1703-zd6 (top panel in Figure 3) reveals clear detection of the CIV emission seen with Keck, along with several other intense emission features (NIV], He II, OIII], NIII], CIII]). The NIRSpect R=1000 data reveal more information than was possible with Keck. Both components of the CIV doublet are detected and resolved with NIRSpect, with an integrated strength (EW=19.4 Å) well in excess of what is seen in nearly all lower-redshift star-forming galaxies (P. Senchyna et al. 2019; Y. I. Izotov et al. 2024). As CIV is a resonant line, we expect the lines to be offset from the systemic redshift. We measure centroids of $1.2461\mu\text{m}$ ($\lambda 1548$) and $1.2484\mu\text{m}$ ($\lambda 1550$), both indicating the line is shifted by 240 km s^{-1} from systemic. The line profile is distinctly different from RXCJ2248-ID, where the blue component was shown to be significantly attenuated by scattering effects (M. W. Topping et al. 2024a). The ratio of the two components

in A1703-zd6 is near unity, with a doublet ratio of $f_{\text{CIV } \lambda 1548}/f_{\text{CIV } \lambda 1550} = 0.8 \pm 0.2$ (Table 4). This is well below the intrinsic ratio (2), as expected when the blue component is preferentially scattered by outflowing gas. Nonetheless, the mere presence of the blue component suggests A1703-zd6 faces less attenuation to the transfer of CIV photons than RXCJ2248-ID.

The detection of the strong nitrogen line emission in A1703-zd6 follows the recently reported detection in RXCJ2248-ID (M. W. Topping et al. 2024a; see also A. J. Bunker et al. 2023; Y. Isobe et al. 2023; M. Castellano et al. 2024), providing more evidence for a connection between hard ionizing sources and nitrogen enhancement. Both components of the NIV] doublet are detected in A1703-zd6, revealing a total EW of $5.0 \pm 0.7\text{Å}$. The NIV] line profile is very similar to that seen in RXCJ2248-ID, with the red component $2.1 \times$ stronger than the blue component (Figure 4). We will come back to discuss implications for the electron density in Section 4.1. The CIV/NIV] flux ratio in A1703-zd6 (3.1) is slightly greater than that seen in RXCJ2248-ID (2.1). We additionally detect

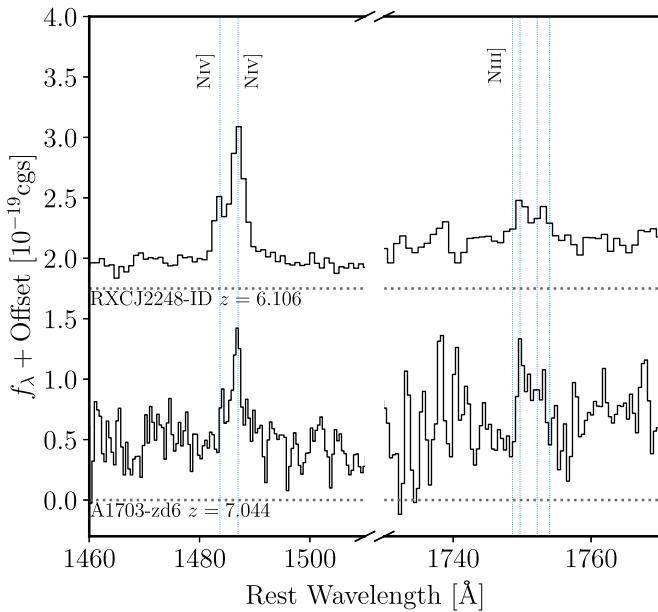


Figure 4. Comparison of nitrogen lines detected in deep NIRSpect G140M spectra of RXCJ2248-ID (M. W. Topping et al. 2024a) and A1703-zd6 (this work) at $z = 6.106$ and $z = 7.044$, respectively. Both spectra have been shifted into the rest frame. The vacuum wavelengths of the NIV] doublet and NIII] multiplet members are indicated by vertical blue lines. The line of zero flux for each spectrum is shown as a horizontal dotted line.

emission from the NIII] quintuplet ($S/N = 3.2\sigma$) with an integrated EW of $3.1 \pm 1.0\text{\AA}$. We will use these detections to constrain the N/O ratio of A1703-zd6 in Section 4.4.

The detection of the auroral OIII] $\lambda\lambda 1660, 1666$ doublet (EW = 11.6 \AA) enables an additional constraint on the electron temperature which we will discuss in Section 4.2. The CIII], CIII] $\lambda\lambda 1907, 1909$ doublet is resolved with a total line strength (EW = 8.8 \AA) that is comparable to what is often seen in metal-poor star-forming galaxies (D. P. Stark et al. 2017; T. A. Hutchison et al. 2019; M. Tang et al. 2021, 2023). The CIV/CIII] flux ratio is well in excess of unity (3.3), suggesting a very hard spectrum. The He II $\lambda 1640$ line is also detected at 6.2σ , indicating a very large EW (6.8 \AA) rare among nearby star-forming galaxies (D. A. Berg et al. 2016, 2019; P. Senchyna et al. 2017). Nevertheless, the UV line ratios appear consistent with expectations for stellar photoionization (Figure 5). We will discuss these comparisons in more detail in Plat et al. (2025, in preparation), but here we mostly note that the hard spectrum is not clearly indicative of an underlying AGN in A1703-zd6.

The deep NIRSpect spectrum confirms the strong Ly α line detected from the ground by M. A. Schenker et al. (2012). The $R \sim 1000$ grating combined with the sensitivity of NIRSpect yields a precise systemic redshift and enables the shape of the Ly α emission line to be accurately characterized. The Ly α detection in A1703-zd6 is presented in Figure 6. The Ly α peak velocity offset measured from the $R \sim 1000$ spectrum is $180 \pm 80 \text{ km s}^{-1}$. This offset is consistent with the median peak velocities observed for strong line emitters at $z > 6.5$, reflecting the attenuation at line center from the increasingly neutral intergalactic medium (IGM) at these redshifts. The Ly α EW ($61.2 \pm 9.0\text{\AA}$) is larger than what has been seen for a majority of moderately luminous $z > 7$ galaxies characterized by NIRSpect (e.g., A. Saxena et al. 2023; M. Tang et al. 2023). We derive the Ly α escape fraction for A1703-zd6 from the

intrinsic Ly α flux inferred as $f_{\text{Ly}\alpha}^{\text{int}}/f_{\text{H}\beta} = 24.6$, which is appropriate for the density and temperature and assuming case B recombination. The resulting escape fraction of $f_{\text{esc}}^{\text{Ly}\alpha} = 0.30 \pm 0.04$ is comparable to typical values at $z \sim 5-6$ (Z. Chen et al. 2024) implying significant transmission through the IGM. This value is well above typical escape fractions at $z \simeq 7$ ($f_{\text{esc}}^{\text{Ly}\alpha} \simeq 0.05$; Z. Chen et al. 2024; G. C. Jones et al. 2024; M. Nakane et al. 2024) consistent with expectations for galaxies situated within ionized sight lines.

Finally, as has been noted previously (L. D. Bradley et al. 2012), the HST imaging of A1703-zd6 demonstrates that it is extremely compact (Figure 1). It is unresolved in the image plane in the J_{125} band, which has a point-spread function FWHM of $0''.12$ (e.g., A. M. Koekemoer et al. 2011). This is consistent with the angular size of the rest-UV continuum trace in the 2D NIRSpect spectrum. These constraints yield an effective radius of $< 120 \text{ pc}$ in the source plane. We constrain the stellar-mass surface density (Σ_{M^*}) from this radius and the stellar mass from the synthesized SED, which demonstrates that A1703-zd6 has a very high concentration of stellar mass ($> 3 \times 10^3 M_{\odot}/\text{pc}^2$). In Figure 7 we compare the mass density of A1703-zd6 to other galaxies and star clusters at high redshift (A. Adamo et al. 2024; E. Vanzella et al. 2023, 2022) and the local Universe (G. Brown & O. Y. Gnedin 2021). A1703-zd6 shows similar characteristics to other high-redshift galaxies sharing several spectroscopic properties (i.e., GNz11 and RXCJ2248-ID A. J. Bunker et al. 2023; M. W. Topping et al. 2024a). Specifically, all of these systems host very young stellar populations, and display high-ionization UV lines including CIV, NIV], and NIII], potentially suggesting that high stellar density (and in particular a large density of very young O stars) may be linked to these properties.

3.2. A1703-zd1

A1703-zd1 is one of the brightest ($H=24.0$) z -band dropouts known (L. D. Bradley et al. 2012), with moderate magnification ($\mu = 3.1_{-0.3}^{+0.3}$) and a blue *Spitzer*/IRAC [3.6]-[4.5] color, suggesting a photometric redshift of $z_{\text{phot}} \simeq 6.6-7.0$ (R. Smit et al. 2014). In spite of its brightness, ground-based rest-UV spectroscopy failed to confirm its redshift, likely indicating A1703-zd1 is characterized by weak Ly α (M. A. Schenker et al. 2012) and fairly weak UV metal lines (D. P. Stark et al. 2015a; R. Mainali et al. 2018). The redshift of A1703-zd1 was eventually confirmed ($z = 6.827$) in the far-IR (FIR), via detection of [CII] $\lambda 158\mu\text{m}$ with the Northern Extended Millimeter Array (NOEMA) (S. J. Molyneux et al. 2022). However no FIR dust continuum was detected with NOEMA (see also D. Schaerer et al. 2015).

The NIRSpect observations of A1703-zd1 reveal a suite of strong rest-optical emission lines ([OII], [NeIII], [OIII], H α , H β , H γ , H δ), indicating a systemic redshift ($z = 6.8257$) consistent with that derived from NOEMA. We do not detect [OIII] $\lambda 4363$ in this spectrum. The combined [OIII]+H β EW is very large (1290 \AA), placing A1703-zd1 among the upper 25% of the [OIII]+H β EW distribution at $z \simeq 6-9$ (e.g., J. Matthee et al. 2023; R. Endsley et al. 2024). Reproducing such large EW optical lines with the synthesized SED requires relatively young stellar populations (37 Myr). The best fit suggests a moderate stellar mass ($\log(M/M_{\odot}) = 9.05 \pm 0.22$), one of the largest in our sample. At such young stellar population ages, ionization-sensitive ratios are usually somewhat elevated

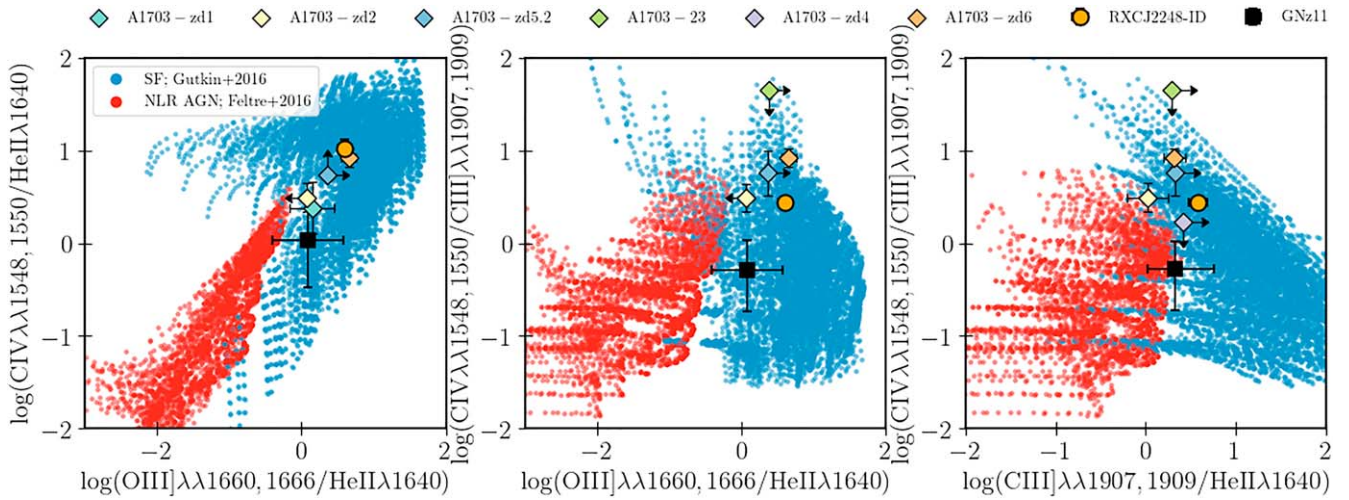


Figure 5. Rest-UV line ratios compared to photoionization models of HII regions within star-forming galaxies (blue points; J. Gutkin et al. 2016), and models where a narrow-line AGN dominates the ionizing radiation field (red points; A. Feltre et al. 2016). Galaxies in our A1703 spectroscopic sample are displayed as the colored diamonds. For comparison, we plot the rest-UV line ratios of RXCJ2248-ID (M. W. Topping et al. 2024a) and GNz11 (A. J. Bunker et al. 2023) as the orange circle and black square, respectively. Line ratios indicated as limits are provided at the 3σ level.

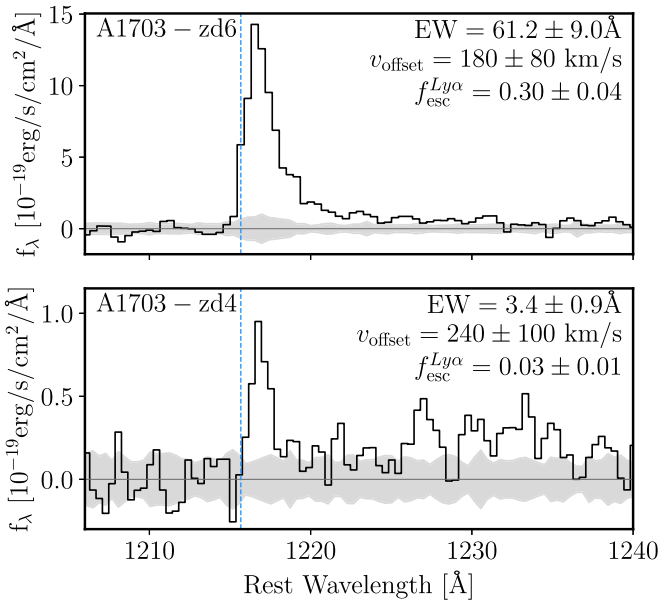


Figure 6. $\text{Ly}\alpha$ profiles of A1703-zd6 (top; Section 3.1) and A1703-zd4 (bottom; Section 3.7). The vacuum wavelength of $\text{Ly}\alpha$ is displayed as a vertical blue line, and the $\text{Ly}\alpha$ EW, systemic velocity offset, and escape fraction for each source are presented at the top right.

(M. Tang et al. 2019), and indeed we find large values of O32 ($8.0^{+0.8}_{-1.0}$) and Ne3O2 ($0.62^{+0.12}_{-0.13}$) in A1703-zd1. The Balmer-line ratios are consistent with the intrinsic values ($H\alpha/H\beta = 2.6^{+0.2}_{-0.3}$, $H\gamma/H\beta = 0.48^{+0.07}_{-0.07}$; Table 3), implying minimal dust attenuation, in agreement with the upper limits on the FIR dust continuum (D. Schaerer et al. 2015; S. J. Molyneux et al. 2022).

The rest-frame UV spectrum reveals confident detection of the continuum ($S/N = 5$ per resolution element) without strong line emission, consistent with expectations from earlier ground-based observations. The nondetections place stringent upper limits on the rest-UV emission line fluxes (see Table 6). At the spectroscopic redshift of A1703-zd1, the G140M spectrum covers 1250–2400Å in the rest frame. In addition, the detector

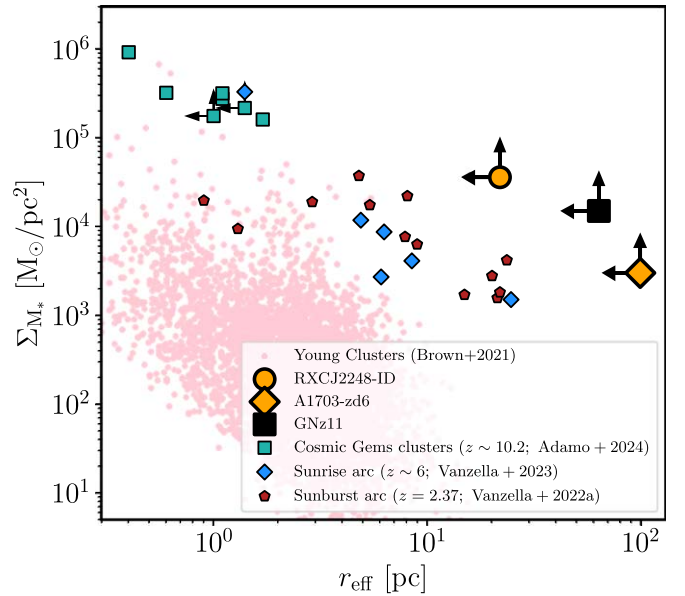


Figure 7. Stellar mass surface density versus effective radius. We display galaxies at $z > 6$ with NIV] detections including A1703-zd6 (orange diamond; this work), RXCJ2248-ID (orange circle; M. W. Topping et al. 2024a), and GN-z11 (black square; A. J. Bunker et al. 2023), in addition to individual star-forming clumps from the Cosmic Gems (A. Adamo et al. 2024), Sunrise arc (E. Vanzella et al. 2023), and the Sunburst arc (E. Vanzella et al. 2022). The pink points provide measurements of individual young star clusters in the local Universe (G. Brown & O. Y. Gnedin 2021). These NIV]-emitting systems have significantly higher Σ_{M^*} at fixed radius compared to local young clusters, and are even elevated compared to individual star-forming clusters at high redshift.

gap falls at rest-frame wavelengths of 1895–2020Å negating our ability to constrain CIII]. Within the observed wavelength coverage, the typical EW limits (3σ) on the UV lines range from 0.7–2.2Å, indicating much weaker emission than the relatively intense optical lines. One example is OIII] $\lambda\lambda 1660, 1666$. The implied total EW limit (< 2.7 Å at 3σ) indicates weaker UV lines than are often seen in galaxies with such large [OIII]+ $H\beta$ EWs (X. Du et al. 2020; M. Tang et al. 2021). This emphasizes that not all strong optical line emitters

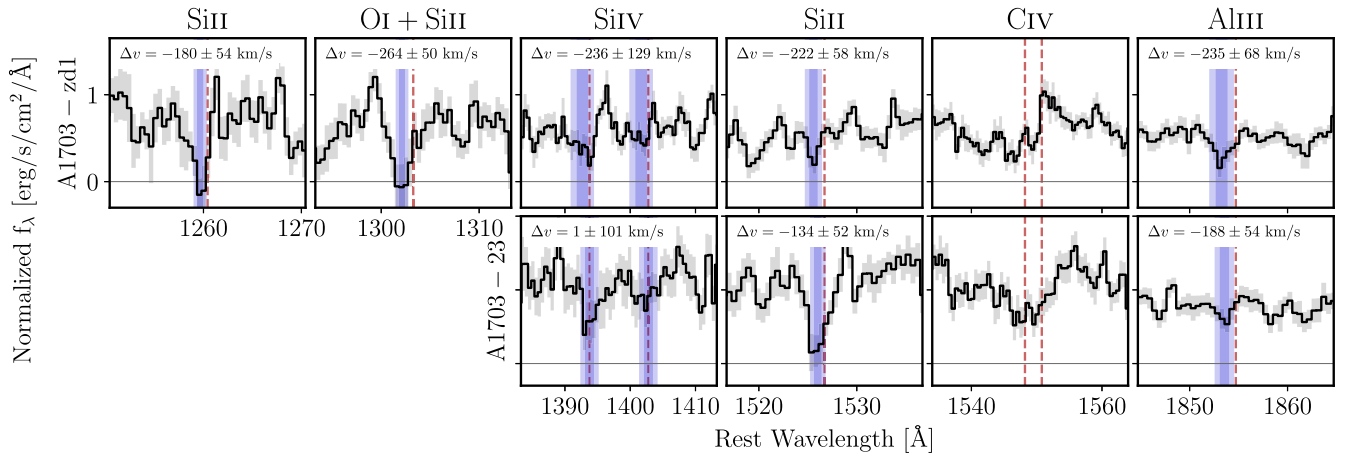


Figure 8. Rest-frame UV absorption lines in the spectrum of A1703-zd1 (top row) and A1703-23 (bottom row). In each panel, the systemic wavelength of the absorption feature is indicated by a red dashed line. The offset of the absorption feature is then listed at the top of each panel. The error spectra are displayed as the gray shaded regions. The vertical dark and light shaded regions illustrate the 1.5σ and 3σ uncertainties for the velocity offset of the line center from systemic.

Table 3
Rest-optical Emission-line Ratios Measured for the A1703 Sample

ID	H α /H β	H γ /H β	O3	O32	Ne3O2	$12 + \log(\text{O}/\text{H})_{\text{strong}}$	$12 + \log(\text{O}/\text{H})_{\text{direct}}$	$f_{[\text{CIII}]}^{1907}/f_{[\text{CIII}]}^{1909}$	$n_e [\text{cm}^{-3}]$
A1703-zd1	$2.6^{+0.2}_{-0.3}$	$0.48^{+0.07}_{-0.07}$	$8.1^{+0.5}_{-0.6}$	$8.0^{+0.8}_{-1.0}$	$0.62^{+0.12}_{-0.13}$	7.88 ± 0.30	> 7.57	–	–
A1703-zd2	–	$0.63^{+0.14}_{-0.16}$	$5.2^{+0.5}_{-0.7}$	–	–	7.35 ± 0.30	> 7.27	$1.10^{+0.21}_{-0.22}$	$(2.0 \pm 1.2) \times 10^4$
A1703-zd5.1	$3.4^{+1.0}_{-1.8}$	< 1.0	$3.1^{+0.9}_{-1.6}$	–	–	7.19 ± 0.43	–	–	–
A1703-zd5.2	$2.8^{+0.2}_{-0.3}$	$0.57^{+0.10}_{-0.11}$	$4.4^{+0.3}_{-0.4}$	–	–	7.26 ± 0.28	7.20 ± 0.28	> 1.48	< 1500
A1703-23	$3.6^{+0.3}_{-0.4}$	$0.25^{+0.09}_{-0.09}$	$7.6^{+0.6}_{-0.7}$	–	–	7.92 ± 0.32	7.84 ± 0.27	–	–
A1703-zd4	–	$0.39^{+0.09}_{-0.10}$	$7.6^{+0.7}_{-1.0}$	$5.6^{+0.5}_{-0.7}$	< 0.21	7.98 ± 0.31	> 7.53	–	–
A1703-zd6	–	$0.57^{+0.17}_{-0.17}$	$6.4^{+0.3}_{-0.4}$	> 36	> 3.6	7.60 ± 0.30	7.47 ± 0.19	$0.49^{+0.19}_{-0.16}$	$(9.4 \pm 4.2) \times 10^4$

Note. Limits are provided at the 3σ level, and “–” symbols indicate that at least one line in the line ratio lacks wavelength coverage in the spectrum. Strong-line metallicities were derived using calibrations of R. L. Sanders et al. (2024) from the O32 ratio if detected, and the low-metallicity branch of the O3 ratio calibration otherwise.

should be expected to power strong UV lines. The presence of weak UV lines in galaxies with very young stellar populations is often a signature of relatively elevated gas-phase metallicities, given the sensitivity of the UV transitions to electron temperature. Strong line calibrations (see Section 4.2) provide some support for this picture, indicating a gas-phase metallicity at the upper end of this sample ($12 + \log(\text{O}/\text{H}) = 7.88$). But detection of auroral lines in the UV or optical will be required to confirm this definitively.

The well-detected UV continuum in the A1703-zd1 spectrum is ideal for recovery of absorption lines. We detect both low-ionization (LIS) and high-ionization (HIS) species. Figure 8 presents a zoomed in view of each detected absorption feature in our spectrum, including SiII λ 1260, OI+SiII λ 1303, SiIV $\lambda\lambda$ 1393, 1402, CIV $\lambda\lambda$ 1548, 1550, and AlIII $\lambda\lambda$ 1854, 1862. We discuss the CIV profile in more detail later in this Section, as it also includes a stellar wind component. We measure EWs of the LIS features in absorption that range from -0.5 to -2.0\AA , and have an average (blueshifted) velocity offset of $-220 \pm 80 \text{ km s}^{-1}$ relative to systemic. The HIS SiIV $\lambda\lambda$ 1393, 1402 line has a lower total EW than each of the LIS lines. However, it is blueshifted from systemic by a similar velocity ($-238 \pm 129 \text{ km s}^{-1}$). These features signify the presence of outflows in both phases, similar to those commonly seen at $z \sim 1-5$ (e.g., A. E. Shapley et al. 2003; C. C. Steidel

et al. 2010; T. Jones et al. 2012; A. J. Pahl et al. 2020; A. Saldana-Lopez et al. 2023). The spectrum highlights that moderately massive galaxies at $z \simeq 7$ do present significant absorption lines with EWs approaching those seen in $z \simeq 3-4$ composites.

While most of the UV absorption lines are relatively narrow with characteristic velocity offsets of $\sim 200 \text{ km s}^{-1}$, a much broader kinematic profile is evident in the CIV complex. The absorption in CIV for this object extends to -2000 km s^{-1} , and is accompanied by prominent redshifted emission. Rather than interstellar gas, a P-Cygni profile of this shape and character is suggestive of formation in the hot stellar winds of massive OB stars. While some high-redshift AGNs exhibit CIV absorption at similar velocities (e.g., J. T. Allen et al. 2011), such systems with absorption velocities matching those of A1703-zd1 typically show much stronger CIV and other rest-UV line emission than what is observed here (A. L. Rankine et al. 2020). Nevertheless, we cannot rule out the possibility of AGN contributions to the spectrum of A1703-zd1. Assuming this profile is indeed stellar, we compare it to models for simple stellar populations (SSPs) from the Charlot & Bruzual population synthesis grids (see Section 2.2, and descriptions in J. Gutkin et al. 2016; A. Plat et al. 2019; P. Senchyna et al. 2022). We compare against SSP ages (2–4 Myr) that span a range of H β EWs similar to that measured for A1703-zd1, and

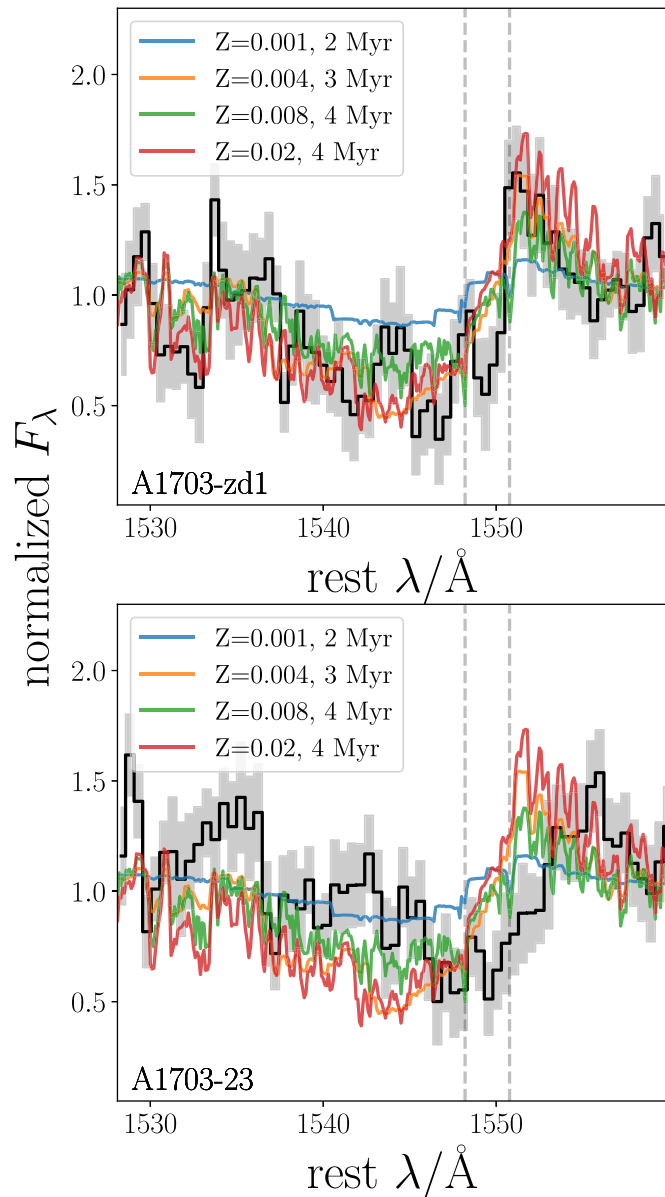


Figure 9. Prominent broad absorption in the resonant CIV 1548,1550 doublet is detected in A1703-zd1 and A1703-23 (spectra in grayscale). Comparison to stellar wind profiles for SSP models from Charlot & Bruzual (colored curves) reveal reasonable agreement with the P-Cygni profile in A1703-zd1, provided a fairly high model stellar metallicity $Z \gtrsim 0.004$ ($Z/Z_{\odot} \gtrsim 20\%$). This suggests we may be viewing a relatively metal-rich galaxy (consistent with the weakness of the UV nebular emission lines), or one in which very luminous stars driving prominent winds are overrepresented. The absorption in A1703-23 is of similar magnitude, but with minimal emission near systemic, in contrast to the stellar wind profiles. Deeper FUV spectroscopy of such galaxies probing other wind lines at similar or higher resolution promises a clearer view of the massive stars populating these systems.

for which these stellar wind contributions are most prominent at a given metallicity. These models include both stellar light and the contribution from nebular continuum in the FUV. Since CIV is the only line with a significant potential stellar contribution at the observed S/N (consistent with model expectations), rather than detailed fitting, we adopt a simple approach of qualitative comparison with the observed profile, normalized to the median flux level at 1570–1580 Å.

The resulting comparison is displayed in Figure 9 (top panel). It is clear that the young very-low-metallicity

($Z = 0.001$) models ($Z/Z_{\odot} = 5\%$) substantially underestimate the observed P-Cygni profile. Slightly older SSP ages at this low metallicity would predict even shallower profiles (A. Vidal-García et al. 2017), even more inconsistent with the observations. At moderately low metallicities ($Z = 0.004 - 0.008$), a range of individual SSP models at different ages are able to match both the absorption and emission profile reasonably well (underscoring the challenge of using resonant wind lines as a robust age and metallicity tracer in isolation). A more complicated SFH will suppress the strength of this P-Cygni profile relative to the SSPs where it is most prominent (P. Senchyna et al. 2022). Thus, in the context of these model predictions, this comparison suggests that a massive star population with metallicities of $\sim 20\%$ solar or above is present. However, the strengths of these modeled stellar wind lines are highly sensitive to the uncertain treatment of winds for very luminous metal-poor massive stars, and to the uncertain proportion of such luminous stars in stellar populations. Indeed, observations of FUV–optical spectra of metal-poor dwarf galaxies in the local Universe hosting young bursts of star formation have revealed markedly stronger C IV wind profiles in comparison to models constrained in detail by other observables (both nebular line emission and FUV photospheric absorption lines; P. Senchyna et al. 2021, 2022). One proposed solution is that these metal-poor young galaxies have an overabundance of luminous massive stars near the Eddington limit (and thus driving strong winds) not captured in the models, perhaps from a high rate of binary mass transfer and mergers occurring on very short timescales. These very massive stars may contribute to stronger wind lines than are captured in the existing models, allowing the wind profiles to be fit at somewhat lower metallicities than shown in Figure 9. A deeper FUV spectrum would reveal or place limits on additional wind features with different sensitivity to burst age, initial mass function (IMF), abundances, and other key properties (e.g., A. Vidal-García et al. 2017; L. J. Smith et al. 2016), allowing for a more robust investigation of the stellar population in A1703-zd1.

3.3. A1703-zd2

A1703-zd2 is a bright ($H = 24.9$) z-band dropout highly magnified ($\mu = 19.9_{-7.0}^{+7.1}$) by the foreground cluster (L. D. Bradley et al. 2012). No previous spectroscopy of this system has been presented in the literature. The NIRSpect rest-optical spectrum is dominated by prominent [OIII] $\lambda\lambda 4959, 5007$ and Balmer ($H\beta$ and $H\gamma$) emission lines, implying a systemic redshift of $z_{\text{spec}} = 6.4267$. At this systemic redshift, the G395M spectrum covers wavelengths of 3900–6500 Å in the rest frame such that strong lines such as [NeIII], [OII], and $H\alpha$ are not observed. The auroral [OIII] $\lambda 4363$ line is not detected at the current S/N of the spectrum. The [OIII] $\lambda 5007$ ($\text{EW} = 1096 \pm 412 \text{ \AA}$) and $H\beta$ ($\text{EW} = 209 \pm 81 \text{ \AA}$) lines are narrow, with FWHMs of 295 km s^{-1} and 320 km s^{-1} , respectively, which is consistent with the instrumental resolution at $R \sim 1000$. The total EW of the [OIII] + $H\beta$ line complex is 1580 Å, which is nearly twice the average value for $z > 6$ galaxies of a similar UV luminosity (R. Endsley et al. 2024) but not as large as in A1703-zd6. Driven by the moderately large rest-optical line EWs, the synthesized photometry is best fit by an SED model (see Section 2.2) with a (CSFH) stellar population age of just 17_{-7}^{+18} Myr.

Table 4
Properties of the CIV Emission Line for Three Objects in Our Sample with a Prominent Nebular Component

Line	A1703-zd2	A1703-zd5.2	A1703-zd6
CIV λ 1548 Flux ^a	10.9 \pm 2.2	39.0 \pm 3.2	23.5 \pm 2.5
CIV λ 1550 Flux ^a	7.0 \pm 1.5	19.9 \pm 3.0	30.0 \pm 2.8
CIV λ 1548 EW	17.1 \pm 4.5 \AA	7.8 \pm 1.4 \AA	8.0 \pm 1.8 \AA
CIV λ 1550 EW	11.0 \pm 3.4 \AA	3.9 \pm 1.3 \AA	10.2 \pm 1.9 \AA
CIV λ 1548 v_{offset}	157 \pm 48 km s ⁻¹	67 \pm 24 km s ⁻¹	220 \pm 26 km s ⁻¹
CIV λ 1550 v_{offset}	127 \pm 62 km s ⁻¹	94 \pm 32 km s ⁻¹	259 \pm 40 km s ⁻¹

Note.

^a Flux measurements are given in units of 10^{-19} erg s⁻¹ cm⁻².

The $H\gamma/H\beta$ ratio ($0.63_{-0.16}^{+0.14}$; Table 3) implies the emission from A1703-zd2 is subject to minimal dust attenuation. The relatively blue UV continuum ($\beta = -2.2$) provides a consistent picture of minimal dust content and low V -band optical depth ($\tau_V = 0.04$). Of the available lines in the optical spectrum, the $[OIII]/H\beta$ ratio ($5.2_{-0.7}^{+0.5}$) is the best probe of the gas-phase conditions. The measured value of $5.2_{-0.7}^{+0.5}$ is below the typical ratios observed at $z \gtrsim 6$ (6-8; R. L. Sanders et al. 2023; M. Tang et al. 2023; A. J. Cameron et al. 2023b), likely suggesting low gas-phase metallicities. Using existing strong line calibrations (Section 4.2), this suggests $12 + \log(O/H) = 7.4$, just $1/20Z_{\odot}$. We infer a stellar mass for A1703-zd2 of only $\log(M/M_{\odot}) = 7.52 \pm 0.47$, which is the lowest value in the sample. A low mass is consistent with the optical line properties described above, given the empirical trends between both attenuation (e.g., A. E. Shapley et al. 2023) and metal content (e.g., M. Curti et al. 2023) derived at high redshift. We return to interpret the oxygen abundance combined with the other galaxy properties in Section 4.2.

The rest-frame UV spectrum displays prominent detections of the high-ionization CIV and He II lines in emission. Emission features commonly used to probe higher energies (i.e., NV and NeIV) are not covered within the wavelength range of the spectrum (1300–2350 \AA). The presence of CIV and He II in emission along with the large optical line EWs in A1703-zd2 is qualitatively similar to trends observed in low-metallicity low-mass galaxies in the local Universe (e.g., P. Senchyna et al. 2017). However, the observed CIV EW of $31.6 \pm 7.0\text{\AA}$ is considerably larger than nearly all such local systems (e.g., P. Senchyna et al. 2019; Y. I. Izotov et al. 2024), and even exceeds the majority of objects at $z > 6$. This clearly indicates this low-mass galaxy is associated with a hard radiation field.

We resolve the CIV doublet profile (Figure 3) into two unresolved emission lines at observed wavelengths of 1.1504 μm and 1.1521 μm . Relative to the systemic redshift, these two doublet members are offset by $+142\text{km s}^{-1}$ (Table 4). We find that the CIV λ 1548 flux is nearly twice that of CIV λ 1550, consistent with the intrinsic doublet ratio. This indicates a low amount of scattering and relatively clear channels for CIV to propagate through the interstellar medium (ISM). This is likely to contribute to the elevated CIV EW measured in this system. The He II λ 1640 line also exhibits a very large EW ($14.0 \pm 6.1\text{\AA}$) that exceeds values measured for even the most extreme CIV emitters locally (Y. I. Izotov et al. 2024) and at high redshift (M. W. Topping et al. 2024a; M. Castellano et al. 2024). These two prominent emission lines characterize the hardness of the ionizing spectrum from 48–54 eV, and their ratio (CIV/He II = 3.1 ± 1.0) is consistent

with models driven by star formation or AGN activity (see Figure 5; A. Feltre et al. 2016; J. Gutkin et al. 2016). Finally, the CIII] (total EW=13.0 \AA) and OIII] (total EW < 12.1 \AA) lines are found to be weaker than both He II and CIV. The UV line ratios implied by these features (Figure 5) are also consistent with both stellar and AGN photoionization. Whereas other sources analyzed in this paper are more confidently in the regime of stellar photoionization, a deeper spectrum of A1703-zd2 is required to put more robust constraints on the powering mechanism of the radiation field.

3.4. A1703-zd5.1

A1703-zd5.1 is one of the faintest ($H = 25.7$) galaxies in our sample and is also the most magnified ($\mu = 33.6_{-13.7}^{+14.0}$) of the $z > 6$ systems identified by L. D. Bradley et al. (2012). As such, it has the lowest luminosity of all high-redshift galaxies we observed in the Abell 1703 field. The galaxy is a close neighbor of A1703-zd5.2 (see Section 3.5 below), situated only 0 $^{\circ}$.5 away from its companion in the image plane. L. D. Bradley et al. (2012) interpreted their close separation as a signature of separate clumps within a single galaxy; however, it is also possible that they are different galaxies currently in the process of merging. Despite the two star-forming components falling within the same slit, we leverage the high spatial resolution of JWST/NIRSpec to extract separate spectra for each system. Here we present the our observations of A1703-zd5.1, while A1703-zd5.2 is described in Section 3.5. Despite the apparent faintness of A1703-zd5.1, NIRSpec confirms detections in $H\beta$, $[OIII]\lambda$ 5007, and $H\alpha$ at a spectroscopic redshift of $z = 6.4260$. We take this as the systemic redshift.

A1703-zd5.1 notably has very low optical-line EWs of $[OIII]\lambda$ 5007 (267 \AA) and $H\alpha$ (157 \AA). The synthesized SED is relatively flat (in f_{ν}) across the rest-UV and rest-optical, suggesting a relatively young stellar population. This source appears to be a spectroscopic example of the weak-line population identified photometrically in R. Endsley et al. (2024). It is challenging to explain these SEDs with simple CSFH models, as young ages generally are accompanied by large EW rest-optical lines. R. Endsley et al. (2023) demonstrated that such systems can be readily explained as having recently experienced a sudden decrease in their star formation activity. To address these complications in A1703-zd5.1, we employ a two-component star formation history (TcSFH; R. Endsley et al. 2024) with the additional flexibility required to fit the observed emission. These models parallel our setup described in Section 2.2, except with an SFH composed of a delayed-tau model ($\text{SFR} \propto t \cdot e^{-t/\tau}$) combined with a decoupled CSFH episode over the most recent 20 Myr.

The TcSFH model provides a much better fit ($\chi^2 = 1.6$) when compared to the CSFH model ($\chi^2 = 9.4$). Furthermore, the best-fit TcSFH SED model implies a light-weighted age of 70 Myr, and stellar mass of just $10^{7.74} M_{\odot}$. The relatively low instantaneous specific star formation rate (sSFR; $3.3/\text{Gyr}^{-1}$) underscores the recent downturn in star formation. The O3 line ratio ($3.1_{-1.6}^{+0.9}$) is the lowest value in our sample, indicative of a very low oxygen abundance ($0.04Z_{\odot}$; see Section 4.2 below). This is perhaps not surprising given the very low luminosity of this galaxy. We note that while low metallicity will contribute to the weak [OIII], it should boost the strength of H α and other Balmer lines (see discussion in R. Endsley et al. 2024). Hence, low metallicity on its own cannot explain the weak emission lines in this galaxy (as evidenced by the poor χ^2 for the CSFH models). The recent downturn in the SFH allowed in the TcSFH models is key for explaining the weakness of both H α and [OIII].

We note that models with ionizing photon escape can also explain the weakness of the emission lines in such SEDs. Following the approach taken in M. W. Topping et al. (2022), we fit the SED using the density-bounded f_{esc} models of A. Plat et al. (2019). In short, these models self-consistently compute the impact of density-bounded HII regions on the continuum and lines for different escape fractions (see A. Plat et al. 2019 and implementation in M. W. Topping et al. 2022). The results indicate that reasonable solutions can be achieved for moderate escape fractions, although the reduced χ^2 (3.3) is not quite as low as for the TcSFH models.

The rest-frame UV spectrum of A1703-zd5.1 is relatively featureless, with no detections in the commonly observed lines (e.g., CIV, He II, CIII). We place tight upper limits on the EWs of these features ranging from 3–6Å (Table 6). The absence of rest-UV emission lines is consistent with the low sSFR inferred from the best-fit TcSFH model described above, which implies that the massive stars that power these lines have begun to disappear following the recent downturn in SFR. We do observe a tentative He II λ 1640 emission line (S/N = 2.5) that appears slightly broadened (FWHM = 450 km s^{-1}) relative to the instrumental line-spread function (see Figure 3). If confirmed, this would potentially indicate a broad stellar He II profile. This would be more challenging to explain in the TcSFH models, where recent star formation is subdominant, but it could be explained by the leakage models, as significant massive star populations would still be present. Ultimately, deeper spectroscopy will be required to constrain the flux and shape of He II in order to discern its origin.

3.5. A1703-zd5.2

A1703-zd5.2 is the brighter ($H = 25.3$) neighbor to A1703-zd5.1, is situated only $0''.5$, and is magnified by a factor of $\mu = 33.5_{-16.9}^{+17.8}$. The rest-optical spectrum reveals significant detection in multiple Balmer lines (H α , H β , H γ , H δ), in addition to [OIII] λ λ 4959, 5007. These lines indicate a systemic redshift of $z_{\text{spec}} = 6.4295$, which is very similar to its close neighbor, A1703-zd5.1. The full extent of the optical spectrum spans from 3850–6680Å in the rest frame, thus lacking constraints on the low-ionization [OII] and [SII] lines. All of the emission lines detected in the rest optical are narrow, with an average FWHM (310 km s^{-1}) that is consistent with the instrumental resolution.

Despite the close proximity between A1703-zd5.1 and zd5.2, the rest-optical spectra differ significantly. The H α

EW ($651 \pm 227\text{Å}$) is over $4 \times$ that of A1703-zd5.1, while the [OIII] λ 5007 EW ($749 \pm 188\text{Å}$) is a factor of 2.7 larger. The observed SED is well fit by models with CSFH stellar population ages of 23_{-17}^{+45} Myr. Each of the Balmer line ratios is consistent with the absence of attenuation from dust, with H α /H β ($2.8_{-0.3}^{+0.2}$) being the most constraining. We draw a similar conclusion from the relatively blue UV-continuum slope ($\beta = -2.4$). The only strong rest-optical line ratio probed by NIRSpec is O3. We measure a low value of $4.4_{-0.4}^{+0.3}$, which suggests the strength of [OIII] is being weakened by the low gas-phase metallicity. The strong line calibration of R. L. Sanders et al. (2023) suggests this value of O3 corresponds to $12 + \log(\text{O}/\text{H}) = 7.26 \pm 0.28$ (Table 3).

The rest-UV spectrum reveals significant CIV emission (Figure 3). We additionally achieve detections at $\gtrsim 5\sigma$ in [OIII] λ 1666 and [CIII] λ 1907 within the observed wavelength range of 1300–2400Å. CIV is the strongest of the rest-UV lines in A1703-zd5.2, comprising a total EW of $10.5 \pm 1.0\text{Å}$. While not as extreme as the CIV emission observed in some other $z > 6$ galaxies (e.g., A1703-zd6, RXCJ2248-ID, GHZ2), CIV EWs approaching 10Å are rare locally (e.g., Y. I. Izotov et al. 2016b, 2024; P. Sencyna et al. 2017). Furthermore, we resolve the CIV emission into two narrow components ($1.1504\mu\text{m}$ and $1.1524\mu\text{m}$) that are redshifted by $+80 \text{ km s}^{-1}$ relative to systemic (Table 4). The relative fluxes of the two components (λ 1548/ λ 1550 = 2.0) and the small velocity offset (from systemic) likely indicates the resonant CIV line may face minimal attenuation. This may suggest the observed emission is close to the intrinsic value produced in the HII regions. We use the [OIII] λ 1666 ([CIII] λ 1907) detections to infer the direct gas-phase oxygen abundances (electron density) in Section 4.2 (Section 4.1) below. Here, we use the CIV/He II ratio (>5.6) to demonstrate a significant decrease in the ionizing radiation field at energies above 47 eV. Other rest-UV line ratios provide a similar picture, with the CIV/CIII (>3.2) and [OIII]/He II (>2.7) line ratios (Figure 5) suggesting a stellar origin for the ionizing radiation. It is striking how different A1703-zd5.2 is from its close ($\simeq 450 \text{ pc}$) neighbor A1703-zd5.1. While A1703-zd5.2 is in the midst of a significant episode of star formation with intense nebular emission, A1703-zd5.1 appears to have very weak emission lines, potentially following a recent downturn in star formation.

3.6. A1703-23

A1703-23 was first identified as a bright ($H=23.8$) i -band dropout (W. Zheng et al. 2009; J. Richard et al. 2009), in which subsequent follow-up reported Ly α emission at $z \simeq 5.8$ (J. Richard et al. 2009). Further spectroscopy obtained by D. P. Stark et al. (2015a) targeted the CIII] λ λ 1907, 1909 line using Keck/MOSFIRE based on the Ly α redshift; however, no strong emission was detected. The strongest rest-optical lines detected with JWST/NIRSpec are [OIII] λ 5007, H α , and H β , at wavelengths of $3.5489\mu\text{m}$, $4.6518\mu\text{m}$, and $3.4456\mu\text{m}$, respectively. Based on these strong lines, we measure a redshift of $z_{\text{spec}} = 6.0862$, slightly different from the single-line measurement presented in J. Richard et al. (2009). Unlike the other galaxies in our sample, the Balmer-line ratios (H α /H β = $3.4_{-0.4}^{+0.3}$) imply a modest dust attenuation, which is consistent with the moderately red UV slope ($\beta = -1.5$) and optical depth inferred from the SED ($\tau_V = 0.17_{-0.04}^{+0.04}$). The EWs of [OIII] ($415 \pm 22\text{Å}$), H β ($46 \pm 4\text{Å}$), and H α ($193 \pm 61\text{Å}$) are lower than typical galaxies at $z \simeq 6$ (R. Endsley et al. 2024). The

synthesized SED fit implies a moderate age stellar population (150_{-61}^{+33} Myr) and a relatively large stellar mass ($\log(M/M_{\odot}) = 9.54 \pm 0.16$). The implied SFR ($25M_{\odot} \text{ yr}^{-1}$) is broadly consistent with the star-forming main sequence at $z = 6$ (J. S. Speagle et al. 2014). This is in contrast to most of the other galaxies we targeted in Abell 1703, which sit above the main sequence with much younger stellar populations.¹⁴

The rest-frame UV spectrum reveals CIII] emission in addition to a significantly detected continuum (4.5 per resolution element). As a result, we detect several features in absorption (Figure 8). Si II $\lambda 1526$ is the most strongly detected absorption line, and traces low-ionization along with neutral gas (e.g., A. E. Shapley et al. 2003). The Si II $\lambda 1526$ absorption ($\text{EW} = -2.0 \pm 0.6 \text{ \AA}$) is moderately stronger than lines measured from stacks of typical $z \sim 3-7$ galaxies (e.g., T. Jones et al. 2012); however, the strongest absorption lines are observed in systems with the largest attenuation from dust and highest metallicity (T. Jones et al. 2012; X. Du et al. 2021). These features are qualitatively similar to the properties of A1703-23, indicating that reasonable strong absorption lines should be present in a subset of $z \simeq 6$ galaxies. The Si II $\lambda 1526$ line center is blueshifted from the systemic redshift ($\Delta v = -130 \pm 29 \text{ km s}^{-1}$), indicative of outflowing gas. In contrast, the high-ionization H β SiIV $\lambda 1393$, 1402 absorption line is detected (total $\text{EW} = 1.2 \pm 0.4 \text{ \AA}$) at the systemic redshift ($\Delta v = 4 \pm 97 \text{ km s}^{-1}$). The difference in velocity structure indicates the LIS and HIS lines are kinematically distinct. Notably, this is different than what is observed in A1703-zd1, where the two phases are kinematically more similar.

As in A1703-zd1, absorption in CIV is also detected in A1703-23. We compare this absorption profile to the same set of stellar models as described in Section 3.2 in Figure 9. Interestingly, the absorption in A1703-23 is almost absent accompanying emission near the rest wavelengths of the doublet. This is in strong contrast with the profiles typical of the spherical outflows driven by massive star winds and thus the predictions of the SSP models we compare with. This morphology is closer to that observed in broad absorption-line quasar spectra (e.g., J. T. Allen et al. 2011), though with fairly modest $\sim 2000 \text{ km s}^{-1}$ velocity for such systems. While limited by S/N, a pure absorption profile would be suggestive of interstellar gas entrained in some manner of outflow rather than stellar wind absorption; but this would stand in contrast to the near-systemic absorption in Si IV. It is also possible that the peculiar profile is a result of a relatively weak stellar wind profile combined with particularly strong interstellar absorption in CIV near-systemic. Higher-S/N and potentially higher-resolution data would help separate these contributions and enable clearer constraints to be placed on the putative stellar component directly.

3.7. A1703-zd4

A1703-zd4 is a z -band dropout identified by L. D. Bradley et al. (2012) to have a photometric redshift of $z_{\text{phot}} = 8.4_{-1.4}^{+0.9}$. Multiple spectroscopic campaigns have observed A1703-zd4 using Keck/MOSFIRE targeting the Ly α , CIV, He II, OIII], and CIII] emission lines (D. P. Stark et al. 2015a; R. Mainali

et al. 2018). These observations did not yield detections of any emission lines; however, the EW limits ($< 6-20 \text{ \AA}$ at 5σ) were sufficient to distinguish A1703-zd4 from extreme UV-line emitters such as A1703-zd6. The JWST/NIRSpec spectrum provides the first spectroscopic confirmation at a redshift of $z_{\text{spec}} = 7.8727$ based on the [OIII] $\lambda 5007$ and H β lines. For this spectroscopic redshift, the H-band magnitude ($H=25.4$) and modest magnification ($\mu = 2.0_{-0.1}^{+0.1}$) correspond to an absolute UV magnitude of $M_{\text{UV}} = -20.7$ (i.e., $\simeq L_{\text{UV}}^*$; R. J. Bouwens et al. 2021). At the stellar mass ($\log(M/M_{\odot}) = 8.50 \pm 0.27$) and SFR ($\log(\text{SFR}/M_{\odot} \text{ yr}^{-1}) = 1.06_{-0.45}^{+0.52}$) inferred from the SED fit, we find that A1703-zd4 is elevated above the star-forming main sequence by 0.4 dex (J. S. Speagle et al. 2014). The best-fit SED implies a nonzero impact from dust attenuation ($\tau_V = 0.07_{-0.04}^{+0.04}$), which is consistent with the UV slope measured using NIRSpec ($\beta = -2.0$) and relative fluxes of the strongest observed Balmer lines ($H\gamma/H\beta = 0.39_{-0.10}^{+0.09}$; Table 3).

We measure large [OIII] $\lambda 5007$ and H β EWs of $1317 \pm 432 \text{ \AA}$ and $148 \pm 46 \text{ \AA}$, respectively, which are both consistent with the high sSFR of the SED. A1703-zd4 is one of the two objects in our sample with an [OII] detection enabling the O32 ratio to be calculated. As the best-fit SED and Balmer-line ratios imply the presence of dust, we correct the [OIII] and [OII] fluxes for attenuation using the J. A. Cardelli et al. (1989) attenuation curve and assuming an intrinsic $H\gamma/H\beta = 0.47$. We derive a resulting O32 ratio of $4.0_{-0.9}^{+0.9}$, while we calculate a line ratio prior to the dust correction of $5.6_{-0.7}^{+0.5}$. Star-forming galaxies in this epoch commonly have O32 in excess of the A1703-zd4 value (O32 $\simeq 10$; M. Tang et al. 2023; R. L. Sanders et al. 2023; A. J. Cameron et al. 2023b), with a clear trend between [OIII] EW and O32 (M. Tang et al. 2023). A1703-zd4 appears broadly consistent with this relation.

In the rest-frame UV, we detect clear Ly α emission as well as [CIII] $\lambda 1907$ at $S/N > 3$. The [CIII] $\lambda 1907$ EW is just $3.6 \pm 0.7 \text{ \AA}$, which is easily matched by EELGs at $z \sim 2$ with comparable optical line properties (e.g., M. Tang et al. 2019). While no other rest-UV metal line is detected (EWs $< 3-6 \text{ \AA}$), we compute limits on the CIV/CIII] (< 0.3) and CIII]/He II (> 4.8) line ratios. Both of these constraints support a population of massive stars as the source of ionizing radiation in A1703-zd4 (Figure 5). We also detect a weak Ly α line with an EW of $3.4 \pm 0.9 \text{ \AA}$. We calculate a velocity offset of $+240 \text{ km s}^{-1}$ for Ly α relative to the systemic redshift set by the optical lines. The Ly α EW in A1703-zd4 is relatively small, and the typical EWs of galaxies at lower redshift with the same optical line EWs suggest a significant attenuation of Ly α photons from A1703-zd4. We compute the Ly α escape fraction following the same method outlined in Section 3.1, and recover a value of just $f_{\text{esc}}^{\text{Ly}\alpha} = 0.03 \pm 0.01$, indeed suggesting the observed line is a small portion of the intrinsic emission.

4. Sample Properties in Abell 1703

In the previous Section, we presented the spectroscopic properties of our $z \gtrsim 6$ sample in the Abell 1703 field, describing each source individually. Here we describe the electron densities (Section 4.1), gas-phase oxygen abundances (Section 4.2), and carbon and nitrogen abundances (Sections 4.3 and 4.4). Finally, we discuss existing constraints on aluminum enhancements, with the goal of identifying an additional anomalous abundance pattern in globular clusters

¹⁴ Given the weak lines, we also fit the synthesized photometry with SED models assuming a TcSFH (see Section 3.4), which yielded a consistent stellar mass, [OIII] + H β EW, and minimum χ^2 to that of the best-fit CSFH model. This suggests that additional flexibility in the SFH is not required to describe A1703-23, and a CSFH is an appropriate assumption given current constraints.

(Section 4.5). In all subsections below, our broad goal is using the new data to improve our understanding of the properties of galaxies with hard ionizing sources and nitrogen-enhanced ionized gas.

4.1. High Electron Densities in Ionized Gas

Recent work has revealed ionized gas with extremely high electron densities ($n_e \simeq 10^5 \text{ cm}^{-3}$) in a subset of reionization era galaxies, several orders of magnitude larger than typical densities at lower redshifts (A. J. Bunker et al. 2023; P. Senchyna et al. 2024; M. W. Topping et al. 2024a). This was first inferred for GNz11 based on the NIV] doublet ratio (A. J. Bunker et al. 2023; R. Maiolino et al. 2024a; P. Senchyna et al. 2024) and was then demonstrated in RXCJ2248-ID based on three density-sensitive doublets in the UV (M. W. Topping et al. 2024a). In GNz11, it has been suggested the densities may be related to the broad-line region of an AGN (R. Maiolino et al. 2024a), but in RXCJ2248-ID, the high ionized gas densities appear likely related to dense conditions during a strong burst of star formation (M. W. Topping et al. 2024a).

A1703-zd6 has a similar spectrum as RXCJ2248-ID, with strong CIV emission and extremely powerful rest-optical emission lines ([OIII]+H β EW = 4116 Å), suggesting a very young stellar population (1.6 Myr). We detect two density-sensitive doublets in the NIRSPEC observations presented in Section 3.1 We infer densities using the GETTEM DEN procedure from the PYNEB software package (V. Luridiana et al. 2015). The NIV] doublet ratio ($f^{1483}/f^{1486} = 0.47_{-0.21}^{+0.19}$) suggests the ionized gas is very dense ($19_{-9}^{+20} \times 10^4 / \text{cm}^3$), comparable to that seen in RXCJ2248-ID. The CIII] doublet ratio ($f^{1907}/f^{1909} = 0.49_{-0.16}^{+0.19}$) reveals a similar picture ($9.4 \pm 4.2 \times 10^4 \text{ cm}^{-3}$). Given the higher ionization potential of NIV] (47.4 eV), its emission originates nearer to the ionizing source when compared to the CIII] emission (24.4 eV). The electron density follows a similar trend and increases toward the inner regions of the H II regions, leading higher-ionization probes to yield higher densities (e.g., R. C. J. Kennicutt 1984; L. J. Kewley et al. 2019; D. A. Berg et al. 2021).

There are several potential physical explanations for the elevated densities. We may expect high ionized gas densities ($\simeq 10^5 \text{ cm}^{-3}$) to arise in a short window after a strong burst of star formation, when gas surface densities are sufficiently high to create an over-pressurized environment for the HII regions (e.g., M. D. Lehnert et al. 2009). In this picture, we would only observe very dense gas in the subset of galaxies with the largest sSFRs (and hence the largest optical line EWs). On the other hand, the UV-based tracers of electron densities (CIII], NIV]) have long been known to probe denser gas than the more typically used doublets in the optical ([OII], [SII]; B. L. James et al. 2014, 2018; R. Mainali et al. 2023). It is thus possible that the UV lines may reveal elevated densities similar to RXCJ2248-ID and A1703-zd6 in all reionization era galaxies, not just those undergoing strong bursts.

We can attempt to distinguish between these two scenarios using our Abell 1703 sample. In addition to A1703-zd6, we detect the density-sensitive CIII] doublet in A1703-zd2 and zd5.2, both with lower H β EWs than A1703-zd6. The spectra of the three galaxies reveal distinctly different doublet flux ratios and hence different densities (Figure 10). A1703-zd5.2 has the lowest H β EW (170 Å) and has a 1907/1909 flux ratio (>1.48), implying moderately low ionized gas densities ($<1500 \text{ cm}^{-3}$). A1703-zd2 has a larger H β EW (209 Å) and

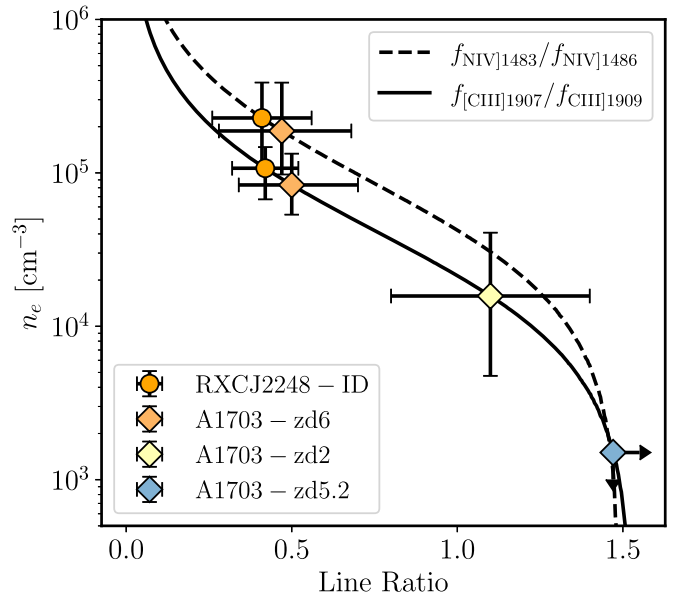


Figure 10. Electron densities inferred from the CIII] and NIV] doublet ratios. Theoretical CIII] and NIV] line ratios calculated for different densities and assuming $T_e = 20000\text{K}$ are displayed as the solid and dashed lines, respectively. Measured line ratios and inferred densities for the high-redshift galaxies are shown as colored markers. Densities inferred from the CIII] doublet are placed along the solid line, while densities inferred from NIV] are plotted on the dashed line. A1703-zd2 and A1703-zd5.2 are only detected using the CIII] line, while A1703-zd6 and RXCJ2248-ID are detected in CIII] and NIV].

a 1907/1909 flux ratio ($1.10_{-0.22}^{+0.21}$) indicating moderately large densities ($2 \times 10^4 \text{ cm}^{-3}$). Taking these results together with the spectra of A1703-zd6 and RXCJ2248-ID, we find that the UV-based densities do increase with H β EW (albeit in small samples), as would be expected if densities are elevated in the strongest bursts. The highest densities ($> 10^5 \text{ cm}^{-3}$) appear limited to a subset of galaxies with H β EWs in excess of 300 Å, corresponding to extremely young stellar populations ($\lesssim 2$ Myr) formed in a recent upturn of star formation.

Signatures of very high densities are not limited to the rest-UV. In galaxies with ionized densities of 10^5 cm^{-3} , we expect the [OII] emission line to be collisionally de-excited, leading to high O32 indices (184 and > 36 in RXCJ2248-ID and A1703-zd6, respectively). We also expect to see strong He I $\lambda 5876$ emission owing to enhanced collisional excitation of this transition (see, e.g., H. Yanagisawa et al. 2024). In RXCJ2248-ID, He I $\lambda 5876$ was found to be 21% as strong as H β , roughly $2 \times$ larger than is typically found in local star-forming galaxies (K. N. Abazajian et al. 2009). The enhancement in the line ratio can be fully explained by the elevated gas densities (see M. W. Topping et al. 2024a). We find similarly enhanced He I $\lambda 5876$ emission in A1703-zd6, with a line flux that is 26% that of H β . The other galaxies in our sample are not detected in He I $\lambda 5876$, as expected given the lower ionized gas densities. The upper limits we are able to place on the He I $\lambda 5876$ /H β flux ratios in these systems ($\lesssim 0.10$ - 0.15) are typically $2 \times$ lower than that found in A1703-zd6 and RXCJ2248-ID (Figure 11), consistent with flux ratios found in nearby galaxies. These results suggest that deep rest-optical spectroscopy may be able to identify high-density sources via elevated He I $\lambda 5876$ emission (see also H. Yanagisawa et al. 2024).

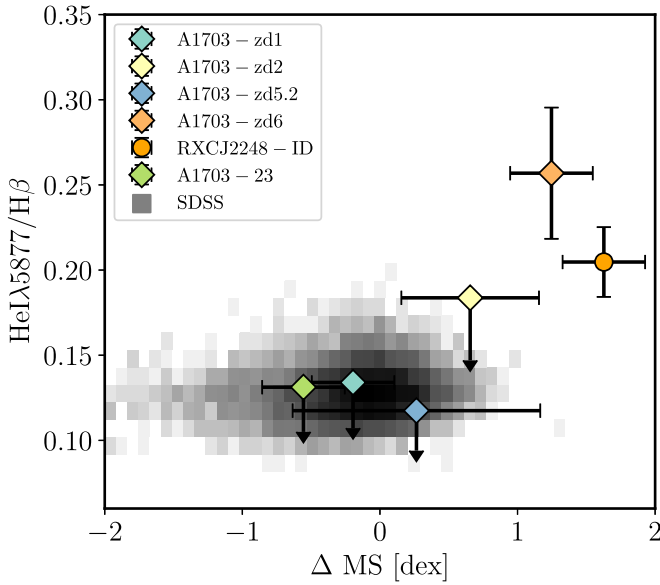


Figure 11. Relative $\text{He I } \lambda 5877 / \text{H}\beta$ flux as a function of distance from the star-forming main sequence. Galaxies at $z > 6$ are displayed as colored symbols, while the locus traced by Sloan Digital Sky Survey galaxies is shown as the gray histogram. Typical galaxies in the local Universe have an average $\text{He I} / \text{H}\beta$ line flux of 0.12, regardless of their location in the SFR versus M_* plane. While the objects in our sample within 1 dex of the main sequence are consistent with this line ratio, A1703-zd6 and RXCJ2248-ID are significantly He I enhanced, resulting from the high densities preferentially boosting He I relative to $\text{H}\beta$ from collisional effects.

4.2. Gas-phase Oxygen Abundances

One of the primary explanations of nebular CIV emission at $z \gtrsim 6$ is hard radiation from a population of very metal-poor massive stars. In this case, we would expect the CIV emitting galaxies to be linked to metal-poor gas, as is often found in nearby galaxies (P. Senchyna et al. 2017, 2022; A. Wofford et al. 2021; D. Schaerer et al. 2022). Photoionization modeling in D. P. Stark et al. (2015a) suggested that reproducing the strong CIV emission in A1703-zd6 may require metallicities approaching 2% of the solar value ($12 + \log(\text{O}/\text{H}) = 7.05$), but these inferences were based on very limited information available from ground-based observations. With the NIRSpect observations presented in this paper, we can now derive a direct gas-phase metallicity for A1703-zd6, while also investigating implications for the metal content in the other lensed systems in our sample.

We quantify gas-phase oxygen abundances for each object in our sample using the available emission-line constraints. The $11\sigma[\text{OIII}]\lambda 4363$ detection in A1703-zd6 provides the best O/H constraint in our sample, while A1703-zd5.2 and A1703-23 are detected in the auroral $[\text{OIII}]\lambda 1666$ line. For these systems, we derive direct metallicities following the methods described in M. W. Topping et al. (2024a; see also Y. I. Izotov et al. 2006). For the remaining galaxies in our sample, we infer the oxygen abundance using the O3 and O32 strong-line calibrations derived from high-redshift galaxies (R. L. Sanders et al. 2024). Results are listed in Table 3. Gas-phase oxygen abundances are generally found to be low, ranging from $12 + \log(\text{O}/\text{H}) = 7.20$ to 7.98.

We start with our primary target, the strong CIV emitting galaxy A1703-zd6. Adopting the density found in Section 4.1, we recover an electron temperature of $T_e(\text{O}^{++}) = 23000 \pm 3200\text{K}$, which is consistent with low-metallicity

galaxies in this epoch (e.g., H. Katz et al. 2023; I. H. Laseter et al. 2024). For this electron temperature and the $[\text{OIII}]\lambda 5007$ and $\text{H}\beta$ fluxes, we derive an oxygen abundance of $12 + \log(\text{O}/\text{H}) = 7.47 \pm 0.19$. This value represents oxygen only in the doubly ionized state, which we expect to dominate the abundance in this system given the very large O32 ratio (> 36). While collisional de-excitations from the high densities may contribute to the weak $[\text{OII}]$, the ionization conditions implied by the additional optical line ratios (e.g., O3) and strong rest-UV lines suggest that a majority of the oxygen has been excited beyond the singly ionized state. We derive a consistent metallicity when considering the O3 ratio ($6.4^{+0.3}_{-0.4}$), which yields an abundance of $12 + \log(\text{O}/\text{H}) = 7.60 \pm 0.30$ using the R. L. Sanders et al. (2024) calibrations. Calibrations using the O32 and Ne3O2 ratios indicate much lower metallicities; however, these line ratios are likely severely impacted by the density of the system (see Section 4.1). Overall, these results suggest the gas in A1703-zd6 is metal-poor ($6\%Z_\odot$), consistent with lower-redshift results (e.g., P. Senchyna et al. 2017, 2022; A. Wofford et al. 2021; D. Schaerer et al. 2022) and as would be expected if there is a low-metallicity stellar population contributing to the hard radiation field. However, what stands out most about A1703-zd6 in our sample is not its metallicity, but rather its very young inferred stellar population age ($1.6^{+0.5}_{-0.4}$ Myr) and correspondingly large $\text{H}\beta$ EW ($424 \pm 112 \text{\AA}$). Both are at the extremes of what has been seen by JWST in the $z \gtrsim 6-8$ galaxy population. Presumably, the coupling of the extremely young stellar population and low gas phase metallicity are mutually required for strong CIV emission (e.g., P. Senchyna et al. 2019).

We have also detected strong CIV emission ($> 10\text{\AA}$) in two additional galaxies in the Abell 1703 field (A1703-zd2 and A1703-zd5.2). As expected, the new CIV emitters are among the most metal-poor in the sample. The O3 ratios of these two systems ($5.2^{+0.5}_{-0.7}$ and $4.4^{+0.3}_{-0.4}$) are well below average (O3=7–10) at $z \simeq 6-8$ (e.g., M. Tang et al. 2023; R. L. Sanders et al. 2023; A. J. Cameron et al. 2023b). Using the calibrations described above, these likely point to low metallicities: $12 + \log(\text{O}/\text{H}) = 7.35 \pm 0.30$ (A1703-zd2) and 7.26 ± 0.28 (A1703-zd5.2). We additionally detect the $[\text{OIII}]$ UV-based auroral line in A1703-zd5.2, suggesting a direct method metallicity ($12 + \log(\text{O}/\text{H}) = 7.20 \pm 0.28$) consistent with the O3-based value described above. This direct metallicity only reflects the doubly ionized oxygen abundance, as the emission lines sensitive to the singly ionized abundance are not covered by our spectrum. The inferred stellar populations ages of A1703-zd2 (17 Myr) and A1703-zd5.2 (23 Myr) are the next two youngest in our sample after A1703-zd6.

We note that galaxies in Abell 1703 with metal-poor gas but without young stellar populations do not show strong CIV emission. A1703-zd5.1 provides the best example of such a source, with ionized gas that appears metal poor ($12 + \log(\text{O}/\text{H}) = 7.19 \pm 0.43$) but has comparatively weak CIV emission ($< 4.3 \text{\AA}$). As pointed out in Section 3.5, this source appears best fit by a recent downturn in star formation (or ionizing photon leakage), resulting in a spectrum without strong CIV emission in spite of the low metallicity. In contrast, A1703-zd4 has a relatively young stellar population age (23 Myr) but gas-phase metallicity at the upper end of our sample ($12 + \log(\text{O}/\text{H}) = 7.98 \pm 0.31$). Here we see no

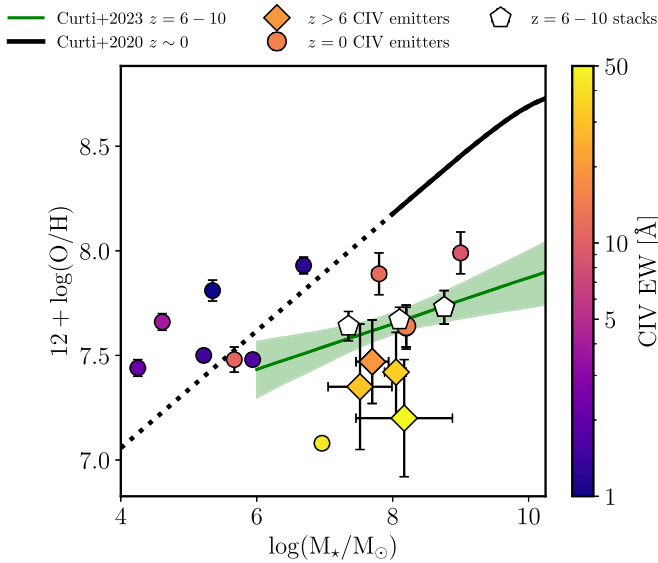


Figure 12. Inferred oxygen abundance as a function of stellar mass for CIV emitters at $z > 6$ (diamonds) from the A1703 field in addition to RXCJ2248-ID (M. W. Topping et al. 2024a), compared to local CIV emitters (squares; Y. I. Izotov et al. 2016a, 2016b, 2018a, 2018b; P. Senchyna et al. 2017, 2022; A. Wofford et al. 2021; D. Schaerer et al. 2022). Objects are color-coded based on their CIV EWs as indicated by the color bar on the right. We display the mass–metallicity relation derived locally (black line; M. Curti et al. 2020). The dotted black line represents an extrapolation of the local MZR from M. Curti et al. (2020) below the mass range probed by their sample. The green line and white pentagons are the best-fit MZR and composite measurements of $z \sim 6-10$ galaxies from M. Curti et al. (2023). The local systems scatter about the MZR, with the smallest and largest CIV emitters lying above and below the MZR, respectively. All of the $z > 6$ CIV emitters have below-average metallicities for their stellar mass.

strong CIV emission ($< 4.9 \text{ \AA}$). Collectively, these results emphasize that the presence of strong CIV emission is limited to sources that show both young stellar populations ($\lesssim 25 \text{ Myr}$) and low-metallicity gas ($\lesssim 0.1 Z_{\odot}$), consistent with trends seen at lower redshift (e.g., P. Senchyna et al. 2017, 2022; A. Wofford et al. 2021; D. Schaerer et al. 2022). We will come back to discuss the demographics of the CIV population through investigating the full public spectroscopic database in Section 5.

To place the $z \gtrsim 6$ CIV-emitting galaxies in context, we consider their position with respect to the mass–metallicity relationship (MZR; M. Curti et al. 2023), as derived from JWST spectroscopy of $z \simeq 6-10$ galaxies (Figure 12). We also include several additional strong $z \gtrsim 6$ CIV emitters (M. W. Topping et al. 2024a) as well the local star-forming galaxies with CIV detections (Y. I. Izotov et al. 2016a, 2016b, 2018a, 2018b; P. Senchyna et al. 2017, 2022; A. Wofford et al. 2021; D. Schaerer et al. 2022). It is clear in Figure 12 that the galaxies with strong CIV emission at $z \gtrsim 6$ typically fall below the MZR, implying that they are both younger and more metal poor than the parent sample of early galaxies. The low-redshift galaxies tend to have much weaker CIV EWs ($\simeq 1-3 \text{ \AA}$; see Y. I. Izotov et al. 2024) and lower stellar masses ($\lesssim 10^6 M_{\odot}$) than existing detections at $z \gtrsim 6$. The mismatch in the mass of the CIV emitters at low and high redshift arises because the low metallicities required to power hard radiation fields ($\lesssim 0.1 Z_{\odot}$) are possible in moderately massive galaxies in the reionization era ($\simeq 10^8 M_{\odot}$). In the local Universe, these low metallicities are only found in much lower-mass galaxies. As a result, there is potentially a significant difference between the $z \gtrsim 6$ CIV

emitters and the local reference sample. Future work is required to investigate whether these differences lead to distinctly different spectra at fixed metallicity.

4.3. C/O Abundances

The abundance of carbon (relative to oxygen) encodes insights into the past SFH (R. B. C. Henry et al. 2000; C. Esteban et al. 2014; D. A. Berg et al. 2016, 2019) and integrated yields of earlier generations of stars (e.g., D. R. Garnett et al. 1995; J. Yin et al. 2011; D. A. Berg et al. 2019). Early JWST spectra have constrained carbon-to-oxygen (C/O) ratios in a small number of early galaxies with deep UV constraints on emission from carbon and oxygen lines (K. Z. Arellano-Córdova et al. 2022a; T. Jones et al. 2023; F. D’Eugenio et al. 2024; M. W. Topping et al. 2024a). The detections (and upper limits) of the UV carbon and oxygen lines in our sample allow us to build on these studies. Here, we focus on galaxies in the Abell 1703 field with detections in CIV, CIII], and OIII] (A1703-zd6 and A1703-zd5.2), which will provide the most robust constraints on C/O.

Briefly, we infer the C/O abundance ratio by first computing C^{++}/O^{++} from the observed CIII] and OIII] emission lines using PYNEB (V. Luridiana et al. 2015). In calculating this abundance ratio, we assume an electron temperature and density inferred from OIII] $\lambda 1666$ /[OIII] $\lambda 5007$ and the CIII] doublet, respectively (see Table 3). The CIII] doublet in A1703-zd5.2 is in the low-density regime, providing only an upper limit on the electron density. For this object, we assume a density of 1000 cm^{-3} , which is consistent with typical densities observed in this epoch (e.g., H. Katz et al. 2023; I. H. Laseter et al. 2024; R. L. Sanders et al. 2024). We note that the inferred abundance ratios vary minimally if a different assumption on density is imposed. These emission lines yield $\log(C^{++}/O^{++})$ abundance ratios of -1.20 ± 0.12 and -1.13 ± 0.15 for A1703-zd6 and A1703-zd5.2, respectively.

Both systems show strong CIV emission ($19.4 \pm 1.4 \text{ \AA}$ in A1703-zd6 and $10.5 \pm 1.0 \text{ \AA}$ in A1703-zd5.2), implying a significant amount of the carbon budget exists in the triply ionized state. The CIV emission is subject to resonant scattering, and the observed line fluxes may underestimate the true values. As discussed in Section 3, the line profiles of both galaxies give indications of modest scattering. Here we consider two bounding cases. On one hand, we compute ionic ratios assuming the observed CIV EWs are the intrinsic values. For the other limiting case, we assume that 50% of the CIV flux has been scattered out of the line of sight, providing a conservative bound on the fraction of carbon in the triply ionized state. We obtain C^{3+}/C^{++} ionization fractions using PYNEB by computing the C^{3+} and C^{++} emissivities at the densities and temperatures defined above. Using the observed CIV emission as intrinsic, we obtain lower-bound values of C^{3+}/C^{++} of 0.08 ± 0.07 (A1703-zd6) and 0.06 ± 0.08 (A1703-zd5.2) and upper-bound values of 0.38 ± 0.12 (A1703-zd6) and 0.36 ± 0.14 (A1703-zd5.2). These give the likely range of ionization fractions. To select a value within this range to use for our calculations, we consider an approach used in G. C. Jones et al. (2024). Given that the redder component of the CIV doublet is less susceptible to attenuation (and that both profiles appear to show only modest signs of scattering), we can adopt its flux as intrinsic and compute the total CIV flux using the theoretical doublet ratio ($\lambda 1548/\lambda 1550=2$). This suggests C^{3+}/C^{++} values of 0.27 ± 0.08 (A1703-zd6) and

0.13 ± 0.11 (A1703-zd5.2), between the two boundary cases quoted above. We will use these values in our calculations below.

Using the ionic abundances computed above, we derive a total abundance ratio of $\log(C/O) = -0.74 \pm 0.18$ and $\log(C/O) = -0.79 \pm 0.17$ for A1703-zd6 and A1703-zd5.2, respectively. Both suggest ionized gas that is not substantially enriched in carbon relative to oxygen, well below ($\approx 4 \times$) the solar value ($\log(C/O)_{\odot} = -0.23$; M. Asplund et al. 2009). Similarly low C/O ratios are commonly inferred for metal-poor galaxies locally (D. A. Berg et al. 2016; D. A. Berg et al. 2018; D. A. Berg et al. 2020; S. Ravindranath et al. 2020; see, R. J. Dufour et al. 1988) and at $z \approx 2$ (D. K. Erb et al. 2010; L. Christensen et al. 2012; D. P. Stark et al. 2014; D. A. Berg et al. 2019). Similarly, many systems in the reionization era have significantly subsolar C/O (e.g., T. Jones et al. 2023; K. Z. Arellano-Córdova et al. 2022a; M. Stiavelli et al. 2023; W. Hu et al. 2024), consistent with our results in this paper. The low C/O observed in these systems is consistent with enrichment from supernovae, without significant pollution from asymptotic giant branch stars (e.g., J. Yin et al. 2011; D. A. Berg et al. 2019). The absence of such evolved stellar populations is consistent with the young ages and massive stars implied by the rest-UV and optical spectra described in Section 3. We note that C/O ratios approaching the solar value are also expected at extremely low metallicities, possibly reflecting yields from Population III stars (e.g., C. J. Akerman et al. 2004; L. Carigi & M. Peimbert 2011). We find no evidence of these in the JWST spectra analyzed above.

4.4. N/O Abundances

In M. W. Topping et al. (2024a), we demonstrated that the strong CIV emitting galaxy RXCJ2248-ID has an anomalously large N/O ratio, similar to that reported by A. J. Bunker et al. 2023 in GNz11 (see also Y. Isobe et al. 2023; R. Marques-Chaves et al. 2024; R. Navarro-Carrera et al. 2024). We detect similar nitrogen line emission (NIV] and [NIII]) in the CIV emitting galaxy A1703-zd6 presented in this paper. We have shown that this galaxy has metal-poor gas ($12 + \log(O/H) = 7.47 \pm 0.19$) and a subsolar C/O ratio ($\log(C/O) = -0.74$). Here we first constrain the N/O ratio in A1703-zd6, before commenting briefly on the relative nitrogen abundances in the other systems in our sample. As we also detect CIV in two additional galaxies, our measurements allow us to further explore the potential link between galaxies with hard radiation fields and significant nitrogen enhancements.

Our methodology is similar to that discussed in detail in M. W. Topping et al. (2024a; and largely parallels our derivation of C/O described above). We will expand on our abundance calculations in Plat et al. (2025, in preparation). We infer N/O in A1703-zd6 and place limits on N/O for systems with [OIII] detections and nitrogen line nondetections (A1703-zd5.2, A1703-23) using the $\frac{NIV] + NIII]}{OIII]}$ line ratio (see, e.g., A. J. Cameron et al. 2023b; P. Senchyna et al. 2024). Briefly, in deriving the N/O abundances, we assume the electron temperature inferred using the highest-S/N auroral emission line ([OIII] $\lambda 4363$ or [OIII] $\lambda 1666$). For A1703-zd6 and A1703-zd5.2, we fix the electron density to the value inferred from the NIV] and CIII] doublets, respectively. Lacking a density-sensitive measurement in A1703-23, we assume a value of 1000 cm^{-3} in our abundance calculations, motivated by typical densities in similar sources at these redshifts (e.g., H. Katz et al. 2023; I. H. Laseter et al. 2024

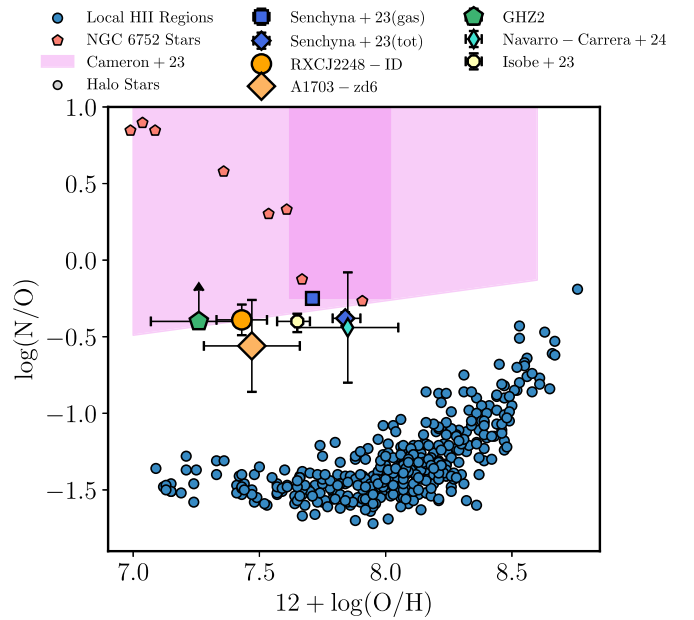


Figure 13. N/O as a function of O/H for stars and HII regions in the local Universe and galaxies at high redshift. Local HII regions trace out a tight locus that asymptotically approaches $\log(N/O) \approx -1.4$ at low metallicities. We display measurements from a sample of N-enriched high-redshift galaxies including A1703-zd6 (orange diamond) with nitrogen abundances $10 \times$ higher than HII regions at fixed O/H. This parameter space is shared by individual stars in the globular cluster NGC 6752, indicating that both types of objects may undergo common formation processes.

R. L. Sanders et al. 2024). We stress that adopting different densities does not have a large systematic effect on our abundance estimates.

We find that the NIV], NIII], and OIII] line fluxes in A1703-zd6 imply a supersolar nitrogen abundance, with a relative abundance of $\log(N/O) = -0.6 \pm 0.3$. Figure 13 demonstrates that this is moderately higher than the solar value ($\log(N/O)_{\odot} = -0.86$; M. Asplund et al. 2009) and nearly $10 \times$ higher than typical values seen in HII regions at the metallicity of A1703-zd6. For A1703-zd5.2 and A1703-23, we follow the methodology described above using the 3σ upper limits on NIV] and NIII] and find constraints of $\log(N/O) < -0.9$ and $\log(N/O) < -0.8$, respectively. While we cannot rule out the possibility that these two systems have a minor nitrogen enhancement relative to the local HII regions, their N/O constraints are consistent with the local locus.

These measurements offer new insight into the nature of the nitrogen-emitting galaxies that have been found in the reionization era with JWST. Our Cycle 1 program has now confirmed nitrogen-enhanced gas in both of our primary targets (A1703-zd6 and RXCJ2248-ID), each originally selected only on strong CIV emission in ground-based UV spectroscopy. This potentially hints at a connection between the processes leading to the formation of hard ionizing sources and those leading to the overabundance of nitrogen. We have shown that both galaxies are likely in the midst of strong bursts of star formation with spectra dominated by the light from very young stellar populations ($\lesssim 2$ Myr). This results in rest-optical emission lines that are among the most prominent (upper 1% of [OIII]+H β EW) seen in existing samples of reionization era galaxies (e.g., J. Matthee et al. 2023; R. Endsley et al. 2024). Both galaxies also appear to host compact star clusters with very dense star formation conditions, the latter revealed by very

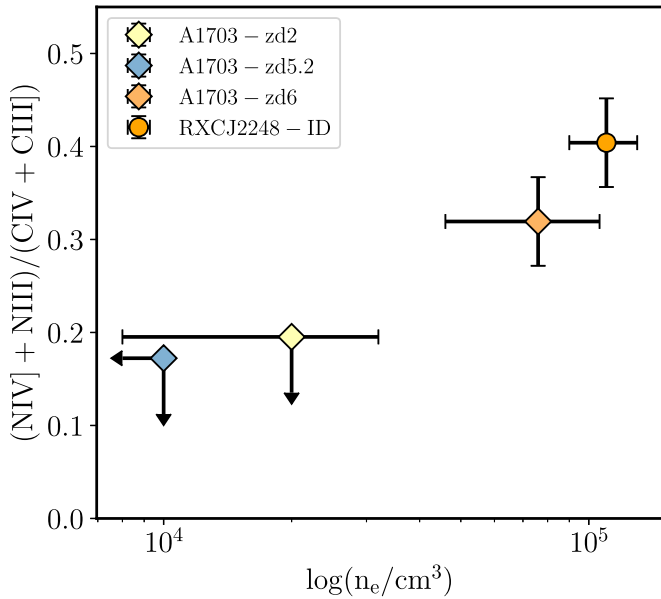


Figure 14. Total NIV]+NIII flux compared to the total CIV+CIII flux as a function of electron density. We display all objects from our sample for which the density can be constrained from the CIII] ratio. The two galaxies with nitrogen line detections (and thus higher N/C line ratios) have the highest densities, while the galaxies with more typical CIII] electron densities have (NIV]+NIII)/(CIV+CIII) ratios that are < 0.2 .

high electron densities ($\approx 10^5 \text{ cm}^{-3}$) associated with the density-sensitive emission line doublets in the UV. These high densities might correspond to a short period ($\approx 1-3 \text{ Myr}$) after strong bursts where HII regions remain confined by very high gas densities that led to the strong burst. At later evolutionary stages, a variety of feedback processes will disperse the birth cloud gas, and the HII regions will acquire more typically observed densities ($\approx 10^2-3 \text{ cm}^{-3}$).

In this picture, the observed link between nitrogen enrichment and hard ionizing sources (the latter responsible for CIV or He II emission) may have its origin in the extremely dense conditions that arise in a brief window ($\lesssim 1-3 \text{ Myr}$) following strong bursts in the reionization era. The high stellar densities ($> 3.6 \times 10^4 M_{\odot}/\text{pc}^2$ in RXCJ2248-ID; M. W. Topping et al. 2024a) that arise in the clusters formed during these bursts will enhance dynamical interactions (i.e., runaway collisions, binary mass transfer) that may lead to the formation of very massive stars and hot stripped stars, boosting the population of hard ionizing sources relative to less dense environments. Such dynamical processes may also help explain how the ISM is polluted with its overabundance of nitrogen relative to oxygen (e.g., M. Gieles et al. 2018; F. Martins et al. 2020; C. Charbonnel et al. 2023).

Our observations also unveiled two new CIV emitting galaxies (A1703-zd5.2, A1703-zd2), with CIV EWs similar to A1703-zd6. According to the picture described above, we may expect to show both nitrogen lines, but our observations reveal no NIII] or NIV] emission in either galaxy. In Figure 14, we plot the upper limit on the flux ratio of nitrogen (NIV] and NIII) and carbon lines (CIII] and CIV) for A1703-zd5.2 (< 0.17) and A1703-zd2 (< 0.19). The flux limits confirm that these two CIV emitters are significantly weaker nitrogen line emitters than RXCJ2248-ID and A1703-zd6, where this ratio was found to be $1.5-2.0 \times$ greater. Clearly, the nitrogen line emission is not present in all strong CIV emitters. While both

A1703-zd5.2 and A1703-zd2 are dominated by relatively young stellar populations (23_{-17}^{+45} and $17_{-7}^{+18} \text{ Myr}$, respectively), they are not as young as A1703-zd6 ($1.6_{-0.4}^{+0.5} \text{ Myr}$) or RXCJ2248-ID ($1.8_{-0.4}^{+0.7} \text{ Myr}$). Similarly, the ionized gas densities appear elevated ($\approx 1-2 \times 10^4 \text{ cm}^{-3}$) but are $5-10 \times$ lower than the densities in A1703-zd6 and RXCJ2248-ID. It is plausible that these new systems correspond to a slightly later evolutionary state, or that they simply experienced less intense bursts where densities were not elevated sufficiently to initiate the conditions required for seeding the ISM with the nitrogen enhancement. Larger samples will be required to confirm this picture in greater detail. We will come back to this in Section 5, investigating the nitrogen line emission in a large public spectroscopic sample.

4.5. Signatures of Additional Abundance Anomalies

The $z \gtrsim 6$ nitrogen line emitters may provide our first opportunity to directly study the nature of the polluters responsible for the anomalous abundances in globular clusters (see, e.g., N. Bastian & C. Lardo 2018, for a recent review). If the N/O and N/C ratios are truly related to those found in globular clusters, we should also see evidence of the additional abundance anomalies associated with hydrogen burning. R. Marques-Chaves et al. (2024) have suggested that aluminum enhancements (from the MgAl cycle) are likely to be the most readily detectable in early galaxies. The most accessible probes of aluminum in these galaxies are the AIII λ 1670 and AIII λ 1854, 1862 lines. These features are most commonly observed in absorption in high-redshift star-forming galaxies (e.g., C. C. Steidel et al. 2016), but are occasionally seen in emission toward some AGNs (R. Alexandroff et al. 2013). If aluminum is overabundant in the ISM of the nitrogen line emitters, we may expect to see the Al III lines in emission.

In RXCJ2248-ID, we presented an upper limit on the strength of the AIII λ 1854, 1862 doublet, with each individual component likely having an EW below 2.0 \AA . Here we extend this analysis to A1703-zd6. We search for Al III emission near the expected observed wavelengths of the doublet. The spectrum of A1703-zd6 displays an emission feature at the expected wavelengths of the AIII λ 1862 emission line. We closely inspect the spectrum surrounding this feature and find that one exposure suffers from a large residual resulting from the subtraction from a snowball event (see Section 2). To remedy this, we repeat our data reduction procedures while removing the affected exposures. The resulting spectrum still exhibits an emission feature (EW = 2.7 \AA) at the expected wavelength of the AIII λ 1854 line. As the S/N is low (2.6), we consider this feature to be tentative. We do not detect any emission at the location of the AIII λ 1862 line, consistent with expectations given the predicted flux ratio ($\lambda 1854/\lambda 1862=1.5$) of the doublet.

To quantify the Al abundance implied by this tentative feature in A1703-zd6, we consider the AIII λ 1854/OIII] λ 1666 line ratio, for which we measure $f_{\text{AIII}}/f_{\text{OIII}} = 0.36$. For the metallicity and ionization parameter that we infer for A1703-zd6, the observed $f_{\text{AIII}}/f_{\text{OIII}}$ indicates an aluminum enhancement that is $30-100 \times$ the solar value ($\log(\text{Al}/\text{O})_{\odot} = -2.24$; M. Asplund et al. 2009). A more detailed treatment of the abundance ratios will be presented by Plat et al. (2025, in preparation). However, we note that this level of aluminum enhancement is consistent with the abundance pattern seen in a subset of individual globular cluster stars (e.g., E. Carretta et al. 2018; M. Carlos et al. 2023). Deeper

spectroscopy of A1703-zd6 will ultimately be required to verify this tentative feature.

5. Demographics of $z > 4$ UV Line Emitters

The discovery of enhanced N/O and N/C ratios in early galaxies has been one of the more surprising early findings of JWST (A. J. Bunker et al. 2023; Y. Isobe et al. 2023; R. Marques-Chaves et al. 2024; M. W. Topping et al. 2024a; M. Castellano et al. 2024), potentially providing a signpost of globular clusters in formation (C. Charbonnel et al. 2023; J. S. Vink 2023; P. Senchyna et al. 2024). In this paper, we have presented more evidence suggesting that the nitrogen emitters also tend to have a population of hard ionizing sources and very dense ionized gas (see Section 4.3 and M. W. Topping et al. 2024a).

In this Section, we attempt to place the strong nitrogen and carbon line emitters in a broader context, establishing how common these systems are at very high redshift and comparing their basic properties to that of the full galaxy population. To achieve this goal in a self-consistent manner, we assemble a large spectroscopic sample of $z \gtrsim 4$ galaxies with NIRSpec observations and characterize the incidence of strong UV line emission. While the nitrogen emitters observed as part of this program (i.e., A1703-zd6 and RXCJ2248-ID) were observed due to their strong CIV emission, this large spectroscopic sample was not constructed with the same prerequisite. The data reduction and construction of the NIRSpec spectroscopic catalog are briefly described in Section 5.1. We then discuss the statistics and properties of the CIV-emitters in Section 5.2 and that of the nitrogen emitters in Section 5.3.

5.1. Public JWST/NIRSpec Spectra at $z > 4$

We assemble the NIRSpec MOS observations from the Cosmic Evolution Early Release Science (CEERS;¹⁵ ERS-1345, PI: S. Finkelstein; S. Finkelstein et al. 2025, in preparation; also see S. L. Finkelstein et al. 2023a, 2023b), the Director's Discretionary Time (DDT) observations (DDT-2750, PI: P. Arrabal Haro; P. Arrabal Haro et al. 2023a, 2023b) in the CEERS field, the JWST Advanced Deep Extragalactic Survey (JADES;¹⁶ GTO-1180, GTO-1181, and GTO-1210, PI: Eisenstein; D. J. Eisenstein et al. 2023a), the JADES Origins Field (GO-3215, PI: Eisenstein; D. J. Eisenstein et al. 2023b; M. Rieke et al. 2023a), and the Ultra-deep NIRSpec and NIRCAM Observations before the Epoch of Reionization (UNCOVER;¹⁷ GO-2561, PIs: I. Labbé & R. Bezanson; R. Bezanson et al. 2024) and GO-4287 (PI: Mason). A full description of the sample selection and analysis methods applied to these public spectroscopic samples will be provided in Tang et al. (2025, in preparation); however, we provide a brief description in this Section. We obtained final 2D and 1D spectra following the reduction procedure described in Section 2.1. We also collect the HST/ACS+JWST/NIRCAM photometry available from R. Endsley et al. (2023) in the CEERS field, the JADES DR2 photometric catalog in the GOODS-S field (corresponding to sources observed in programs GTO-1180 and 1210, and GO-3215; M. J. Rieke et al. 2023a, 2023b), photometry from the DAWN JWST Archive (G. Brammer 2023; F. Valentino et al. 2023) in the

GOODS-N field (for GTO-1181), and the UNCOVER DR2 catalog from J. R. Weaver et al. (2024).

We follow the procedure outlined in M. Tang et al. (2023) to identify spectroscopic redshifts based on the H α (for $z \lesssim 6.7$) in addition to [OIII] + H β (for $z \lesssim 9.4$) emission lines. For the small number of systems at yet higher redshift, we utilized the strongest emission line (typically [NeIII], [OII], or CIII) if present; otherwise, we adopted the redshift implied by the Ly α continuum break. Break redshifts typically have larger uncertainties ($\sigma_z \sim 0.1$) than those measured from emission lines (e.g., G. C. Jones et al. 2024; K. N. Hainline et al. 2024); however, this does not significantly impact our results. In total, these efforts yield a parent sample of 737 galaxies with spectroscopic redshifts spanning $z = 3.90$ to 13.36 (median 5.29). This sample does not include the CIV emitter targeted in RXCJ2248-ID (M. W. Topping et al. 2024a) or any of the Abell 1703 sources presented in this paper. We will comment on how the detections in these samples compare to the overall population trends.

Following the methods outlined in M. Tang et al. (2023, 2024) and Z. Chen et al. (2024), we fit the HST/ACS+JWST/NIRCAM photometry of each of the 737 galaxies using BEAGLE following the model setup described in Section 2.2 with the redshifts fixed to the spectroscopic value. We utilize the best-fit SEDs to define the absolute UV magnitudes (M_{UV}) as well as to infer stellar population properties including stellar mass, SFR, and age from their best-fit SEDs. In addition, we measure [OIII] λ 5007 and H β EWs for each galaxy in the sample. In systems where the rest-optical continuum is detected at $> 3\sigma$, the optical-line EWs are measured directly from the spectrum. For these objects, we compare the measured EWs to the values inferred from the best-fit SED and achieve an excellent agreement. In the absence of a significant rest-optical continuum detection in the spectrum, we adopt the [OIII] λ 5007 and H β EWs derived from the best-fit SED.

Figure 16 presents the M_{UV} and combined [OIII] + H β EWs for the 737 galaxies comprising the spectroscopic sample. The absolute UV magnitudes of the spectroscopic sample range from $M_{UV} = -22.6$ to -16.1 , with a median value of -19.6 . This M_{UV} distribution is consistent with the UV-bright end of the UV luminosity distribution of photometrically selected objects (e.g., R. Endsley et al. 2024), the latter also including fainter systems (down to $M_{UV} = -16.0$) and having a luminous median M_{UV} (-18.0). Both the photometric and spectroscopic samples span the similar ranges of [OIII] + H β EW of 150–6000Å and 45–8300Å, respectively, and the median [OIII] + H β of the spectroscopic sample (710Å) is well matched to that of the photometric sample at fixed M_{UV} .

We select galaxies from the spectroscopic sample displaying CIV or NIV emission lines using a combination of visual inspection and S/N criteria. First, we measure emission-line fluxes by shifting the PRISM and grating spectrum into the rest frame, and fitting Gaussian profiles at the vacuum wavelength of each line. The centroids of the profiles were allowed to vary by one resolution element in the PRISM spectra (≈ 10000 km s $^{-1}$), and 1000 km s $^{-1}$ in the grating spectra to allow for small variations in the wavelength solution in addition to ensure capturing of resonance lines that do not necessarily trace the systemic redshift (e.g., CIV). Uncertainties are set by width of the flux distribution derived by repeatedly fitting profiles to 1000 instances of the spectrum perturbed by its error. Each $> 5\sigma$ CIV and NIV emission line was visually inspected to remove artifacts and poor fits to the data, and we verified that

¹⁵ <https://ceers.github.io/>

¹⁶ <https://jades-survey.github.io/>

¹⁷ <https://jwst-uncover.github.io/>

each emission line yielded consistent fluxes when covered by multiple observing modes. The resulting robust sample comprises 11 galaxies detected in either CIV (10 galaxies; Section 5.2) or NIV] (three galaxies; Section 5.3) spanning from $z = 5.449$ up to 10.621, which are presented in Table 5. The spectroscopic redshifts for each of these systems are measured from rest-optical emission lines, rather than the continuum break. Among the nine galaxies detected in CIV, the measured equivalent widths range from 4.9 Å up to 47.6 Å with a median of 25.4 Å, comparable to what is observed in A1703-zd2 and A1703-zd6. When present, the NIV] emission lines have EWs that span a smaller range (5.1–8.3 Å), which may contribute to their smaller sample size. Finally, we additionally select two (four) galaxies with tentative NIV] (CIV) detections, which satisfy only one of our S/N and visual inspection criteria (Table 5). The spectra of several of our robust sources have been previously presented in the literature, as indicated in Table 5. Additionally, we identify two new galaxies (JADES-202208 and 210003) with either a CIV or NIV] detection (Figure 15).

In addition, we present a deep, high-resolution ($R \simeq 2700$) NIRSpc spectrum of CEERS-1019 (i.e., EGSY8p7; A. Zitrin et al. 2015; G. W. Roberts-Borsani et al. 2016) in the rest-frame UV that reveals CIV emission (Whitler et al. 2025, in preparation). Previous spectroscopy using the $R \sim 1000$ grating from CEERS was not sufficiently deep to detect the CIV feature (e.g., R. L. Larson et al. 2023; M. Tang et al. 2023).¹⁸ We measure a total EW for the CIV emission in EGSY8p7 of $4.6_{-0.6}^{+0.5}$ Å. The CIV profile of EGSY8p7 is asymmetric with no sign of the blue doublet component. This is reminiscent of the line profile of RXCJ2248-ID and easily explained by resonant scattering effects (see M. W. Topping et al. 2024a). It is well-fit by a skewed Gaussian profile redshifted from the systemic wavelength. The properties of the fit are also similar to the RXCJ2248-ID line; we measure an FWHM of 310 km s^{-1} after correcting for the instrumental resolution ($\sim 100 \text{ km s}^{-1}$), and a velocity offset from CIV λ 1550 of the emission peak of $+190 \text{ km s}^{-1}$. Finally, the emission extends to yet higher velocities, with the best-fit profile extending above the error spectrum up to velocities of $+800 \text{ km s}^{-1}$.

In the following subsections, our primary goal is quantifying the incidence of CIV and NIV], independent of the powering mechanism of the lines. We do briefly consider whether any of our sources clearly stand out as having lines powered by AGN photoionization. Here we use the UV diagnostics discussed in Section 3.1 (e.g., A. Feltre et al. 2016; M. Mingozzi et al. 2022; J. Scholtz et al. 2023). Our measurements reveal CIV/He II ratios ($\gtrsim 1$) and CIII]/He II ratios ($\gtrsim 2$) that are consistent with stellar photoionization, as we also found for RXCJ2248-ID and A1703-zd6. We will discuss these in more detail in Plat et al. (2025, in preparation). Of course, very-high-redshift AGNs may have different spectra than those predicted in these models, and some level of mixing between AGN and stellar photoionization is also plausible. We therefore do not rule out the contribution from AGN photoionization in these sources. We note that one source (JADES-954) has been confirmed as a broad-line AGN in R. Maiolino et al. (2024b). We will discuss

this source in more detail below. One additional source (JADES-58975) was listed in the narrow-line AGN sample of J. Scholtz et al. (2023). We find that this spectrum has UV lines that are plausibly consistent with a stellar origin ($\text{OIII]}/\text{HeII} = 1.4$, $[\text{Ne IV}] \text{EW} < 30 \text{ \AA}$), but this does not significantly impact our demographic investigation below (see also, M. Curti et al. 2024).

5.2. The Demographics of CIV Emitters at $z \gtrsim 4$

We have presented new evidence in this paper that links nitrogen line emitters to those with strong CIV emission (see also M. W. Topping et al. 2024a; M. Castellano et al. 2024). In this subsection, we attempt to quantify the fraction of $z \gtrsim 4$ galaxies with strong CIV emission, establishing how commonly hard ionizing sources are present in early galaxies. This builds on earlier efforts to establish the CIV emitting fraction in the galaxy population with ground-based spectroscopy (R. Mainali et al. 2018).

We have identified 11 galaxies with robust CIV detections among the 737 systems in our $z > 4$ spectroscopic sample. Table 5 presents the properties of each of these systems. Seven of these CIV detections have been previously reported, including CEERS-1019 (EGSY8p7; R. L. Larson et al. 2023; Y. Isobe et al. 2023; M. Tang et al. 2023; R. Marques-Chaves et al. 2024), JADES-3991 (GNz11; A. J. Bunker et al. 2023; R. Maiolino et al. 2024a), CEERS-397 (Y. Harikane et al. 2024), JADES-954 (R. Maiolino et al. 2024b), JADES-1899 (M. Tang et al. 2024; J. Witstok et al. 2025), JADES-13176 (A. J. Cameron et al. 2023a), JADES-58975 (J. Scholtz et al. 2023; M. Curti et al. 2024), and UNCOVER-10646 and UNCOVER-22223 (S. Fujimoto et al. 2024). The CIV emission in JADES-210003 and JADES-202208 has not been previously reported, and we present their spectra in Figure 15.

The detection rate of CIV emitting galaxies (11 among 737 systems) is extremely low, as would be expected if the hard ionizing sources required to power strong CIV are only present in a small subset of the parent population. Of course, not all 737 galaxies have sufficiently deep spectra to place a meaningful limit on the CIV EW. To achieve a more robust CIV emitter fraction, we identify spectra with the depth to detect CIV with an $\text{EW} > 10 \text{ \AA}$ at the $> 5\sigma$ level. Of the 737 $z \gtrsim 4$ galaxies with spectra described in Section 5.1, we identify 99 systems with sufficient CIV sensitivity. With this more refined sample, we still find that a very small fraction (8%) of $z > 4$ galaxies show robust CIV emission with an EW in excess of 10 Å.

To understand the low success rate in detecting CIV emission, we compare the M_{UV} and $[\text{OIII}] + H\beta$ EWs of the CIV emitters to the full spectroscopic sample, as well as to a larger NIRCcam-based photometric sample of $z \sim 6-9$ galaxies from R. Endsley et al. (2024) in Figure 16. The eight CIV emitters span a fairly broad range of UV luminosities (M_{UV} of -21.6 to -17.7), with a median absolute UV magnitude of $M_{\text{UV}} = -19.6$). In contrast, the $[\text{OIII}] + H\beta$ EWs of the CIV emitters are far from typical. Nearly all of the CIV emitters have very large $[\text{OIII}] + H\beta$ EWs (median 3000 Å), indicating they are on the tail of the full distribution of galaxies.¹⁹ According to the $z \simeq 6-9$ $[\text{OIII}] + H\beta$ EW distribution in R. Endsley et al. (2024), the median $[\text{OIII}] + H\beta$ EW exhibited

¹⁸ CEERS observations targeting EGSY8p7 using the NIRSpc PRISM suffered from an electrical short resulting in significant excess emission throughout the detector. However, R. Marques-Chaves et al. (2024) noted the presence of a feature at the expected wavelength of CIV in the contaminated spectrum

¹⁹ One of the CIV emitters (UNCOVER-22223) lacks an $[\text{OIII}] + H\beta$ EW measurement as the lines are redshifted out of the NIRSpc wavelength coverage.

Table 5
Additional CIV and NIV] Emitters at $z \gtrsim 4$ Identified from Public NIRSspec Data Sets

Program	Object ID	RA	DEC	z_{spec}	M_{UV} (AB Mag)	[OIII] + H β EW (Å)	CIV EW (Å)	NIV] EW (Å)	NRS Mode	Ref.
Galaxies selected on NIV] emission										
CEERS(1345,4287)	1019	215.0353910	+52.8906620	8.678	$-22.4^{+0.1}_{-0.1}$	2599^{+642}_{-459}	$4.6^{+0.5}_{-0.6}$	$10.1^{+0.7}_{-0.8}$	R1000,R2700	[1],[2],[3],[4]
JADES(1181)	3991	189.1060540	+62.2420490	10.621	$-21.5^{+0.1}_{-0.1}$	—	$5.4^{+1.5}_{-2.9}$	$5.1^{+1.7}_{-1.7}$	PRISM,R1000	[5],[6]
JADES(3215)	202208	53.1640684	-27.7997202	5.449	$-20.6^{+0.1}_{-0.1}$	3268^{+112}_{-102}	$5.1^{+1.6}_{-2.6}$	$5.6^{+2.0}_{-2.0}$	PRISM,R1000	...
Galaxies selected on CIV emission without a robust NIV] detection										
CEERS(1345)	397 ^a	214.8361970	+52.8826930	6.000	$-21.4^{+0.1}_{-0.1}$	2396^{+95}_{-92}	$7.7^{+2.2}_{-2.4}$...	PRISM,R1000	[5],[7]
JADES(1181)	954 ^a	189.1519660	+62.2596350	6.761	$-19.9^{+0.1}_{-0.1}$	679^{+35}_{-36}	$23.3^{+3.8}_{-3.7}$...	PRISM,R1000	[5],[8]
JADES(1181)	1899	189.1977400	+62.2569640	8.279	$-19.5^{+0.1}_{-0.1}$	5039^{+702}_{-951}	$44.7^{+22.1}_{-14.7}$	$*27.5^{+21.6}_{-14.6}$	PRISM,R1000	[5] [9],[10],[11]
JADES(1210)	13176	53.1217573	-27.7976379	5.941	$-19.6^{+0.1}_{-0.1}$	4127^{+448}_{-392}	$39.5^{+3.5}_{-4.7}$...	PRISM,R1000	[5],[12]
JADES(1210)	58975	53.1124340	-27.7746090	9.436	$-20.2^{+0.1}_{-0.2}$	957^{+121}_{-101}	$9.2^{+1.1}_{-1.6}$...	PRISM,R1000	[5],[13],[14]
JADES(3215)	210003	53.1318414	-27.7737748	5.780	$-18.8^{+0.1}_{-0.1}$	3037^{+261}_{-212}	$26.3^{+3.8}_{-3.3}$...	PRISM,R1000	[5]
UNCOVER(2561)	10646	3.6369600	-30.4063620	8.511	$-21.6^{+0.1}_{-0.1}$	3733^{+341}_{-335}	$11.5^{+1.9}_{-1.7}$...	PRISM	[5],[15]
UNCOVER(2561)	22223	3.5681150	-30.3830520	9.570	$-17.7^{+0.1}_{-0.1}$...	$22.8^{+7.2}_{-6.4}$...	PRISM	[5],[15]
Tentative NIV]-Emitters										
JADES(1181)	3990	189.0169950	+62.2415820	9.374	$-20.7^{+0.1}_{-0.1}$...	—	$*12.4^{+10.0}_{-5.9}$	PRISM,R1000	[5],[16]
UNCOVER(2561)	34265	3.6071810	-30.3648170	6.354	$-18.7^{+0.1}_{-0.1}$	1115^{+275}_{-225}	...	$*10.0^{+4.2}_{-2.8}$	PRISM	[5]
Tentative CIV-Emitters										
JADES(1210)	5173	53.1568262	-27.7671606	7.980	$-18.9^{+0.2}_{-0.1}$	1021^{+261}_{-288}	$*27.1^{+4.0}_{-4.3}$...	PRISM,R1000	[5]
JADES(1210)	9903	53.1690468	-27.7788335	6.631	$-18.6^{+0.1}_{-0.1}$	2564^{+437}_{-380}	$*19.5^{+2.2}_{-2.4}$...	PRISM,R1000	[5]
UNCOVER(2561)	10155	3.5822060	-30.4071140	5.660	$-16.4^{+0.1}_{-0.1}$	2671^{+1291}_{-1307}	$*73.7^{+25.5}_{-16.2}$...	PRISM	[5]
UNCOVER(2561)	23604	3.6052470	-30.3805840	7.882	$-18.3^{+0.1}_{-0.1}$	668^{+313}_{-190}	$*36.8^{+7.3}_{-6.0}$...	PRISM	[5],[17]

Note. We list the JWST program where the NIRSspec observation is taken, their IDs, coordinates, spectroscopic redshifts, absolute UV magnitudes (M_{UV}), [OIII]+H β equivalent widths, the CIV and NIV] equivalent widths, the mode of the NIRSspec observations (i.e., prism or $R \sim 1000$ medium grating), and literature references when available. Here, the M_{UV} for UNCOVER sources in the Abell 2744 cluster have been corrected for gravitational lensing with the L. J. Furtak et al. (2023) lensing map. For [OIII]+H β EWs, we adopt the values derived directly from the prism spectra when the rest-optical continuum is detected, and values inferred from NIRCcam SED fitting in other cases. Emission-line EWs marked with an “*” are designated as tentative.

^a Broad-line AGNs reported in Y. Harikane et al. (2023) and R. Maiolino et al. (2024b).

References. [1] R. L. Larson et al. (2023); [2] Y. Isobe et al. (2023); [3] M. Tang et al. 2023; [4] R. Marques-Chaves et al. (2024); [5] K. E. Heintz et al. (2025); [6] A. J. Bunker et al. (2023); [7] Y. Harikane et al. (2023); [8] R. Maiolino et al. 2024b; [9] J. Wistok et al. 2025; [10] M. Tang et al. 2024; [11] R. Navarro-Carrera et al. (2024); [12] A. J. Cameron et al. (2024); [13] J. Scholtz et al. 2023; [14] M. Curti et al. 2024; [15] S. Fujimoto et al. 2024; [16] D. Schaerer et al. 2024; [17] Z. Chen et al. 2024.

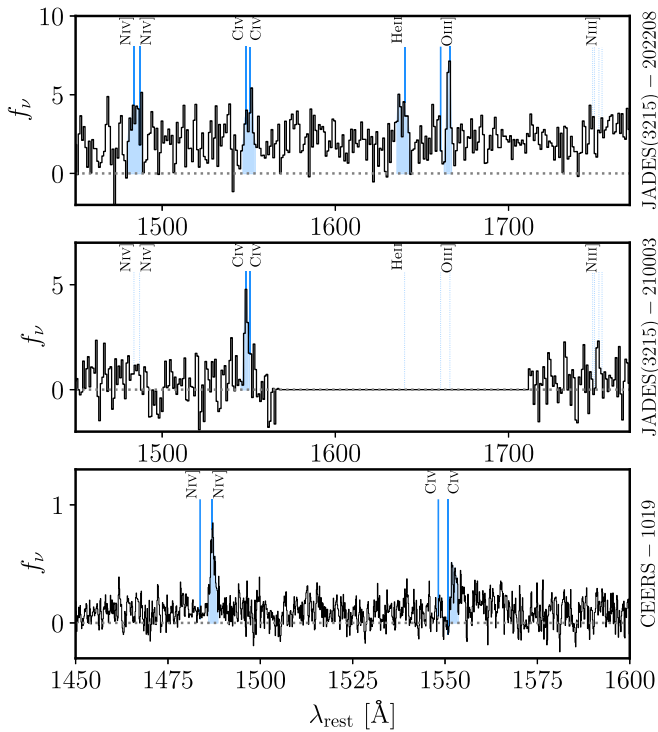


Figure 15. Spectra for galaxies with previously unreported CIV or NIV] detections presented in the rest frame. The top, center, and bottom panels show the spectra for JADES-202208, JADES-210003, and CEERS-1019, respectively, as indicated by their labels on the right (see also Table 5). The spectra of JADES-202208 and JADES-210003 were obtained using the $R \sim 1000$ G140M grating, and CEERS-1019 was obtained using the $R \sim 2700$ G140H grating. The spectrum of JADES-210003 between 1565–1710 Å is covered by the NIRSpect detector gap. The wavelength range of the CEERS-1019 spectrum is narrowed to better show the emission lines at high resolution, and none of the redder rest-UV lines (i.e., He II λ 1640, OIII] λ 1666, 1666, NIII] λ 1750) are detected at $> 3\sigma$. Vacuum wavelengths of emission lines in the rest-UV are indicated by vertical blue lines that are labeled at the top of each panel. Emission lines that are detected have their fluxes shaded blue. A 5σ detection of NIV] λ 1486 in CEERS-1019 was previously reported by R. L. Larson et al. (2023) and Y. Isobe et al. (2023), now detected at 17σ in the $R \sim 2700$ spectrum. This spectrum also presents the first detection of CIV in CEERS-1019 using the NIRSpect grating.

by the CIV emitters corresponds to the upper 2% of the population. There is one CIV emitter in our sample (JADES 1181-954) that shows relatively small [OIII] + $H\beta$ EW (679 Å), distinguishing it from the rest of the sample. This source is a broad-line AGN with a very red optical continuum (R. Maiolino et al. 2024b). It is likely that the AGN is contributing significantly to the continuum flux density in the rest-optical, decreasing the [OIII] + $H\beta$ EW from what would have been observed from the host galaxy.

The large optical-line EWs are consistent with expectations for extremely young stellar populations, formed in a recent strong burst of star formation. Indeed, the BEAGLE SEDs that describe these systems show a median constant star formation age of just 5 Myr. These results are consistent with our findings for A1703-zd6 and RXCJ2248-ID, where [OIII] + $H\beta$ EWs are large (4120 and 3100 Å, respectively) and stellar population ages are young ($1.6^{+0.5}_{-0.4}$ and $1.8^{+0.7}_{-0.4}$ Myr, respectively). Based on these results, we suggest that the rarity of strong CIV emission is likely due to the [OIII] + $H\beta$ EW (or age) threshold required to power the high-ionization lines. Only a small fraction of the galaxy population is found with the extremely young stellar population ages that are linked to the large [OIII] + $H\beta$ EWs

associated with strong CIV emission. If we consider only those objects in the parent spectroscopic sample with [OIII] + $H\beta$ EWs larger than 2000 Å (and spectra sufficiently deep to detect CIV with $EW > 10$ Å), we find that 40% (5 of 12) show strong CIV emission (> 10 Å). This suggests that hard ionizing sources capable of powering CIV are likely fairly common in galaxies in a brief (few megayears) window following a strong burst of star formation. By selecting galaxies with very high [OIII] + $H\beta$ EWs (via photometric flux excesses or spectroscopy), it should be possible to build a larger sample of systems with high-ionization lines in the rest-UV.

We compare the CIV EWs of the $z \gtrsim 4$ galaxies to local star-forming systems (e.g., D. A. Berg et al. 2016, 2019; Y. I. Izotov et al. 2016a, 2016b, 2018a, 2018b, 2024; P. Sencchna et al. 2017, 2019) with similar $H\beta$ EW in Figure 17. These two quantities provide insight into how the hard radiation field varies with the stellar population age. We see that local metal-poor galaxies often power relatively weak CIV emission (1–10 Å) at $H\beta$ EW = 100–300 Å. In contrast, the early galaxies with CIV detections extend to much higher CIV EWs ($\gtrsim 20$ –50 Å) than are seen locally at similar $H\beta$ EWs. While several newly discovered local systems are beginning to approach the intense CIV EWs found in the reionization era (e.g., Y. I. Izotov et al. 2024), it appears that these very large CIV EWs are not the norm in strong bursts of star formation at low redshift. This may indicate that the stellar populations in reionization era galaxies host harder ionizing sources, or it could hint at some contribution from AGN photoionization. Alternatively, a larger fraction of the resonant CIV emission may be escaping from very-high-redshift galaxies (see P. Sencchna et al. 2022), with observed EWs approaching the maximum CIV EW achievable by stellar photoionization models (Plat et al. 2025, in preparation). Deeper spectra of the CIV emitters should reveal which of these is most likely to be driving the stronger high-ionization line emission seen at $z \gtrsim 4$.

5.3. The Demographics of NIV] Emitters at $z \gtrsim 4$

We now quantify the prevalence of the NIV] emitters in the spectroscopic sample. As described in Section 5.1, we recover three systems with significant NIV] detections (Table 5) including GN-z11 (A. J. Bunker et al. 2023) and CEERS-1019 (R. L. Larson et al. 2023; Y. Isobe et al. 2023; R. Marques-Chaves et al. 2024), as well as one new source (MSA ID: JADES-202208). We display the spectrum of JADES-202208 ($z = 5.449$) in Figure 15. The NIV] emission is detected at $S/N = 5.0$, along with CIV ($S/N = 5.1$), He II ($S/N = 4.4$), and a strong detection of the OIII] auroral line ($S/N = 4.9$). The NIV] EW ($5.1^{+1.6}_{-2.6}$ Å) and CIV EW ($5.6^{+2.0}_{-2.0}$ Å) are comparable, while the [OIII] + $H\beta$ EW (3268 Å) is among the largest in the parent catalog.

The recovery of only three NIV] lines in a redshift catalog of 747 galaxies highlights the challenges in blindly increasing the nitrogen line sample with nontargeted spectroscopy. One reason for the low detection rate is that the nitrogen lines are typically weak ($EW \simeq 5$ –10 Å), requiring extremely deep rest-UV spectroscopy for meaningful limits in fainter sources. To quantify the fraction of nitrogen line emitters in the $z > 4$ galaxy sample, we only consider spectra where an NIV] line with an EW larger than 5 Å can be constrained at $> 5\sigma$. This limiting EW is stricter than the one imposed for CIV in Section 5.2 reflecting the typically weaker NIV] line. Of the

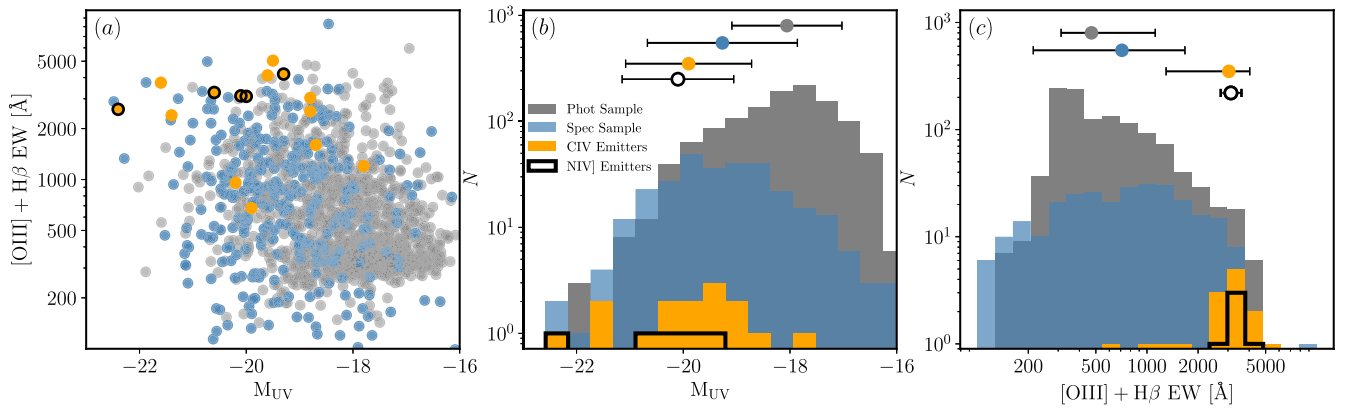


Figure 16. $[OIII] + H\beta$ EW versus M_{UV} of robust NIV] (black) and CIV (orange) emitters compared to the full sample of spectroscopic (teal) and photometric (gray) measurements (panel (a)). Panels (b) and (c) provide the distributions of M_{UV} and $[OIII] + H\beta$, respectively, for the four samples. In these panels, the points and error bars above each histogram display the median and standard deviation, respectively, of each sample. The CIV and NIV] emitters appear to have UV luminosities at or above the median of the spectroscopic sample; however, nearly all of these objects have EWs elevated significantly above the sample average. The two CIV emitters with $[OIII] + H\beta$ EWs that are $< 1000\text{\AA}$ have been shown to display evidence of AGN activity (J. Scholtz et al. 2023; R. Maiolino et al. 2024b).

737 galaxies across the full sample, only 38 are of sufficient depth to reach this limit. Given the three NIV] detections, this suggests that 7% of $z \gtrsim 4$ galaxies with sufficiently deep JWST spectra exhibit NIV] with $EW > 5 \text{\AA}$. This fraction is comparably low to that found for strong CIV emitting galaxies, suggesting that the majority of early galaxies are not observed in a phase with very hard ionizing sources and enhanced nitrogen.

To understand what makes nitrogen line emitters rare at $z \gtrsim 4$, we compare the absolute magnitude and $[OIII] + H\beta$ EWs of the NIV] emitters to the parent spectroscopic sample in Figure 16. Currently, the NIV] detections are primarily limited to the bright galaxies (median $M_{UV} = -21.1$), which is not surprising given the sensitivity to detect NIV]. It is conceivable that deeper spectroscopy (or highly magnified sources in cluster fields) may reveal strong nitrogen line emission in fainter galaxies. What does appear to be clear is that the NIV] emitters exclusively have very large $[OIII] + H\beta$ EWs (2600-4200Å), placing them in the upper 2% of the EW distribution at similar redshifts and indicating extremely young stellar populations (J. Matthee et al. 2023; R. Endsley et al. 2024). Of course, very large $[OIII] + H\beta$ EWs are also found in RXCJ2248-ID and A1703-zd6, neither of which is included in the sample described above. If we consider galaxies with high $[OIII] + H\beta$ EWs ($> 2000\text{\AA}$) and spectra deep enough to recover NIV] emission at our EW limit, we find that nitrogen emitters comprise a much larger fraction (30%) of the population. Spectroscopic programs targeting the highest equivalent width optical line emitters may provide a more efficient means of identifying additional nitrogen emitters.

6. Discussion

Over the past several years, a distinct phase in the early evolution of reionization-era galaxies has been uncovered by deep spectroscopy. The first glimpse of galaxies in or near this phase was via discovery of prominent CIV emission detected pre-JWST in a handful of luminous lensed systems, a transition rarely encountered in nebular emission at such strengths in lower-redshift star-forming systems (D. P. Stark et al. 2015a; R. Mainali et al. 2017; K. B. Schmidt et al. 2017). More recently, the detection of strong lines of ionized nitrogen including NIV] in GN-z11 clearly established that some high-

redshift galaxies harbor gas in a remarkable nitrogen-enriched and high-density phase that is not yet fully understood (A. J. Bunker et al. 2023; A. J. Cameron et al. 2023a; P. Senchyna et al. 2023; R. Maiolino et al. 2024a). In M. W. Topping et al. (2024a) and this paper, we have shown that both prominent $z > 6$ CIV emitters known before JWST's launch also reveal signatures of dense, nitrogen-enriched gas, suggesting that these two phenomena are potentially linked.

With improved statistics on the demographics of nitrogen emitters, we can begin to place some constraints on the nature of this observational phase. The clear association of strong CIV and NIV] detections with very intense optical nebular emission ($H\beta$ EW $\gtrsim 400 \text{\AA}$) in a sample of over 700 $z \gtrsim 4$ galaxies establishes that this is likely a short-lived phase during bursts of star formation. The elevated $H\beta$ EWs correspond to galaxies caught with very large instantaneous sSFR. In the context of bursty SFHs likely to be present at $z \gtrsim 6$ (e.g., X. Ma et al. 2018; S. R. Furlanetto & J. Mirocha 2022; V. Strait et al. 2023; T. Dome et al. 2024; R. Endsley et al. 2024) the largest sSFRs will be found in galaxies with the highest-amplitude bursts (i.e., the highest star formation rate at fixed stellar mass) observed near the peak of this star formation activity. The $H\beta$ EWs thus depend both on the light-weighted stellar population age and on the relative strength of the burst. The demographic trends we found in Section 5 may therefore suggest that the nitrogen enrichment is limited to the highest peak intensity bursts of star formation. Specifically, while galaxies with reasonably intense line emission ($H\beta$ EW $\simeq 200\text{\AA}$) are likely in the midst of recent upturns of star formation, they appear not to power the nitrogen emission seen in more intense bursts. We illustrate this schematically in Figure 18.

The fact that these nitrogen signatures are only observed at the highest sSFRs is an important clue as to their nature. It is natural to expect that galaxies undergoing the strongest bursts are likely to have unique ISM conditions. In particular, we expect the cold gas densities to reach extremely high values in these systems (e.g., J.-G. Kim et al. 2021; M. Y. Grudić et al. 2021) where the cluster formation efficiency may be elevated (e.g., A. Adamo et al. 2011; A. Adamo et al. 2015; X. Ma et al. 2020). Hence, the nitrogen line emitters appear to be preferentially found in galaxies that are likely to be forming very dense star cluster complexes, potentially similar to the conditions under which globular clusters formed. This fact also

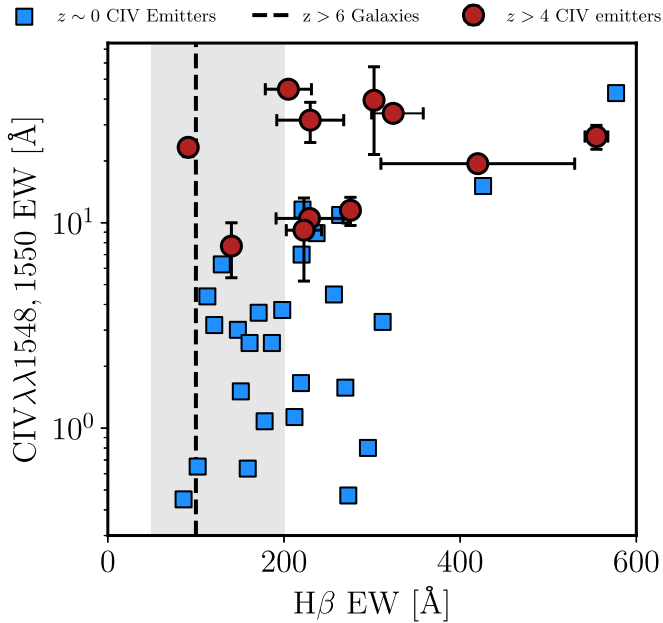


Figure 17. CIV EW versus $H\beta$ EW for galaxies in the local Universe (blue squares) and at high redshift (red circles). The high-redshift CIV-emitter sample includes objects in the A1703 field in addition to RXCJ2248-ID (M. W. Topping et al. 2024a) and the CIV emitters identified in Table 5. The local comparison samples include objects presented by P. Senchyna et al. (2017, 2019), Y. I. Izotov et al. (2016a, 2016b; 2018a, 2018b, 2024), and D. A. Berg et al. (2016, 2019). We indicate the average $H\beta$ EW and the 1σ distribution width at $z > 6$ as the vertical dashed line and shaded region, respectively, from the photometric sample of R. Endsley et al. (2024). The high-redshift galaxies nearly universally have higher CIV EWs than the local samples. For $H\beta$ EWs of 100–300 Å, the highest CIV EWs locally only reach ≈ 10 Å, while several galaxies at $z > 4$ exceed 30 Å. At the highest $H\beta$ EWs (> 400 Å), the local and high-redshift galaxies have comparable CIV EWs, implying they may be reaching the maximum EW that can be produced by photoionization from massive stars.

suggests that the abundances are short-lived in the ionized gas phase, as otherwise, we would expect to find similar evidence for nitrogen overabundances (in these or lower-ionization nitrogen lines) in galaxies with somewhat less extreme optical equivalent widths, representing the same bursts at somewhat older ages. Some combination of processes must alter this situation on a short (of the order of a megayear; Section 5.2) timescale: for instance, ongoing star formation involving this gas (as is the case if some of this material is locked up in stars with globular cluster-like abundance patterns), stellar feedback heating, and evacuating this gas, yields from Type II supernovae or time-integrated normal massive star winds polluting this material (which should boost oxygen and carbon relative to nitrogen; e.g., K. Nomoto et al. 2013; C. Charbonnel et al. 2023), or inflows of pristine gas diluting these abundances.

However, high sSFR alone is clearly not sufficient to produce the conditions responsible for this enrichment. Strong bursts with similar $H\beta$ EWs in the local Universe do not appear to show the prominent nitrogen lines being recovered at $z \gtrsim 6$ (e.g., Y. I. Izotov et al. 2016a, 2016b, 2018b, 2024; D. A. Berg et al. 2019; P. Senchyna et al. 2017, 2019). This suggests that the conditions required to produce the anomalous nitrogen abundance pattern may be uniquely present in high-redshift galaxies, perhaps reflecting different star formation processes. One possibility is that the combination of high gas densities and low metallicities (thought to be common at $z \gtrsim 6$) may lead to rapid cooling times and less effective feedback, resulting in

elevated star formation efficiencies in a subset of early galaxies (A. Dekel et al. 2023; Z. Li et al. 2024). If present in early galaxies, these so-called “feedback-free starbursts” (FFBs) would likely be the highest sSFR galaxies at a given epoch, the same population that appears to often show CIV and NIV] detections. We note that the compact star-forming complexes associated with the nitrogen enhancements do appear to reach stellar mass surface densities (M. W. Topping et al. 2022) where feedback-free starburst conditions may be expected (M. Y. Grudić et al. 2021). Hence, while FFBs have recently been discussed as a means of explaining the excess of galaxies at $z \gtrsim 10$, they may also play an important role in driving the nitrogen-enhanced abundance pattern that is being seen in the strongest bursts of the reionization era and in the fossil record of globular clusters (see also, e.g., A. Renzini 2023).

The ionizing sources responsible for driving the nitrogen enhancement have been discussed at length in the recent literature (e.g., P. Senchyna et al. 2023; D. Nandal et al. 2024b; M. W. Topping et al. 2024a; M. Castellano et al. 2024; R. Maiolino et al. 2024a; R. Marques-Chaves et al. 2024). With improved constraints on the demographics of this population, we can gain new insights into the nature of this population. The fact that this abundance pattern is only found in very strong bursts where densities are large is consistent with a picture where dynamical interactions play an important role in forming the polluting sources (M. Gieles et al. 2018; F. Martins et al. 2020; C. Charbonnel et al. 2023), as pointed out previously (P. Senchyna et al. 2023). Runaway collisions may alter the stellar IMF in these dense stellar systems, creating a population of very massive stars (VMSs; $\approx 10^2$ – $10^3 M_\odot$) or supermassive stars (SMSs; $\approx 10^3$ – $10^5 M_\odot$). The contribution of both populations to the nitrogen-enhanced abundance pattern has been recently investigated in some detail (e.g., C. Nagele & H. Umeda 2023; C. Charbonnel et al. 2023; P. Senchyna et al. 2023; M. W. Topping et al. 2024a; D. Nandal et al. 2024b; R. Marques-Chaves et al. 2024). If low-metallicity VMSs altered by interactions and mergers are present in nitrogen emitters, we would expect a hard radiation field, perhaps even more intense than is commonly found in metal-poor galaxies locally. This may help explain the intense CIV emission in these systems, with EWs in excess of most local samples (Figure 17). In contrast, the SMSs are not expected to power hard radiation fields (e.g., M. Gieles et al. 2018; F. Martins et al. 2020), so if such a population was responsible for expelling the nitrogen-enriched material, we would likely also need there to be a separate population of hard ionizing sources to power the high-ionization lines. Or we may be witnessing a later evolution stage (following the SMS phase) during a second burst of star formation, where massive stars forming from already-enriched material now photoionize their nitrogen-enhanced surroundings. Along these lines, the potentially important role of multiple bursts in explaining the abundance pattern has been discussed in C. Kobayashi & A. Ferrara (2024). In multiple burst scenarios, a key prediction is that there should be a population of strong bursts without significant nitrogen emission lines (i.e., the first burst in such scenarios). The demographics presented in Section 5 are to first order consistent with this possibility, as not all galaxies with $H\beta$ EW $\gtrsim 400$ Å support strong nitrogen line emission. More detailed comparison of formation models to these demographics may aid in differentiating between these scenarios.

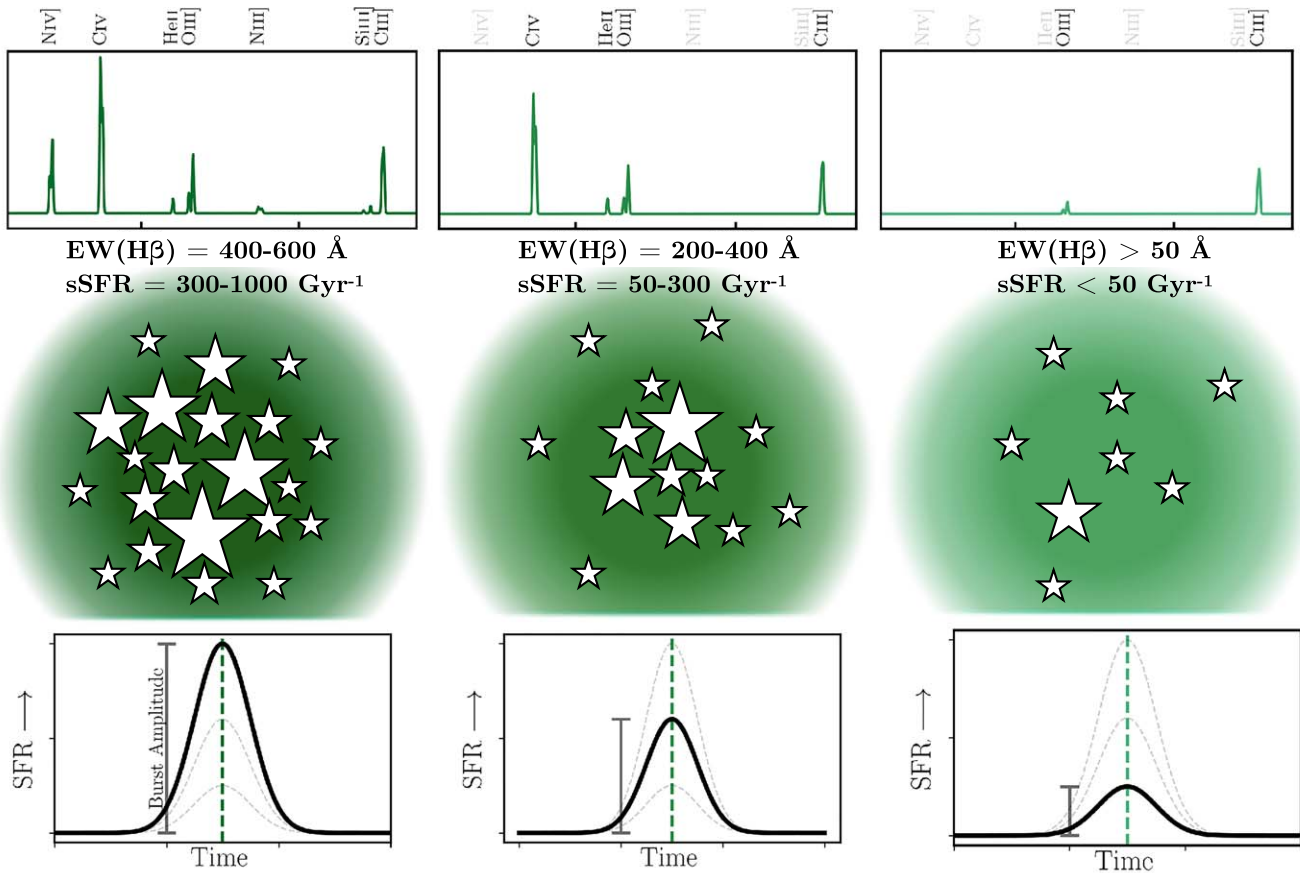


Figure 18. Schematic demonstrating the physical scenarios that result in a given rest-frame UV spectrum. The left panels present a UV spectrum that contains high-ionization lines (e.g., He II and CIV) along with strong nitrogen lines (e.g., NIV] and NIII]) such as those seen in A1703-zd6 (this work) and RXCJ2248-ID (M. W. Topping et al. 2024a). In this scenario, the UV lines are driven by a significant burst of star formation ($sSFR = 300\text{--}1000\text{Gyr}^{-1}$), which also drives very strong rest-optical emission lines ($H\beta$ EW = 400–600Å). The middle panels reflect rest-UV spectra such as those of A1703-zd2 and A1703-zd5.2, which display strong high-ionization lines (CIV and He II), but do not show emission from nitrogen. These systems are driven by a moderate burst of star formation ($sSFR = 50\text{--}300\text{Gyr}^{-1}$) and have above-average rest-optical emission line EWs ($H\beta$ EW = 200–400Å). The right panels demonstrate a scenario where the most massive stars are absent, representing recent star formation activity corresponding to an $sSFR$ of $< 50\text{Gyr}^{-1}$. These systems do not have the ionizing radiation field capable of driving CIV and He II emission, and do not have an ISM enriched in nitrogen, and display $H\beta$ EWs down to $\approx 50\text{Å}$. The most common line seen in the rest-frame UV for this scenario is CIII].

It has been recently noted (e.g., R. Marques-Chaves et al. 2024) that the dense conditions in the nitrogen emitters also appear optimized for creating intermediate-mass black holes (IMBHs). If VMSs or SMSs are common in the star clusters of nitrogen emitters (see discussion above), they may provide an efficient path for the formation of black holes, with subsequent growth from tidal disruption events and black hole mergers (e.g., G. D. Quinlan & S. L. Shapiro 1990; S. F. Portegies Zwart et al. 2004; A. Rantala et al. 2024). In cases where this picture holds, the nitrogen emitters at $z \gtrsim 6$ may correspond to an early phase where relatively massive black holes are efficiently formed following intense and dense bursts of star formation. In multiple burst scenarios (e.g., C. Kobayashi & A. Ferrara 2024), it is possible that IMBHs could have already assembled in earlier star formation episodes. In this case, the nitrogen emitters may already harbor relatively massive black holes, which may be fueled during the current burst of star formation. Here we may expect to see AGN signatures, as is plausibly the case for GNz11 (R. Maiolino et al. 2024a). Distinguishing between these cases requires confirmation of the presence of VMSs or SMSs in the nitrogen emitters or their progenitors.

Many of the outstanding questions about these objects are connected to the uncertain nature of the stellar populations and ionizing sources powering them. An important first step in characterizing such massive star populations was taken in T. E. Rivera-Thorsen et al. (2024), using deep JWST spectroscopy of the $z = 2.37$ Sunburst Arc, probing the rest-frame optical of this object. The Sunburst Arc is a crucial lower-redshift laboratory for understanding these $z > 6$ spectra, as the rest-UV spectrum of the highly lensed LyC-leaking cluster in this galaxy reveals similarly prominent NIII] emission requiring significant nitrogen enrichment: $N/O = 0.6$ (M. Pascale et al. 2023), albeit at a much smaller mass scale (a lensed single cluster) and likely higher metallicity (plausibly consistent with the lack of NIV] emission). The new JWST spectra reveal strong broadened stellar wind emission in both the blue and red “bumps” typically associated with Wolf-Rayet (W-R) stars (T. E. Rivera-Thorsen et al. 2024). These bumps are composed of blended lines of (predominantly) ionized nitrogen/helium and carbon, respectively; and their detection supports the presence of a prominent population of luminous and stripped (or otherwise processed to reveal layers exposed to hot H-burning) massive stars driving dense, highly ionized winds. This may be critical to understanding the source

of the nitrogen-enriched material seen in the ionized gas phase in this object. The strong winds of very massive stars ($\sim 100\text{--}1000 M_{\odot}$) near the Eddington limit are a natural source of nitrogen-enriched material themselves (e.g., J. S. Vink 2023), and are expected to be visible in both optical W-R bumps (e.g., F. Martins & A. Palacios 2022). However, the wind signatures of these VMSs are highly sensitive to mass-loss rates and to detailed evolution and wind modeling, and they are challenging to disentangle from “classical” W-R stars in integrated light (e.g., F. Martins et al. 2023). If VMS or W-R winds are directly responsible for the pollution observed in these $z > 6$ sources, deep UV spectroscopy promises to readily reveal their continuum signatures even at low metallicities (e.g., P. Senchyna et al. 2021; F. Martins et al. 2023); and in any case, detailed comparisons both with lower-redshift samples and with population synthesis predictions including these sources would enable the first characterization of their constituent massive stars and a critical test for the various enrichment scenarios.

7. Summary

We present new JWST/NIRSpec observations of galaxies in the Abell 1703 field. Our primary target is A1703-zd6, a bright ($H = 25.9$) $z = 7.0435$ galaxy known to power strong CIV emission from ground-based observations (D. P. Stark et al. 2015b). The new NIRSpec spectrum spans the rest-UV to optical, constraining the metal content, abundance pattern, and ionizing sources linked with such strong CIV emission. We also present spectra of seven additional bright ($H = 23.8\text{--}25.9$) $z \simeq 6\text{--}8$ galaxies in the Abell 1703 field. To place these results in context, we investigate the prevalence of CIV and nitrogen lines in a newly constructed redshift catalog of 737 $z \gtrsim 4$ galaxies with public NIRSpec spectra.

One of our central goals is to understand the physical conditions that lead to the nitrogen enhancements seen in recent metal-poor galaxies at high redshift (A. J. Bunker et al. 2023; R. Marques-Chaves et al. 2024; M. W. Topping et al. 2024a), testing whether there is a link between the presence of hard radiation fields and the anomalous abundance pattern. We summarize our primary findings below.

1. The rest-UV spectrum of A1703-zd6 confirms the strong CIV emission ($EW = 19.4 \text{ \AA}$) seen with Keck, while also revealing strong emission from a suite of other emission lines (i.e., OIII], CIII], He II). The CIV EW is larger than that seen in most metal-poor star-forming galaxies found in nearby ($z < 0.02$) galaxies. The line ratios indicate a hard radiation field ($CIV/CIII] = 3.3$), albeit consistent with expectations for stellar photoionization.

2. The rest-optical spectrum of A1703-zd6 exhibits a suite of strong emission lines. The [OIII]+H β EW (4116 \AA) is extremely large, corresponding to the upper 0.5% of EWs seen in the reionization-era. The ionized gas is found to be metal poor ($12 + \log(O/H) = 7.47$) and very high in electron density ($8\text{--}19 \times 10^4 \text{ cm}^{-3}$). The elevated gas densities result in collisional de-excitation of [OII] (boosting the O32 ratio) and strong He I lines ($He I \lambda 5876/H\beta = 0.26$). The spectral features are similar to those of RXCJ2248-ID (M. W. Topping et al. 2024a), suggesting high densities are a feature of HII regions in reionization-era galaxies with the largest [OIII] and H β EWs.

3. We find that the emission-line spectrum of A1703-zd6 can be explained by a low-metallicity young (1.6 Myr) stellar population formed in a recent burst of star formation. The

stellar mass ($10^{7.70} M_{\odot}$) associated with the burst appears concentrated in a compact (unresolved) region < 120 pc in size. NIRCам imaging will be required to put a more stringent limit on the size. Nonetheless, the current measurement suggests that A1703-zd6 hosts a high density of metal-poor massive stars.

4. The rest-UV spectrum of A1703-zd6 reveals strong [NIV] and [NIII] emission lines, indicating that the ionized gas is both elevated in nitrogen and deficient in oxygen ($\log(N/O) = -0.6$). The abundance pattern is similar to that seen in GNz11 (A. J. Bunker et al. 2023) and RXCJ2248-ID (M. W. Topping et al. 2024a). The discovery of nitrogen enhancements in both A1703-zd6 and RXCJ2248-ID, two galaxies identified based on strong CIV emission, suggests that there may be a physical link between the presence of hard ionizing sources and the processes leading to the elevated nitrogen content in the ISM. We suggest that both may be related to a dense clusters of massive stars formed after a strong burst of star formation.

5. We also find strong CIV emission ($EW = 10.5$ and 31.6 \AA) in A1703-zd2 and A1703-zd5.2, two $z \gtrsim 6$ galaxies with rest-optical emission lines suggesting metal-poor gas ($12 + \log(O/H) = 7.35 \pm 0.30$ and 7.26 ± 0.28). Both galaxies are also found to lie above the star-forming main sequence at $z \simeq 6\text{--}8$ with large specific star formation rates (59 and 32 Gyr^{-1} assuming a CSFH). The H β EWs are very large (209 \AA and 170 \AA), yet they are $\gtrsim 2 \times$ less than A1703-zd6. Neither source shows evidence for nitrogen enhancements. Doublet ratios suggest electron densities are large ($1\text{--}2 \times 10^4 \text{ cm}^{-3}$) but not as elevated as the sources showing the nitrogen emission. We suggest that the H β EW is likely to provide the best indicator of whether a galaxy exhibits nitrogen enhancements seen in a handful of early JWST spectra.

6. To better test this physical picture, we investigate the spectra of 737 $z \gtrsim 4$ galaxies available in our reductions of the public JWST database. Strong CIV ($> 10 \text{ \AA}$) and [NIV] ($> 5 \text{ \AA}$) emission is extremely rare, found in only 8% and 7% of $z \gtrsim 4$ galaxies, respectively, where we only consider those spectra sufficiently deep to reach the respective EW limits. We find that the strong UV lines are primarily seen in galaxies with extremely large [OIII]+H β EWs ($> 2500 \text{ \AA}$), corresponding to extremely young stellar populations (< 5 Myr) formed in a recent strong burst of star formation. Such extremely young ages are rare in early star-forming systems. Targeted observations of galaxies with these large optical line EWs should yield larger samples of nitrogen-enhanced galaxies with hard ionizing sources.

Acknowledgments

M.W.T. acknowledges support from the NASA ADAP program through grant No. 80NSSC23K0467. D.P.S. acknowledges support from the National Science Foundation through grant AST-2109066. A.Z. acknowledges support from grant No. 2020750 from the United States-Israel Binational Science Foundation (BSF) and grant No. 2109066 from the United States National Science Foundation (NSF); from the Ministry of Science & Technology, Israel; and from the Israel Science Foundation, grant No. 864/23.

This work is based in part on observations made with the NASA/ESA/CSA James Webb Space Telescope. The data were obtained from the Mikulski Archive for Space Telescopes at the Space Telescope Science Institute, which is operated by the Association of Universities for Research in

Astronomy, Inc., under NASA contract NAS 5-03127 for JWST. The authors acknowledge the CEERS, DDT-2750, and UNCOVER teams led by Steven L. Finkelstein, Pablo Arrabal Haro, and I. Labbé & R. Bezanson for developing their observing program with a zero-exclusive-access period. Some of the data products presented herein were retrieved from the Dawn JWST Archive (DJA). DJA is an initiative of the Cosmic Dawn Center (DAWN), which is funded by the Danish National Research Foundation under grant DNRF140.

Data Availability

The data underlying this article may be presented upon reasonable request to the corresponding author.

Appendix A

Emission-line Fluxes and Equivalent Widths

Tables 6 and 7 provide the full set of emission lines in the rest-frame UV and optical, respectively, that we measured for the spectroscopic sample.

Table 6
Emission-line Fluxes and Equivalent Widths of Rest-frame UV Features for Our JWST/NIRSpec Sample of Galaxies in Abell 1703

Line	A1703-zd1	A1703-zd2	A1703-zd5.1	A1703-zd5.2	A1703-23	A1703-zd4	A1703-zd6
	Line Flux [10^{-19} erg/s/cm 2]						
Ly α	-	-	-	-	-	7.9 \pm 1.6	249.5 \pm 9.3
NIV] λ 1483	< 4.2	< 4.1	< 11.2	< 8.6	< 6.8	< 4.2	5.8 \pm 1.9
NIV] λ 1486	< 4.4	< 4.8	< 9.8	< 10.9	< 7.3	< 3.9	12.3 \pm 1.6
CIV] λ 1549	-	20.1 \pm 2.4	< 14.6	51.9 \pm 4.7	< 10.6	< 6.1	57.0 \pm 3.1
HeII] λ 1640	< 3.9	6.5 \pm 1.5	< 9.5	< 9.5	< 4.9	< 3.7	6.8 \pm 1.1
OIII] λ 1660	< 4.0	< 4.4	< 10.1	< 9.4	7.0 \pm 1.7	< 4.6	10.7 \pm 1.7
OIII] λ 1666	< 3.5	< 6.1	< 9.9	16.0 \pm 2.9	7.2 \pm 1.8	< 4.3	19.8 \pm 1.8
NIII]1750	< 5.1	< 6.3	< 13.8	< 13.7	< 6.0	< 5.3	7.0 \pm 2.2
SiIII] λ 1883	< 8.9	< 4.1	< 9.2	< 7.9	< 4.8	< 4.2	< 5.0
SiIII] λ 1892	< 7.4	< 3.4	< 7.7	< 8.5	< 3.8	< 3.8	< 3.6
[CIII] λ 1907	-	4.4 \pm 1.3	< 8.5	10.7 \pm 2.2	9.5 \pm 1.5	9.6 \pm 1.9	5.8 \pm 1.5
CIII] λ 1909	-	3.8 \pm 1.7	< 8.5	< 5.4	-	< 8.4	11.7 \pm 1.8
	Equivalent Width [\AA]						
Ly α	-	-	-	-	-	3.4 \pm 0.9	61.2 \pm 9.0
NIV] λ 1483	< 1.4	< 4.1	< 3.1	< 1.7	< 1.2	< 3.0	1.6 \pm 0.5
NIV] λ 1486	< 1.5	< 4.9	< 2.7	< 2.1	< 1.3	< 2.8	3.4 \pm 0.5
CIV] λ 1549	-	31.6 \pm 7.0	< 4.3	10.5 \pm 1.0	< 1.9	< 4.9	19.4 \pm 1.4
HeII] λ 1640	< 1.5	14.0 \pm 6.1	< 3.1	< 2.2	< 1.0	< 4.8	2.2 \pm 0.4
OIII] λ 1660	< 1.4	< 7.1	< 3.6	< 2.3	1.4 \pm 0.4	< 5.5	4.0 \pm 0.7
OIII] λ 1666	< 1.3	< 9.1	< 3.5	3.9 \pm 0.7	1.5 \pm 0.5	< 5.0	7.6 \pm 0.9
NIII]1750	< 2.2	< 11.3	< 5.2	< 3.5	< 1.3	< 10.0	3.1 \pm 1.0
SiIII] λ 1883	< 0.9	< 6.4	< 4.1	< 2.5	< 1.4	< 5.0	< 2.6
SiIII] λ 1892	< 0.7	< 7.3	< 3.5	< 2.7	< 1.1	< 4.5	< 1.9
[CIII] λ 1907	-	6.5 \pm 2.7	< 3.6	3.1 \pm 0.6	2.8 \pm 0.5	3.6 \pm 0.7	2.9 \pm 0.7
CIII] λ 1909	-	5.5 \pm 2.2	< 5.5	< 2.4	-	< 4.9	5.9 \pm 1.1

Note. Upper limits are provided at the 3σ level. Fluxes and equivalent widths of emission lines lacking wavelength coverage are indicated by a “-” symbol. Equivalent widths are calculated using the continuum level measured from the spectrum if the continuum is detected at $>3\sigma$.

Table 7
Emission-line Fluxes and Equivalent Widths of Rest-frame Optical Features for Our JWST/NIRSpec Sample of Galaxies in Abell1703

Line	A1703-zd1	A1703-zd2	A1703-zd5.1	A1703-zd5.2	A1703-23	A1703-zd4	A1703-zd6
	Line Flux [10^{-19} erg/s/cm 2]						
[OII] λ 3728	23.1 \pm 2.2	-	-	-	-	15.1 \pm 1.3	< 5.8
[NeIII] λ 3869	14.4 \pm 2.0	< 13.0	< 17.4	< 19.3	-	< 3.2	19.5 \pm 1.6
HeI λ 3890 + H8	< 5.1	< 9.9	< 14.8	< 11.8	-	< 3.6	6.5 \pm 1.6
H ϵ	< 5.6	< 6.7	< 9.9	< 9.7	-	< 3.6	13.0 \pm 1.7
H δ	10.8 \pm 1.2	< 4.7	< 6.9	8.4 \pm 2.3	< 17.2	< 3.0	9.2 \pm 1.2
H γ	11.0 \pm 1.2	7.8 \pm 1.4	< 6.1	14.2 \pm 2.0	4.8 \pm 1.4	4.3 \pm 0.8	20.0 \pm 1.4
[OIII] λ 4363	< 3.3	< 4.2	< 4.8	< 5.1	< 4.2	< 3.4	11.3 \pm 1.0
HeII λ 4686	< 3.7	< 4.4	< 6.1	< 5.8	< 4.8	< 3.2	< 3.5
H β	23.0 \pm 1.3	12.4 \pm 1.1	5.7 \pm 1.6	25.1 \pm 1.6	19.4 \pm 1.3	11.1 \pm 1.0	32.7 \pm 1.3
[OIII] λ 4959	60.4 \pm 1.6	16.2 \pm 1.2	< 5.4	32.4 \pm 1.8	46.8 \pm 1.4	28.4 \pm 1.3	77.1 \pm 1.8
[OIII] λ 5007	185.5 \pm 2.4	64.9 \pm 1.7	17.8 \pm 2.3	110.8 \pm 2.1	147.9 \pm 2.2	84.1 \pm 1.6	207.8 \pm 2.4
HeI λ 5876	< 4.6	< 3.4	< 4.3	< 4.4	< 3.8	-	8.4 \pm 1.4
H α	60.7 \pm 3.1	-	19.3 \pm 2.8	70.1 \pm 2.8	69.8 \pm 2.3	-	-
[NII] λ 6585	< 6.4	-	< 5.5	< 5.7	< 5.4	-	-
[SII] λ 6717	-	-	-	-	7.5 \pm 2.2	-	-
[SII] λ 6730	-	-	-	-	7.1 \pm 2.1	-	-
	Equivalent Width [\AA]						
[OII] λ 3728	9.9 \pm 1.4	-	-	-	-	214.4 \pm 56.8	< 15.5
[NeIII] λ 3869	34.5 \pm 7.3	< 41.1	< 79.8	< 8.5	-	< 27.7	58.3 \pm 9.7
HeI λ 3890 + H8	< 12.0	< 34.5	< 63.9	< 7.2	-	< 34.4	20.0 \pm 6.3
H ϵ	< 17.6	< 35.7	< 30.5	< 17.0	-	67.1 \pm 23.8	67.1 \pm 17.6
H δ	50.2 \pm 9.7	< 37.9	34.0 \pm 14.4	17.5 \pm 5.4	< 101.2	< 30.8	80.3 \pm 25.2
H γ	69.5 \pm 18.3	131.9 \pm 55.0	< 18.7	91.2 \pm 35.3	9.8 \pm 3.2	61.7 \pm 19.4	133.8 \pm 33.0
[OIII] λ 4363	< 22.2	< 39.3	< 33.9	< 5.7	< 8.7	< 32.9	73.1 \pm 18.5
HeII λ 4686	< 23.8	< 48.7	< 48.0	< 25.6	< 9.9	< 38.3	< 28.9
H β	116.9 \pm 14.5	208.8 \pm 80.6	86.3 \pm 53.6	169.7 \pm 43.7	46.0 \pm 4.2	147.9 \pm 46.4	423.8 \pm 112.4
[OIII] λ 4959	292.7 \pm 26.8	274.4 \pm 104.8	< 42.8	218.6 \pm 56.0	123.5 \pm 7.3	431.4 \pm 133.2	1006.1 \pm 219.7
[OIII] λ 5007	880.2 \pm 82.7	1096.4 \pm 412.2	267.3 \pm 152.3	748.9 \pm 187.8	414.8 \pm 22.1	1316.7 \pm 432.4	2686.6 \pm 632.8
HeI λ 5876	< 30.0	< 43.3	< 58.0	< 10.7	< 15.7	-	43.7 \pm 8.2
H α	210.1 \pm 44.4	-	157.7 \pm 57.6	651.5 \pm 227.3	192.9 \pm 40.8	-	-
[NII] λ 6585	< 22.5	-	< 42.1	< 48.1	< 28.6	-	-
[SII] λ 6717	-	-	-	-	15.0 \pm 4.5	-	-
[SII] λ 6730	-	-	-	-	14.2 \pm 4.3	-	-

Note. Upper limits are provided at the 3σ level. Emission lines indicated by a “-” symbol do not have wavelength coverage in the spectra.

Appendix B

Best-fit SEDs to Synthesized Photometry

Figure 19 presents the broadband photometry synthesized from the A1703 sample spectra and best-fit BEAGLE SEDs that are described in Section 2.2.

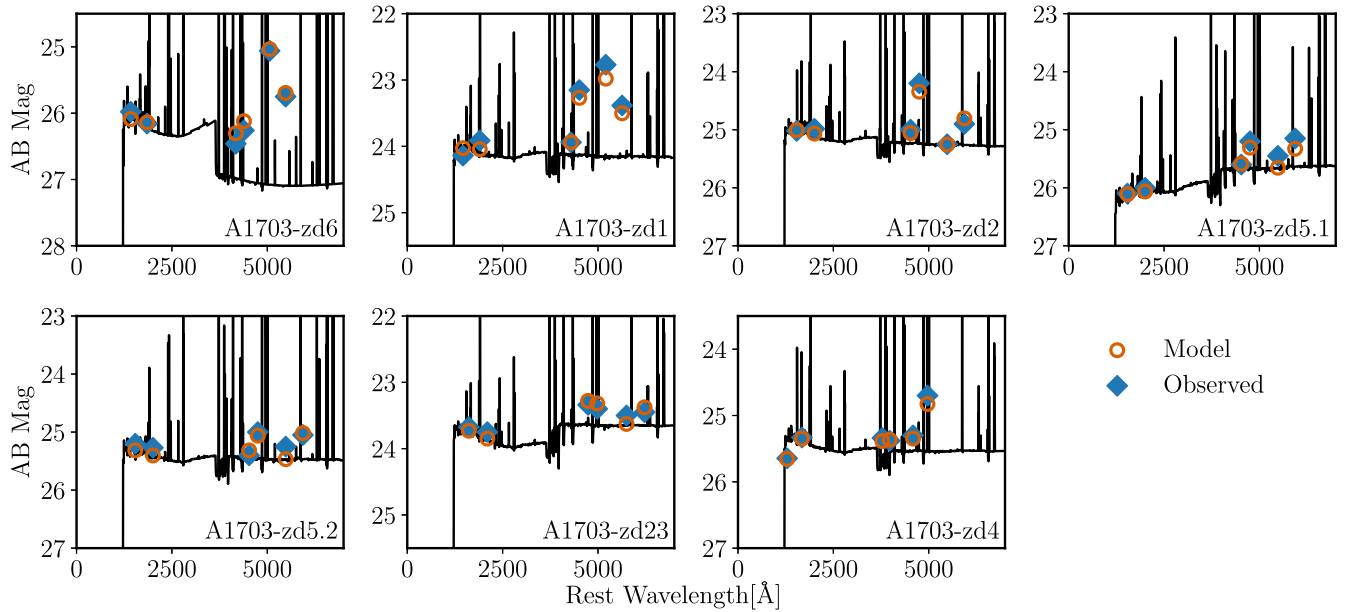


Figure 19. Best-fit BEAGLE SEDs to the synthesized photometry of the A1703 sample. The model setup is described in Section 2.2. Broadband fluxes synthesized from the NIRSpect spectra are displayed as blue diamonds, and predicted fluxes from the best-fit SED model are shown as red circles.

Appendix C Tentative CIV and NIV] Emitting Sources

In searching for CIV and NIV] emitters in the public JWST spectra, we identified several objects that appeared to display emission in these UV lines, yet we were unable to classify the lines as “robust.” These tentative sources are presented at the bottom of Table 5. We identify tentative NIV] lines in the spectra of JADES-3990 and UNCOVER-34265. D. Schaerer et al. (2024) recently presented a detection of NIV] from the PRISM spectrum of JADES-3990. While we also note an apparent emission feature at the rest-frame wavelength of NIV], we do not measure it at the 5σ significance level we require to consider it in our robust sample. The spectrum of UNCOVER-34265 presents an excess of emission coincident with NIV]. However, in addition to being measured at $< 5\sigma$, the line comprises only one pixel in the spectrum, increasing the likelihood of being either an artifact or the result of scatter from noise. In addition to these tentative NIV] emitters, we identify several objects with tentative CIV emission lines. All of JADES-5173, UNCOVER-10155, and UNCOVER-23604 show emission features in their PRISM spectra coincident with the wavelength of CIV. However, in each of these cases, the S/N of the line does not reach the necessary 5σ limit. In addition, the tentative CIV lines in JADES-5173 spectra do not appear in its corresponding $R\sim 1000$ NIRSpect spectra. The apparent CIV emission line in JADES-9903 is detected at a higher S/N than the other tentative sources; however, the line centroid is offset from systemic by $\sim 5000 \text{ km s}^{-1}$. While this is comparable to the instrumental resolution of the NIRSpect PRISM at this wavelength, this offset is significant enough to preclude JADES-9903 from being included in the robust sample.

ORCID iDs

Peter Senchyna <https://orcid.org/0000-0002-9132-6561>
 Zuyi Chen <https://orcid.org/0000-0002-2178-5471>
 Adi Zitrin <https://orcid.org/0000-0002-0350-4488>
 Ryan Endsley <https://orcid.org/0000-0003-4564-2771>

Stéphane Charlot <https://orcid.org/0000-0003-3458-2275>
 Lukas J. Furtak <https://orcid.org/0000-0001-6278-032X>
 Michael V. Maseda <https://orcid.org/0000-0003-0695-4414>
 Renske Smit <https://orcid.org/0000-0001-8034-7802>
 Ramesh Mainali <https://orcid.org/0000-0003-0094-6827>
 Jacopo Chevallard <https://orcid.org/0000-0002-7636-0534>
 Jane R. Rigby <https://orcid.org/0000-0002-7627-6551>

References

- Abazajian, K. N., Adelman-McCarthy, J. K., Agüeros, M. A., et al. 2009, *ApJS*, **182**, 543
 Adamo, A., Kruijssen, J. M. D., Bastian, N., Silva-Villa, E., & Ryon, J. 2015, *MNRAS*, **452**, 246
 Adamo, A., Östlin, G., & Zackrisson, E. 2011, *MNRAS*, **417**, 1904
 Adamo, A., Bradley, L. D., Vanzella, E., et al. 2024, *Natur*, **632**, 513
 Akerman, C. J., Carigi, L., Nissen, P. E., Pettini, M., & Asplund, M. 2004, *A&A*, **414**, 931
 Alexandroff, R., Strauss, M. A., Greene, J. E., et al. 2013, *MNRAS*, **435**, 3306
 Allen, J. T., Hewett, P. C., Maddox, N., Richards, G. T., & Belokurov, V. 2011, *MNRAS*, **410**, 860
 Allen, S. W., Edge, A. C., Fabian, A. C., et al. 1992, *MNRAS*, **259**, 67
 Arellano-Córdova, K. Z., Berg, D. A., Chisholm, J., et al. 2022, *ApJL*, **940**, L23
 Arrabal Haro, P., Dickinson, M., Finkelstein, S. L., et al. 2023a, *Natur*, **622**, 707
 Arrabal Haro, P., Dickinson, M., Finkelstein, S. L., et al. 2023b, *ApJL*, **951**, L22
 Asplund, M., Grevesse, N., Sauval, A. J., & Scott, P. 2009, *ARA&A*, **47**, 481
 Bastian, N., & Lardo, C. 2018, *ARA&A*, **56**, 83
 Berg, D. A., Chisholm, J., Erb, D. K., et al. 2021, *ApJ*, **922**, 170
 Berg, D. A., Erb, D. K., Auger, M. W., Pettini, C., & Brammer, G. B. 2018, *ApJ*, **859**, 164
 Berg, D. A., Erb, D. K., Henry, R. B. C., Skillman, E. D., & McQuinn, K. B. W. 2019, *ApJ*, **874**, 93
 Berg, D. A., Pogge, R. W., Skillman, E. D., et al. 2020, *ApJ*, **893**, 96
 Berg, D. A., Skillman, E. D., Henry, R. B. C., Erb, D. K., & Carigi, L. 2016, *ApJ*, **827**, 126
 Bezanson, R., Labbe, I., Whitaker, K. E., et al. 2024, *ApJ*, **974**, 92
 Bouwens, R. J., Oesch, P. A., Stefanon, M., et al. 2021, *AJ*, **162**, 47
 Boyett, K., Bunker, A. J., Curtis-Lake, E., et al. 2024, *MNRAS*, **535**, 1796
 Bradley, L. D., Bouwens, R. J., Zitrin, A., et al. 2012, *ApJ*, **747**, 3
 Brammer, G. 2023, grizli, Version 1.9.11, Zenodo doi:10.5281/zenodo.8370018

- Brown, G., & Gnedin, O. Y. 2021, *MNRAS*, 508, 5935
- Bruzual, G., & Charlot, S. 2003, *MNRAS*, 344, 1000
- Bunker, A. J., Saxena, A., Cameron, A. J., et al. 2023, *A&A*, 877, A88
- Bushouse, H., Eisenhamer, J., Dencheva, N., et al. 2024, JWST Calibration Pipeline, Zenodo, doi:10.5281/zenodo.6984365
- Cameron, A. J., Katz, H., Rey, M. P., & Saxena, A. 2023a, *MNRAS*, 523, 3516
- Cameron, A. J., Katz, H., Witten, C., et al. 2024, *MNRAS*, 534, 523
- Cameron, A. J., Saxena, A., Bunker, A. J., et al. 2023b, *A&A*, 677, A115
- Cardelli, J. A., Clayton, G. C., & Mathis, J. S. 1989, *ApJ*, 345, 245
- Carigi, L., & Peimbert, M. 2011, *RMxAA*, 47, 139
- Carlos, M., Marino, A. F., Milone, A. P., et al. 2023, *MNRAS*, 519, 1695
- Carretta, E., Bragaglia, A., Lucatello, S., et al. 2018, *A&A*, 615, A17
- Carretta, E., Gratton, R. G., Lucatello, S., Bragaglia, A., & Bonifacio, P. 2005, *A&A*, 433, 597
- Castellano, M., Napolitano, L., Fontana, A., et al. 2024, *ApJ*, 972, 143
- Charbonnel, C., Schaerer, D., Prantzos, N., et al. 2023, *A&A*, 673, L7
- Chen, Z., Stark, D. P., Mason, C., et al. 2024, *MNRAS*, 528, 7052
- Chevallard, J., & Charlot, S. 2016, *MNRAS*, 462, 1415
- Christensen, L., Laursen, P., Richard, J., et al. 2012, *MNRAS*, 427, 1973
- Cullen, F., McLure, R. J., McLeod, D. J., et al. 2023, *MNRAS*, 520, 14
- Curti, M., Mannucci, F., Cresci, G., & Maiolino, R. 2020, *MNRAS*, 491, 944
- Curti, M., D'Eugenio, F., Carniani, S., et al. 2023, *MNRAS*, 518, 425
- Curti, M., Witstok, J., Jakobsen, P., et al. 2024, arXiv: 2407.02575
- Curtis-Lake, E., Carniani, S., Cameron, A., et al. 2023, *NatAs*, 7, 622
- Dekel, A., Sarkar, K. C., Birnboim, Y., Mandelker, N., & Li, Z. 2023, *MNRAS*, 523, 3201
- D'Eugenio, F., Maiolino, R., Carniani, S., et al. 2024, *A&A*, 689, A152
- Dome, T., Tacchella, S., Fialkov, A., et al. 2024, *MNRAS*, 527, 2139
- Du, X., Shapley, A. E., Tang, M., et al. 2020, *ApJ*, 890, 65
- Du, X., Shapley, A. E., Topping, M. W., et al. 2021, *ApJ*, 920, 95
- Dufour, R. J., Garnett, D. R., & Shields, G. A. 1988, *ApJ*, 332, 752
- Eisenstein, D. J., Willott, C., Alberts, S., et al. 2023a, arXiv: 2306.02465
- Eisenstein, D. J., Johnson, B. D., Robertson, B., et al. 2023b, arXiv:2310.12340
- Eliasdóttir, Á., Limousin, M., Richard, J., et al. 2007, arXiv:0710.5636
- Endsley, R., Stark, D. P., Whitler, L., et al. 2023, *MNRAS*, 524, 2312
- Endsley, R., Stark, D. P., Whitler, L., et al. 2024, *MNRAS*, 533, 1111
- Erb, D. K., Pettini, M., Shapley, A. E., et al. 2010, *ApJ*, 719, 1168
- Esteban, C., García-Rojas, J., Carigi, L., et al. 2014, *MNRAS*, 443, 624
- Feltre, A., Charlot, S., & Gutkin, J. 2016, *MNRAS*, 456, 3354
- Finkelstein, S. L., Bagley, M., & Yang, G. 2023a, Data from The Cosmic Evolution Early Release Science Survey (CEERS), MAST, doi:10.17909/77P0-8481
- Finkelstein, S. L., Bagley, M. B., Ferguson, H. C., et al. 2023b, *ApJL*, 946, L13
- Fujimoto, S., Arrabal Haro, P., Dickinson, M., et al. 2023, *ApJL*, 949, L25
- Fujimoto, S., Wang, B., Weaver, J., et al. 2024, *ApJ*, 977, 250
- Furlanetto, S. R., & Mirocha, J. 2022, *MNRAS*, 511, 3895
- Furtak, L. J., Zitrin, A., Weaver, J. R., et al. 2023, *MNRAS*, 523, 4568
- Garnett, D. R., Skillman, E. D., Dufour, R. J., et al. 1995, *ApJ*, 443, 64
- Gieles, M., Charbonnel, C., Krause, M. G. H., et al. 2018, *MNRAS*, 478, 2461
- Gratton, R., Sneden, C., & Carretta, E. 2004, *ARA&A*, 42, 385
- Grudić, M. Y., Kruijssen, J. M. D., Faucher-Giguère, C.-A., et al. 2021, *MNRAS*, 506, 3239
- Gutkin, J., Charlot, S., & Bruzual, G. 2016, *MNRAS*, 462, 1757
- Guzzo, L., Schuecker, P., Böhringer, H., et al. 2009, *A&A*, 499, 357
- Hainline, K. N., D'Eugenio, F., Jakobsen, P., et al. 2024, *ApJ*, 976, 160
- Harikane, Y., Nakajima, K., Ouchi, M., et al. 2024, *ApJ*, 960, 56
- Harikane, Y., Zhang, Y., Nakajima, K., et al. 2023, *ApJ*, 959, 39
- Heintz, K. E., Brammer, G. B., Watson, D., et al. 2025, *A&A*, 693, A60
- Henry, R. B. C., Edmunds, M. G., & Köppen, J. 2000, *ApJ*, 541, 660
- Horne, K. 1986, *PASP*, 98, 609
- Hu, W., Papovich, C., Dickinson, M., et al. 2024, *ApJ*, 971, 21
- Hutchison, T. A., Papovich, C., Finkelstein, S. L., et al. 2019, *ApJ*, 879, 70
- Isobe, Y., Ouchi, M., Tominaga, N., et al. 2023, *ApJ*, 959, 100
- Izotov, Y. I., Orlitová, I., Schaerer, D., et al. 2016a, *Natur*, 529, 178
- Izotov, Y. I., Schaerer, D., Guseva, N. G., Thuan, T. X., & Worseck, G. 2024, *MNRAS*, 528, L10
- Izotov, Y. I., Schaerer, D., Thuan, T. X., et al. 2016b, *MNRAS*, 461, 3683
- Izotov, Y. I., Schaerer, D., Worseck, G., et al. 2018a, *MNRAS*, 474, 4514
- Izotov, Y. I., Stasińska, G., Meynet, G., Guseva, N. G., & Thuan, T. X. 2006, *A&A*, 448, 955
- Izotov, Y. I., Thuan, T. X., Guseva, N. G., & Liss, S. E. 2018b, *MNRAS*, 473, 1956
- James, B. L., Auger, M., Pettini, M., et al. 2018, *MNRAS*, 476, 1726
- James, B. L., Pettini, M., Christensen, L., et al. 2014, *MNRAS*, 440, 1794
- Jones, G. C., Bunker, A. J., Saxena, A., et al. 2024, *A&A*, 683, A238
- Jones, T., Stark, D. P., & Ellis, R. S. 2012, *ApJ*, 751, 51
- Jones, T., Sanders, R., Chen, Y., et al. 2023, *ApJL*, 951, L17
- Jullo, E., Kneib, J. P., Limousin, M., et al. 2007, *NJPh*, 9, 447
- Katz, H., Saxena, A., Cameron, A. J., et al. 2023, *MNRAS*, 518, 592
- Keeton, C. R. 2001, arXiv: astro-ph/0102340
- Kennicutt, R. C. J. 1984, *ApJ*, 287, 116
- Kewley, L. J., Nicholls, D. C., & Sutherland, R. S. 2019, *ARA&A*, 57, 511
- Kim, J.-G., Ostriker, E. C., & Filippova, N. 2021, *ApJ*, 911, 128
- Kobayashi, C., & Ferrara, A. 2024, *ApJL*, 962, L6
- Koekemoer, A. M., Faber, S. M., Ferguson, H. C., et al. 2011, *ApJS*, 197, 36
- Laporte, N., Nakajima, K., Ellis, R. S., et al. 2017, *ApJ*, 851, 40
- Larson, R. L., Finkelstein, S. L., Kocevski, D. D., et al. 2023, *ApJL*, 953, L29
- Laseter, I. H., Maseda, M. V., Curti, M., et al. 2023, *A&A*, 681, A70
- Lehnert, M. D., Nesvadba, N. P. H., Le Tiran, L., et al. 2009, *ApJ*, 699, 1660
- Li, Z., Dekel, A., Sarkar, K. C., et al. 2024, *A&A*, 690, A108
- Limousin, M., Richard, J., Kneib, J. P., et al. 2008, *A&A*, 489, 23
- Llerena, M., Amorin, R., Pentericci, L., et al. 2023, *A&A*, 676, A53
- Luridiana, V., Morisset, C., & Shaw, R. A. 2015, *A&A*, 573, A42
- Ma, X., Hopkins, P. F., Garrison-Kimmel, S., et al. 2018, *MNRAS*, 478, 1694
- Ma, X., Grudić, M. Y., Quataert, E., et al. 2020, *MNRAS*, 493, 4315
- Mainali, R., Kollmeier, J. A., Stark, D. P., et al. 2017, *ApJL*, 836, L14
- Mainali, R., Stark, D. P., Jones, T., et al. 2023, *MNRAS*, 520, 4037
- Mainali, R., Zitrin, A., Stark, D. P., et al. 2018, *MNRAS*, 479, 1180
- Maiolino, R., Scholtz, J., Witstok, J., et al. 2024a, *Natur*, 627, 59
- Maiolino, R., Scholtz, J., Curtis-Lake, E., et al. 2024b, *A&A*, 691, A145
- Marques-Chaves, R., Schaerer, D., Kuruvanthodi, A., et al. 2024, *A&A*, 681, A30
- Martins, F., & Palacios, A. 2022, *A&A*, 659, A163
- Martins, F., Schaerer, D., Haemmerlé, L., & Charbonnel, C. 2020, *A&A*, 633, A9
- Martins, F., Schaerer, D., Marques-Chaves, R., & Upadhyaya, A. 2023, *A&A*, 678, A159
- Maseda, M. V., van der Wel, A., Rix, H.-W., et al. 2018, *ApJ*, 854, 29
- Matthee, J., Mackenzie, R., Simcoe, R. A., et al. 2023, *ApJ*, 950, 67
- Meena, A. K., Zitrin, A., Jiménez-Teja, Y., et al. 2023, *ApJL*, 944, L6
- Mingozzi, M., James, B. L., Arellano-Córdova, K. Z., et al. 2022, *ApJ*, 939, 110
- Mirocha, J., & Furlanetto, S. R. 2023, *MNRAS*, 519, 843
- Molyneux, S. J., Smit, R., Schaerer, D., et al. 2022, *MNRAS*, 512, 535
- Morales, A. M., Finkelstein, S. L., Leung, G. C. K., et al. 2024, *ApJL*, 964, L24
- Nagele, C., & Umeda, H. 2023, *ApJL*, 949, L16
- Nakajima, K., Schaerer, D., Le Fèvre, O., et al. 2018, *A&A*, 612, A94
- Nakane, M., Ouchi, M., Nakajima, K., et al. 2024, *ApJ*, 967, 28
- Nandal, D., Regan, J. A., Woods, T. E., et al. 2024a, *A&A*, 683, A156
- Nandal, D., Sibony, Y., & Tsiatsioui, S. 2024b, *A&A*, 688, A142
- Navarro-Carrera, R., Caputi, K. I., Iani, E., et al. 2024, arXiv: 2407.14201
- Nomoto, K., Kobayashi, C., & Tominaga, N. 2013, *ARA&A*, 51, 457
- Oke, J. B., & Gunn, J. E. 1983, *ApJ*, 266, 713
- Pahl, A. J., Shapley, A., Faisst, A. L., et al. 2020, *MNRAS*, 493, 3194
- Pascale, M., Dai, L., McKee, C. F., & Tsang, B. T. H. 2023, *ApJ*, 957, 77
- Pascale, M., Frye, B. L., Diego, J., et al. 2022, *ApJL*, 938, L6
- Pascale, M., Frye, B. L., Pierel, J. D. R., et al. 2025, *ApJ*, 979, 13
- Pei, Y. C. 1992, *ApJ*, 395, 130
- Plat, A., Charlot, S., Bruzual, G., et al. 2019, *MNRAS*, 490, 978
- Portegies Zwart, S. F., Baumgardt, H., Hut, P., Makino, J., & McMillan, S. L. W. 2004, *Natur*, 428, 724
- Quinlan, G. D., & Shapiro, S. L. 1990, *ApJ*, 356, 483
- Rankine, A. L., Hewett, P. C., Banerji, M., & Richards, G. T. 2020, *MNRAS*, 492, 4553
- Rantala, A., Naab, T., & Lahén, N. 2024, *MNRAS*, 531, 3770
- Rauscher, B. J. 2024, *PASP*, 136, 015001
- Ravindranath, S., Monroe, T., Jaskot, A., Ferguson, H. C., & Tumlinson, J. 2020, *ApJ*, 896, 170
- Renzini, A. 2023, *MNRAS*, 525, L117
- Richard, J., Pei, L., Limousin, M., Jullo, E., & Kneib, J. P. 2009, *A&A*, 498, 37
- Rieke, M., Robertson, B., Tacchella, S., et al. 2023a, Data from the JWST Advanced Deep Extragalactic Survey (JADES), MAST, doi:10.17909/8tdj-8n28
- Rieke, M. J., Robertson, B., Tacchella, S., et al. 2023b, *ApJS*, 269, 16
- Rivera-Thorsen, T. E., Chisholm, J., Welch, B., et al. 2024, *A&A*, 690, A269
- Roberts-Borsani, G., Treu, T., Shapley, A., et al. 2024, *ApJ*, 976, 193
- Roberts-Borsani, G. W., Bouwens, R. J., Oesch, P. A., et al. 2016, *ApJ*, 823, 143
- Saldana-Lopez, A., Schaerer, D., Chisholm, J., et al. 2023, *MNRAS*, 522, 6295

- Sanders, R. L., Shapley, A. E., Topping, M. W., Reddy, N. A., & Brammer, G. B. 2023, *ApJ*, **955**, 54
- Sanders, R. L., Shapley, A. E., Topping, M. W., Reddy, N. A., & Brammer, G. B. 2024, *ApJ*, **962**, 24
- Sanders, R. L., Shapley, A. E., Kriek, M., et al. 2016, *ApJ*, **816**, 23
- Sanders, R. L., Shapley, A. E., Reddy, N. A., et al. 2020, *MNRAS*, **491**, 1427
- Saxena, A., Robertson, B. E., Bunker, A. J., et al. 2023, *A&A*, **678**, A68
- Schaerer, D., Boone, F., Zamojski, M., et al. 2015, *A&A*, **574**, A19
- Schaerer, D., Marques-Chaves, R., Barrufet, L., et al. 2022, *A&A*, **665**, L4
- Schaerer, D., Marques-Chaves, R., Xiao, M., & Korber, D. 2024, *A&A*, **687**, L11
- Schenker, M. A., Stark, D. P., Ellis, R. S., et al. 2012, *ApJ*, **744**, 179
- Schmidt, K. B., Huang, K. H., Treu, T., et al. 2017, *ApJ*, **839**, 17
- Scholtz, J., Maiolino, R., D'Eugenio, F., et al. 2023, arXiv: 2311.18731
- Senchyna, P., Plat, A., Stark, D. P., & Rudie, G. C. 2024, *ApJ*, **966**, 92
- Senchyna, P., Stark, D. P., Charlot, S., et al. 2021, *MNRAS*, **503**, 6112
- Senchyna, P., Stark, D. P., Chevallard, J., et al. 2019, *MNRAS*, **488**, 3492
- Senchyna, P., Stark, D. P., Vidal-Garcia, A., et al. 2017, *MNRAS*, **472**, 2608
- Senchyna, P., Stark, D. P., Charlot, S., et al. 2022, *ApJ*, **930**, 105
- Shapley, A. E., Sanders, R. L., Reddy, N. A., Topping, M. W., & Brammer, G. B. 2023, *ApJ*, **954**, 157
- Shapley, A. E., Steidel, C. C., Pettini, M., & Adelberger, K. L. 2003, *ApJ*, **588**, 65
- Smit, R., Bouwens, R. J., Labbé, I., et al. 2014, *ApJ*, **784**, 58
- Smith, L. J., Crowther, P. A., Calzetti, D., & Sidoli, F. 2016, *ApJ*, **823**, 38
- Speagle, J. S., Steinhardt, C. L., Capak, P. L., & Silverman, J. D. 2014, *ApJS*, **214**, 15
- Steidel, C. C., Erb, D. K., Shapley, A. E., et al. 2010, *ApJ*, **717**, 289
- Stark, D. P., Ellis, R. S., Charlot, S., et al. 2017, *MNRAS*, **464**, 469
- Stark, D. P., Richard, J., Siana, B., et al. 2014, *MNRAS*, **445**, 3200
- Stark, D. P., Walth, G., Charlot, S., et al. 2015a, *MNRAS*, **454**, 1393
- Stark, D. P., Richard, J., Charlot, S., et al. 2015b, *MNRAS*, **450**, 1846
- Steidel, C. C., Strom, A. L., Pettini, M., et al. 2016, *ApJ*, **826**, 159
- Stiavelli, M., Morishita, T., Chiaberge, M., et al. 2023, *ApJL*, **957**, L18
- Strait, V., Brammer, G., Muzzin, A., et al. 2023, *ApJL*, **949**, L23
- Tacchella, S., Johnson, B. D., Robertson, B. E., et al. 2023, *MNRAS*, **522**, 6236
- Tang, M., Stark, D. P., Chevallard, J., & Charlot, S. 2019, *MNRAS*, **489**, 2572
- Tang, M., Stark, D. P., Chevallard, J., et al. 2021, *MNRAS*, **501**, 3238
- Tang, M., Stark, D. P., Chen, Z., et al. 2023, *MNRAS*, **526**, 1657
- Tang, M., Stark, D. P., Ellis, R. S., et al. 2024, *MNRAS*, **531**, 2701
- Topping, M. W., Shapley, A. E., Stark, D. P., et al. 2021, *ApJL*, **917**, L36
- Topping, M. W., Stark, D. P., Endsley, R., et al. 2022, *MNRAS*, **516**, 975
- Topping, M. W., Stark, D. P., Senchyna, P., et al. 2024a, *MNRAS*, **529**, 3301
- Topping, M. W., Stark, D. P., Endsley, R., et al. 2024b, *MNRAS*, **529**, 4087
- Trump, J. R., Arrabal Haro, P., Simons, R. C., et al. 2023, *ApJ*, **945**, 35
- Valentino, F., Brammer, G., Gould, K. M. L., et al. 2023, *ApJ*, **947**, 20
- Vanzella, E., Castellano, M., Bergamini, P., et al. 2022, *A&A*, **659**, A2
- Vanzella, E., Loiacono, F., Bergamini, P., et al. 2023, *A&A*, **678**, A173
- Vidal-Garcia, A., Charlot, S., Bruzual, G., & Hubeny, I. 2017, *MNRAS*, **470**, 3532
- Vink, J. S. 2023, *A&A*, **679**, L9
- Weaver, J. R., Cutler, S. E., Pan, R., et al. 2024, *ApJS*, **270**, 7
- Whitler, L., Endsley, R., Stark, D. P., et al. 2023, *MNRAS*, **519**, 157
- Witstok, J., Maiolino, R., Smit, R., et al. 2025, *MNRAS*, **536**, 27
- Wofford, A., Vidal-Garcia, A., Feltre, A., et al. 2021, *MNRAS*, **500**, 2908
- Yanagisawa, H., Ouchi, M., Watanabe, K., et al. 2024, *ApJ*, **974**, 266
- Yin, J., Matteucci, F., & Vladilo, G. 2011, *A&A*, **531**, A136
- Zheng, W., Bradley, L. D., Bouwens, R. J., et al. 2009, *ApJ*, **697**, 1907
- Zitrin, A., Broadhurst, T., Umetsu, K., et al. 2010, *MNRAS*, **408**, 1916
- Zitrin, A., Labbé, I., Belli, S., et al. 2015, *ApJL*, **810**, L12